

2013

UNCERTAINTY ASSOCIATED WITH ESTIMATING A SHORT-TERM (1–3 HR) PARTICULATE MATTER CONCENTRATION FROM A HUMAN-SIGHTED VISUAL RANGE


William C. Malm

Colorado State University - Fort Collins

Bret A. Schichtel

Colorado State University - Fort Collins

Follow this and additional works at: <http://digitalcommons.unl.edu/jfspresearch>

 Part of the [Forest Biology Commons](#), [Forest Management Commons](#), [Natural Resources and Conservation Commons](#), [Natural Resources Management and Policy Commons](#), [Other Environmental Sciences Commons](#), [Other Forestry and Forest Sciences Commons](#), [Sustainability Commons](#), and the [Wood Science and Pulp, Paper Technology Commons](#)

Malm, William C. and Schichtel, Bret A., "UNCERTAINTY ASSOCIATED WITH ESTIMATING A SHORT-TERM (1–3 HR) PARTICULATE MATTER CONCENTRATION FROM A HUMAN-SIGHTED VISUAL RANGE" (2013). *JFSP Research Project Reports*. 5.

<http://digitalcommons.unl.edu/jfspresearch/5>

This Article is brought to you for free and open access by the U.S. Joint Fire Science Program at DigitalCommons@University of Nebraska - Lincoln. It has been accepted for inclusion in JFSP Research Project Reports by an authorized administrator of DigitalCommons@University of Nebraska - Lincoln.

UNCERTAINTY ASSOCIATED WITH ESTIMATING A SHORT-TERM (1-3 HR) PARTICULATE MATTER CONCENTRATION FROM A HUMAN-SIGHTED VISUAL RANGE

$V_r=240$ miles $PM=0.0 \mu\text{g}/\text{m}^3$



$V_r=20$ miles $PM=38.0 \mu\text{g}/\text{m}^3$



**UNCERTAINTY ASSOCIATED WITH ESTIMATING A SHORT-TERM (1–3 HR)
PARTICULATE MATTER CONCENTRATION
FROM A HUMAN-SIGHTED VISUAL RANGE**

¹William C. Malm
and
²Bret A. Schichtel

¹Cooperative Institute for Research in the Atmosphere
Colorado State University
Fort Collins, CO 80523-1375

²National Park Service – Air Resources Division
Cooperative Institute for Research in the Atmosphere
Colorado State University
Fort Collins, CO 80523-1375

December 2013

**UNCERTAINTY ASSOCIATED WITH ESTIMATING A SHORT-TERM (1–3 HR)
PARTICULATE MATTER CONCENTRATION
FROM A HUMAN-SIGHTED VISUAL RANGE**

TABLE OF CONTENTS

1. Background.....	9
2. Uncertainty in Estimating an Observed Visual Range	14
2.1 Nomenclature and Fundamental Equations.....	14
2.1.1 Quantifying the Transfer of Radiation through the Atmosphere	15
2.1.2 Contrast and Contrast Transmittance.....	19
2.1.3 Visual Range and Contrast.....	20
2.1.4 Standard Visual Range.....	22
2.1.5 Relationship between Visual Range and Atmospheric Mass Concentration.....	22
2.2 Estimated Mass Concentration Dependence on Lighting Conditions and Haze Distribution	24
2.2.1 Uniformly Distributed Haze	24
2.2.2 Nonuniform Smoke Haze – Haze between Observer and Landscape Feature	25
2.3 Uncertainty in Mass Estimate Associated with Use of the Koschmieder Relationship.	26
2.3.1 Uncertainty Associated with Nonuniform Lighting or Aerosol Distribution.	26
2.3.2 Uncertainty in Estimated Mass Associated with Uncertainty in C_o	28
2.3.3 Uncertainty Associated with Contrast Judgments	29
3. Deriving Mass Scattering Efficiency from Measurements of Atmospheric Scattering and Mass Concentrations.....	31
4. Measured and Derived Mass Scattering and Extinction Efficiencies.....	39
4.1 Mass Scattering, Absorption, and Extinction Efficiency	39
4.2 Mass Scattering and Extinction Efficiencies of Smoke	42
4.2.1 Dry Mass Scattering Efficiency α_s	43
4.2.2 Hygroscopicity	48
4.2.3 Absorption Efficiency α_a	50
4.2.4 Brown Carbon Absorption.....	52
4.2.5 Optical Parameters	52
4.3 Mass Scattering Efficiencies Derived from IMPROVE Data.....	54
4.3.1 IMPROVE Monitoring Program.....	54
4.3.2 Derived Average Mass Extinction Coefficients Using IMPROVE Data	60

4.4	Effect of Background Aerosol and RH Levels on PM Estimates, Assuming an Average Seasonal and Nationwide Mass Scattering Efficiency or CNST.	63
4.5	How Much Is Mass Estimate Inflated Because of Background Aerosol Hygroscopicity?	64
4.5.1	Increase in Mass Concentration Due to Retained Water	64
4.5.2	Examples of Uncertainty in Estimated Mass Concentration Due to Retained Water	66
4.5.3	Uncertainty of Implied Mass When Using a Single Mass Extinction Efficiency... ..	69
5.	Integrating all the Uncertainties/Variabilities in the Mass Extinction Efficiency into an Overall Uncertainty in Mass Estimate.	73
6.	Summary	79
6.1	Background	79
6.2	Uncertainties in Estimating Visual Range	80
6.2.1	Uncertainty in Estimated Mass Concentration Due to Judging When the Target Is at a Threshold Contrast.....	81
6.2.2	Uncertainty in Estimated Mass Concentration Due to Unknown Inherent Contrast	81
6.2.3	Uncertainty in Estimated Mass Concentration Due to Nonuniform Lighting Conditions and Aerosol Mass Spatial Distribution	81
6.3	Uncertainties in an Assumed Wet Mass Extinction Efficiency α_w	82
6.4	Quantifying Total Uncertainty	84
6.5	$V_r * PM = CNST$ Relationships	85
6.6	Pictorial Examples of Visual Impairment Associated with the Health Breakpoint Mass Concentrations	90
7.	Recommendations.....	95
	Quantification of Uncertainty – About a Factor of 2.....	95
	Recommendation #1 – Use a conservative estimate of the $V_r * PM = CNST$ relationship to take into account the factor of 2 uncertainty, and customize it by location.....	95
	Recommendation #2 – Two-level air quality warning system.	98
	Recommendation #3 – An actual visual range determination should not be attempted.....	98
8.	References.....	99

LIST OF FIGURES

Figure 1.1: PM vs. visual range relationships used by various states, those recommended by “Wildfire Smoke, A Guide for Public Health Officials” (2008), and those predicted from the Montana (2013) and O’Neill et al. (2013) equations, plotted on linear scales. 12

Figure 1.2: PM vs. visual range relationships used by various states, those recommended by “Wildfire Smoke, A Guide for Public Health Officials” (2008), and those predicted from the Montana (2013) and O’Neill et al. (2013) equations, plotted on log scales. 12

Figure 1.3: Percent differences between the PM levels predicted for a given visual range used by various states and those presented in “Wildfire Smoke, A Guide for Public Health Officials” (2008) and a reference value of $V_r * PM = 724$ 13

Figure 1.4: Summary of the relationships between human health impact categories and PM concentrations used by different agencies and states. 14

Figure 2.1: Schematic diagram contrasting how the effects of molecular volume scattering function on scattered radiation differ from those of the fine particle scattering function. 15

Figure 2.2: Illustrative geometry for a sight path. 16

Figure 2.3: Diagram showing how path radiance and attenuated image-forming information combine to form the observed image at the eye of an observer. Direct, diffuse, and reflected radiance all contribute to illuminating the image, as well as the incremental volumes of atmosphere that sum to form sight-path radiance. 18

Figure 2.4: Schematic of a teleradiometer measurement of sky/landscape apparent contrast. 24

Figure 2.5: Plot of PM as estimated using equation 1.43 as a function of VR. The green graph refers to the estimated mass with $\gamma = 0.17$, the red graph corresponds to $\gamma = 1.0$, and the line labeled “Uncertainty” is the difference between the mass estimates, assuming $\gamma = 0.17$ and $\gamma = 1.0$ 27

Figure 2.6: Same plot as Figure 2.5, but on a log-log scale. The green graph refers to the estimated mass with $\gamma = 0.17$, the red graph corresponds to $\gamma = 1.0$, and the line labeled “Uncertainty” is the difference between the mass estimates, assuming $\gamma = 0.17$ and $\gamma = 1.0$ 27

Figure 2.7: Uncertainty in estimated mass dm/m as a function of m and uncertainty in C_o of 50%. 29

Figure 2.8: A plot of uncertainty in mass estimates, dm/m , as a function of ambient mass concentration, based on the ability of an observer to determine whether a landscape feature has reached the threshold contrast of -0.02. 31

Figure 3.1: Plots of $PM_{2.5}$ vs. visual range as derived from open air nephelometer measurements of b_{scat} . Also shown in each of the graphs is a curve fit of the measured data and visual range vs. $PM_{2.5}$, assuming $3.912/\alpha = 724$ and 622 35

Figure 3.2: Spatial distribution of the average wet mass scattering efficiency α derived from the curve fit between measured b_{scat} and PM 36

Figure 3.3: Mass scattering efficiencies for selected IMPROVE sites where integrating nephelometers are operated. 37

Figure 3.4: Plot of the percent differences between $\alpha = 6.3$ implied by the $V_r PM = 622$ relationship and the derived α obtained from nephelometer and fine mass measurements.....	37
Figure 3.5: Plot of the average percent of the mean α represented by 2 standard deviations of the mean α value for each season and across all seasons.	39
Figure 4.1: Yearly average mass extinction efficiencies for each of the IMPROVE monitoring locations.	60
Figure 4.2: Plot of average mass extinction efficiency and its standard deviation for each of the IMPROVE monitoring sites.....	61
Figure 4.3: The proportionality constant between V_r and PM. $CNST = 3912/\alpha$	62
Figure 4.4: The proportionality constant between V_r and PM derived from $CNST = 3912/\alpha$ and $CNST = 622$	62
Figure 4.5: Amount of water mass concentration, assuming an average background particle concentration and $RH = 90\%$	65
Figure 4.6: Amount of water mass concentration, assuming that the background particle mass is the average plus one standard deviation and an $RH = 90\%$	66
Figure 4.7: Health breakpoints associated with 1–3 hr, 8 hr, and 24 hr average mass concentrations.	67
Figure 4.8: Uncertainty between implied mass concentration derived from a visual range observation and real mass concentrations for an average $f(RH)$ and average background	67
Figure 4.9: “a” shows an average background aerosol concentration combined with an average $f(RH)$ value, while “b” and “c” correspond to an average background aerosol concentration but with an $f(RH)$ that corresponds to $RH = 90\%$ and an average background aerosol concentration plus one standard deviation associated with that background and $RH = 90\%$, respectively.	68
Figure 4.10: Average $f(RH)$ and average background compared to $TM = 622/(\text{actual visual range})$ for a mass cutpoint of $38.0 \mu\text{g}/\text{m}^3$. Red color corresponds to implied mass being less than actual mass.	70
Figure 4.11: Plot of the percent difference between true mass and mass derived from $TM = 622/(\text{actual visual range})$ for average aerosol background and average RH for each IMPROVE site listed in Table 4.7. Order of sites is from west to east. The various colors correspond to the different mass concentration breakpoints associated with health endpoints.	71
Figure 4.12: $f(RH)$ corresponding to $RH = 90\%$ and average background compared to $TM = 622/(\text{actual visual range})$ for a mass cutpoint of $38.0 \mu\text{g}/\text{m}^3$. When implied mass is greater than actual mass, it is plotted in green, and when it is less than real mass, it is plotted in red.....	72
Figure 4.13: Plot of the percent difference between true mass and mass derived from $TM = 622/(\text{actual visual range})$ for average aerosol background and $RH = 90\%$ for each IMPROVE site listed in Table 4.7. Order of sites is from west to east. The various colors correspond to the different mass concentration breakpoints associated with health endpoints.	72
Figure 4.14: Plot of the percent difference between true mass and mass derived from $TM = 622/(\text{actual visual range})$ for average aerosol background plus one standard deviation and $RH = 90\%$ for each IMPROVE site listed in Table 4.7. Order of sites is from west to east. The various	

colors correspond to the different mass concentration breakpoints associated with health endpoints.	73
Figure 5.1: Average uncertainty in mass concentration resulting from the variability in mass extinction efficiencies.	76
Figure 6.1: Plot of PM vs. visual range from the smoke guide’s (“Wildfire Smoke, A Guide for Public Health Officials”, 2008) best dry and ambient (wet) estimate PM vs. visual range relationships for the West.	87
Figure 6.2: Plot of the smoke guide’s (“Wildfire Smoke, A Guide for Public Health Officials”, 2008) PM vs. visual range relationship as well as the uncertainty in the PM estimate derived from a visual range observation. The Best Estimate visual range values are for ambient conditions, taking into account relative humidity. Also plotted are the recommended visual ranges that are to be associated with the mass concentration breakpoint.	88
Figure 6.3: Log-log plot of the smoke guide’s (“Wildfire Smoke, A Guide for Public Health Officials”, 2008) PM vs. visual range relationship as well as the uncertainty in the PM estimate derived from a visual range observation. Also plotted are the recommended visual ranges that are to be associated with the mass concentration breakpoint.	89
Figure 6.4: Plot of PM vs. visual range from the smoke guide’s (“Wildfire Smoke, A Guide for Public Health Officials”, 2008) best dry and ambient (wet) estimate, PM vs. visual range relationships for the East.	90
Figure 6.5: Desert View as seen from Hopi Point, Grand Canyon, Arizona. Distances to a number of landscape features are indicated.	91
Figure 6.6: The center column (column 2) shows the appearance of the Grand Canyon scene as it would appear in an atmosphere where the ambient mass concentration corresponded to the visual ranges listed for the first four health breakpoints. The first row shows one standard deviation variability of the appearance of the scene for a true mass concentration of $38 \mu\text{g}/\text{m}^3$, the second row the variability in the appearance of the scene for a mass concentration of $88 \mu\text{g}/\text{m}^3$, and so forth.	92
Figure 6.7: View of Dallas, Texas. Distances to a number of structures are indicated.	93
Figure 6.8: The center column (column 2) shows the appearance of the Dallas, Texas scene as it would appear in an atmosphere where the ambient mass concentration corresponded to the visual ranges listed for the first four health breakpoints. The first row shows one standard deviation variability of the appearance of the scene for a true mass concentration of $38 \mu\text{g}/\text{m}^3$, the second row the variability in the appearance of the scene for a mass concentration of $88 \mu\text{g}/\text{m}^3$, and so forth.	94
Figure 7.1: (West) Plot of the smoke guide’s (“Wildfire Smoke, A Guide for Public Health Officials”, 2008) PM vs. V_r relationship, as well as the uncertainty in the PM estimate derived from a visual range observation. Also plotted are the recommended visual ranges that are to be associated with the mass concentration breakpoint.	96
Figure 7.2: (East) Plot of the smoke guide’s (“Wildfire Smoke, A Guide for Public Health Officials”, 2008) PM vs. V_r relationship, as well as the uncertainty in the PM estimate derived	

from a visual range observation. Also plotted are the recommended visual ranges that are to be associated with the mass concentration breakpoint. 97

LIST OF TABLES

Table 1.1: Table linking AQI categories to ambient mass concentrations and visual range as reported in “Wildfire Smoke, A Guide for Public Health Officials” (2008).	10
Table 1.2: Table of visual range–PM relationships used by various states and those listed in “Wildfire Smoke, A Guide for Public Health Officials” (2008).	11
Table 1.3: Table of visual range–PM relationships predicted by the Montana (2013) and O’Neill et al. (2013) equations, using the “Wildfire Smoke, A Guide for Public Health Officials” (2008) PM breakpoints.	11
Table 3.1: List of IMPROVE sites with nephelometer and particle data.	32
Table 3.2: Average estimated extinction efficiencies, α , for each season and for the year as a function of monitoring site. Units of α are m^2/gm	35
Table 3.3: The average percent of the mean α represented by 2 standard deviations of the mean α value for each season and across all seasons.	38
Table 4.1: Average and one standard deviation of mass scattering efficiencies. “Fine”, “Coarse”, and “Total” correspond to the size range of the aerosol. “Mixed” refers to a mixed-composition aerosol. Sulfate efficiencies correspond to dry ammonium sulfate, nitrate entries correspond to dry ammonium nitrate, POM efficiencies have been normalized to an R_{oc} value of 1.8, and sea salt efficiencies have been adjusted to a dry state. The final column gives the overall average for all methods for the mixed-composition aerosols, and the average of three methods (theoretical, MLR, and partial) for the remaining species. The number of observations is given in parentheses. Estimates are for visible wavelengths (near 550 nm).	41
Table 4.2: Optical properties of smoke from the FLAME and YACS Studies. Phase: F = Flaming, M = Mixed, S = Smoldering. Data are from FLAME 2.	43
Table 4.3: Optical properties of smoke from from Reid et al. (2005b). WL = White light. Phase: F = Flaming, M = Mixed, S = Smoldering.	46
Table 4.4: Published values of biomass burning humidification factors ($f(RH)$) using nephelometry (Day et al., 2006).	49
Table 4.5: Measured smoke characteristics for biomass fuels burned from Hand et al. (2007). All burns were conducted in a chamber, were integrated over flaming and smoldering stages, and aged an hour or more. Measured $f(RH)$ is reported for $RH = 80\text{--}85\%$, with dry $RH = 20\text{--}25\%$, wavelength of 530 nm, and experimental uncertainty of ± 0.08	50
Table 4.6: Likely optical properties for dry biomass-burning smoke at 550 nm, estimated by Reid et al. (2005b) in Table 4.3.	53
Table 4.7: A list of the names of each IMPROVE monitoring site along with its abbreviation and its latitude and longitude coordinates.	55
Table 5.1: Value of $f(RH)$ and mass extinction efficiencies used to estimate total uncertainty or variability of mass extinction efficiency of background plus smoke aerosol mix.	75
Table 5.2: Summary of the uncertainties in mass extinction efficiencies of smoke and background and smoke plus background for the western and eastern United States.	77

Table 5.3: Uncertainties in a mass estimated from a visual range observation associated with uncertainties in the visual range observation and in total mixed mass extinction efficiencies..... 78

Table 6.1. The "Wildfire Smoke, A Guide for Public Health Officials" linkage of air quality index categories with 1-hr, 8-hr and 24-hr PM_{2.5} concentrations and visibility for arid conditions. The visibility scale is only linked with the 1–3 hr PM concentrations. 79

Table 6.2: Uncertainties in a mass estimated from a visual range observation associated with uncertainties in the visual range observation and in total mixed mass extinction efficiencies..... 84

Table 6.3a: (West) The smoke guide’s (“Wildfire Smoke, A Guide for Public Health Officials”, 2008) mass concentration breakpoints listed along with the percent uncertainty associated with estimating the mass breakpoints from a visual range observation. Also listed are the upper and lower bounds associated with each mass breakpoint estimate. Best-estimate dry and ambient visual ranges corresponding to the mass breakpoints as well as the recommended visual range levels are listed..... 86

Table 6.3b: (East) The smoke guide’s (“Wildfire Smoke, A Guide for Public Health Officials”, 2008) mass concentration breakpoints are listed along with the percent uncertainty associated with estimating the mass breakpoints from a visual range observation. Also listed are the upper and lower bounds associated with each mass breakpoint estimate. Best-estimate dry and ambient visual ranges corresponding to the mass breakpoints as well as the recommended visual range levels are listed..... 86

Table 7.1: (West) Smoke guide (“Wildfire Smoke, A Guide for Public Health Officials”, 2008) mass concentration breakpoints along with the percent uncertainty associated with estimating mass breakpoints from a visual range observation. Also listed are the upper and lower bounds associated with each mass breakpoint estimate. Best-estimate dry and ambient visual ranges corresponding to the mass breakpoints as well as the recommended visual range levels are listed. 95

Table 7.2: (East) Smoke guide (“Wildfire Smoke, A Guide for Public Health Officials”, 2008) mass concentration breakpoints along with the percent uncertainty associated with estimating the mass breakpoints from a visual range observation. Also listed are the upper and lower bounds associated with each mass breakpoint estimate. Best-estimate dry and ambient visual ranges corresponding to the mass breakpoints as well as the recommended visual range levels are listed. 96

UNCERTAINTY ASSOCIATED WITH ESTIMATING A SHORT-TERM (1–3 HR) PARTICULATE MATTER CONCENTRATION FROM A HUMAN-SIGHTED VISUAL RANGE

1. BACKGROUND

Several state air quality agencies have developed policies to issue air quality health index (AQI) warnings based on low values of visual range (V_r). V_r has been defined in the context of how far away a black object has to be such that it is just noticeable or visible. This distance at which a landscape feature can just be detected is referred to as the V_r . AQI warnings are based on the levels of particulates ($PM_{2.5}$) resulting from fire smoke, often with less than 24-hr average concentrations. Because monitoring data are not available in all places where an AQI warning might potentially be given, human-observed visual conditions (i.e., sighting distant targets to determine V_r) have been used to estimate ambient fine particulate ($PM_{2.5}$) concentrations. This procedure, originally developed in the arid West, may be particularly questionable when applied where higher humidity (especially in the humid Southeast) interacts with background sulfate and nitrate particulates and other aerosols from non-fire sources to reduce visibility. Human errors estimating V_r can be large. One result may be that the public is given an incorrect impression of air quality risks to their health and well-being; either the AQI or other indices are overestimates, causing undue public alarm, or underestimates from which the public, or at least sensitive sections of the public, undergo avoidable risks.

The link between V_r and short-term (1–3 hr) $PM_{2.5}$ concentrations in smoky conditions was originally explored in a study performed in Helena, Montana, in the summer of 2000 (O'Neill et al., 2013). The study used a tapered element oscillating microbalance (TEOM) to measure particle concentrations under smoky conditions associated with wildfire and reported V_r estimations derived from the Automated Surface Observing System (ASOS) at the Helena airport. A curve fit between the two measurements suggested the relationship between V_r (in miles) and PM is $V_r * PM = 450$. If V_r is expressed in km, then $V_r * PM = 724$.

Helena is a city located in a wide, rural mountain valley where relative humidity and background air pollution are typically low, especially in the summer, which is when this analysis was conducted. As stated in O'Neill et al. (2013), this leads to two important caveats about the result of this study: first, it should only be applied if $RH < 65\%$, and second, it should only be applied when the majority of air pollution is from wildfire smoke. The inherent biases in TEOM and ASOS measurements will be discussed in another section of this report, but an obvious bias is that ASOS only measures scattering by aerosols and not absorption. A V_r observation is dependent on particle absorption, and the extinction coefficient associated with a smoke aerosol will have a significant absorption component.

O'Neill et al. (2013) report on an analysis in which they developed the following relationship between V_r and PM using the Interagency Monitoring of Protected Visual Environments (IMPROVE) program aerosol species concentration database: $V_r^{0.98} * PM = 622$. Here, V_r is expressed in km and PM is particle concentration less than $2.5 \mu m$ and in units of $\mu g/m^3$. The relationship is an average across all 166 IMPROVE monitoring sites, and they used the new

IMPROVE equation for estimating extinction as a function of particulate mass concentrations (Pitchford et al., 2007).

The U.S. Environmental Protection Agency (EPA), California Department of Public Health, California Office of Environmental Health Hazard Assessment, California Air Resources Board, and Missoula County Health Department co-authored a document titled “Wildfire Smoke, A Guide for Public Health Officials” (2008, http://oehha.ca.gov/air/risk_assess/wildfirev8.pdf), herein subsequently referred to as “the smoke guide”, which links V_r estimates to PM concentrations, which in turn are linked to air quality health index (AQI) categories. The following table from this document is reproduced in Table 1.1.

Table 1.1: Table linking AQI categories to ambient mass concentrations and visual range as reported in “Wildfire Smoke, A Guide for Public Health Officials” (2008).

Air Quality Index Category	PM _{2.5} or PM ₁₀ Levels (µg/m ³ , 1-3 hr avg)	PM _{2.5} or PM ₁₀ Levels (µg/m ³ , 8 hr avg)	PM _{2.5} or PM ₁₀ Levels (µg/m ³ , 24 hr avg)	Visibility-Arid Conditions (miles)
Good	0-38	0-22	0-12	≥11
Moderate	39-88	23-50	12.1-35.4	6-10
Sensitive Groups	89-138	51-79	35.5-55.4	3-5
Unhealthy	139-351	80-200	55.5-150.4	1.5-2.75
Very Unhealthy	352-526	201-300	150.5-250.4	1-1.25
Hazardous	>526	>300	>250.5	<1

The smoke guide also makes the following recommendations:

“Many communities do not have access to continuous PM monitoring, and therefore need other ways to estimate particle levels. This is true even in areas which do have continuous monitors, **because smoke concentrations can vary widely within a couple miles and can change rapidly. Visibility can sometimes serve as a good surrogate.** In addition, a visibility index gives the public a quick way to assess smoke levels for themselves.

When using the visibility index to determine smoke concentrations, it is important to:

- **Face away from the sun.**
- Determine the limit of your visibility range by looking for targets at known distances (miles). **The visible range is the point at which even high-contrast objects (e.g., a dark forested mountain viewed against the sky at noon) totally disappear.**
- After determining visibility in miles, use Tables 2 and 3 to identify potential health effects and appropriate cautionary statements.”

The underlined and bold text was for emphasis by the authors. These underlined statements are misleading and will be discussed in some detail below. However, a few summary points will be highlighted here. First, if smoke concentrations vary widely and are changing rapidly, then visibility should not be used and would not be a good surrogate to instrumental measures. It is

under these conditions in which the underlying assumptions that allow a linkage between V_r and atmospheric mass concentration (Koschmieder relationship, Middleton, 1952) are violated by hundreds of percent. Second, in the atmospheric assumptions that allow the use of a V_r -to-mass relationship, the viewing angle relative to the sun is not relevant. The sun can be behind, in front of, or overhead of the observer. Finally, the statement that an observer can use even high-contrast targets is misleading. The V_r -to-mass relationship as specified by the Koschmieder relationship can **only** be used for high-contrast targets or landscape features.

The V_r estimates in Table 1.1 (last column) only correspond to 1–3 hr concentrations. Other states use similar but different V_r , PM, and AQI index relationships. The relationship between V_r and 1-hr PM concentrations used by other states are summarized in Table 1.2, and Table 1.3 lists the PM concentrations associated with the V_r increments presented in the smoke guide and the associated mass increments predicted using the Montana and O’Neill V_r PM equations discussed above.

Table 1.2: Table of visual range–PM relationships used by various states and those listed in “Wildfire Smoke, A Guide for Public Health Officials” (2008).

Air Quality Index Category	Smoke guide (2008)		Montana (2013)		Colorado (2013)		Alaska (2013)	
	V_r (km)	Mass ($\mu\text{g}/\text{m}^3$)	V_r (km)	Mass ($\mu\text{g}/\text{m}^3$)	V_r (km)	Mass ($\mu\text{g}/\text{m}^3$)	V_r (km)	Mass ($\mu\text{g}/\text{m}^3$)
Good	17.71	38	21.41	33.6	16.1	40	16.1	40
Moderate	9.66	88	14.01	51.1	8.05	80	9.66	80
Sensitive Groups	4.83	138	8.05	88.6	4.83	175	4.83	175
Unhealthy	2.42	351	3.38	201	2.42	300	2.42	300
Very Unhealthy	1.61	526	2.09	338.5	1.61	500	1.21	500
Hazardous	<1.61	>526	<2.09	>338.5	<1.61	>500	<1.21	>500

Table 1.3: Table of visual range–PM relationships predicted by the Montana (2013) and O’Neill et al. (2013) equations, using the “Wildfire Smoke, A Guide for Public Health Officials” (2008) PM cutpoints.

Air Quality Index Category	Montana equation		O’Neill et al. equation	
	V_r (km)	Mass ($\mu\text{g}/\text{m}^3$)	V_r (km)	Mass ($\mu\text{g}/\text{m}^3$)
Good	17.71	40.88	17.71	35
Moderate	9.66	74.95	9.66	64
Sensitive Groups	4.83	149.90	4.83	129
Unhealthy	2.42	299.17	2.42	258
Very Unhealthy	1.61	449.69	1.61	386

The V_r versus PM relationships presented in Tables 1.2 and 1.3 are plotted in Figures 1.1 and 1.2. The information is plotted on linear scales in Figure 1.1, while in Figure 1.2 V_r is plotted on log scales to better emphasize the differences in mass concentrations. At high mass loadings or low V_r , the absolute mass differences between the various curves are greater than at low mass loadings.

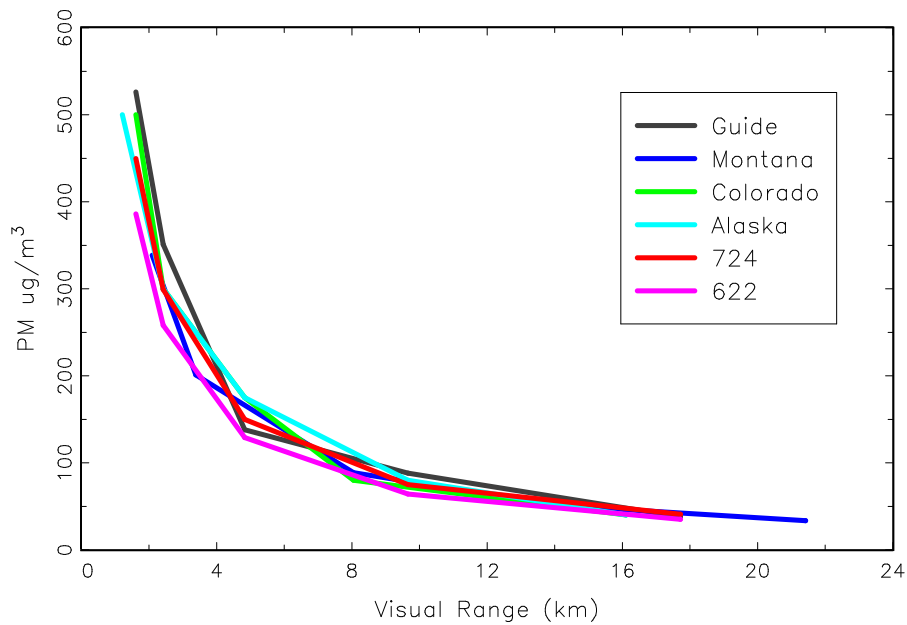


Figure 1.1: PM vs. visual range relationships used by various states, those recommended by “Wildfire Smoke, A Guide for Public Health Officials” (2008), and those predicted from the Montana (2013) and O’Neill et al. (2013) equations, plotted on linear scales.

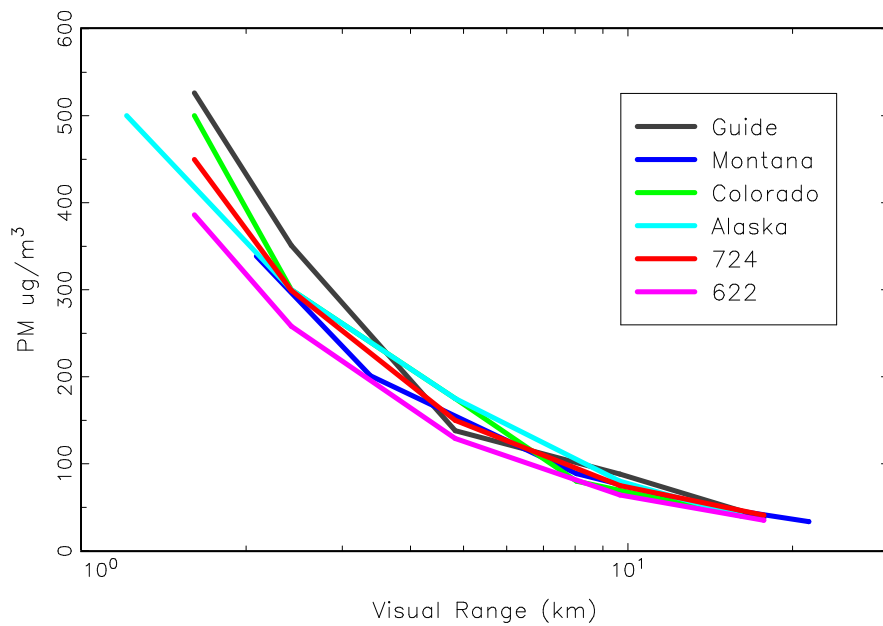


Figure 1.2: PM vs. visual range relationships used by various states, those recommended by “Wildfire Smoke, A Guide for Public Health Officials” (2008), and those predicted from the Montana (2013) and O’Neill et al. (2013) equations, plotted on log scales.

Because uncertainties in V_r judgments and PM concentrations relate to uncertainties more directly on a percentage basis, the data in Figure 1.3 are plotted as a percent difference between the various mass V_r breakpoints and the arbitrarily chosen Montana V_r PM equation as a function of V_r . The relationship presented on the Montana Department of Environmental Quality web site is about 30% lower on the average. The remaining relationships are quite similar to the reference relationship in that the differences are less than 20% and on the average only differ by about 10%.

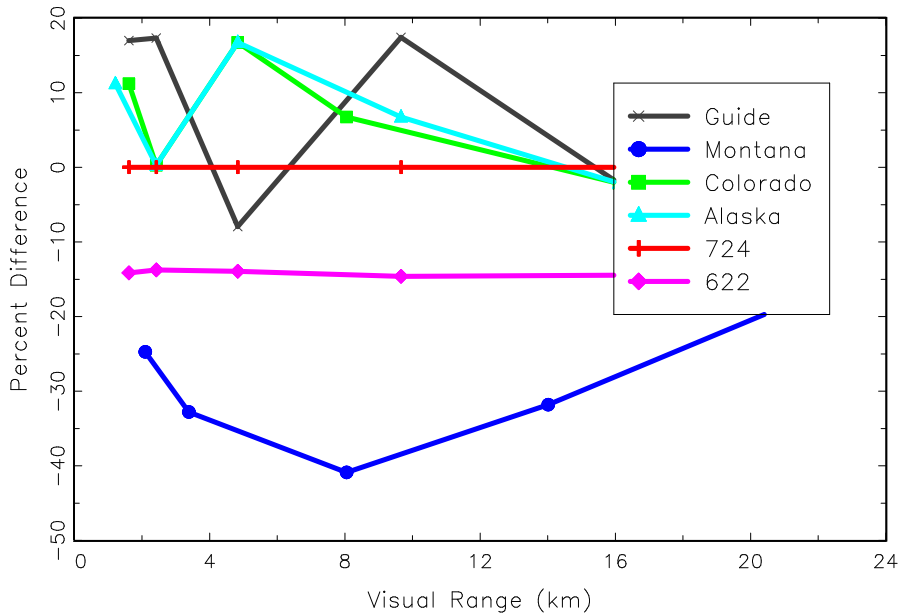


Figure 1.3: Percent differences between the PM levels predicted for a given visual range used by various states and those presented in “Wildfire Smoke, A Guide for Public Health Officials” (2008) and a reference value of $V_r * PM = 724$.

Not only are the relationships between V_r and PM concentrations variable between states and those recommended in the smoke guide, but the link between AQI and human health impacts and mass loadings vary substantial as well. Figure 1.4, presented in O’Neill et al. (2013), shows the varying relationships. However, this review will not address the relationship between health impacts and mass loadings but will focus on the ability to relate observed V_r to PM mass loadings.

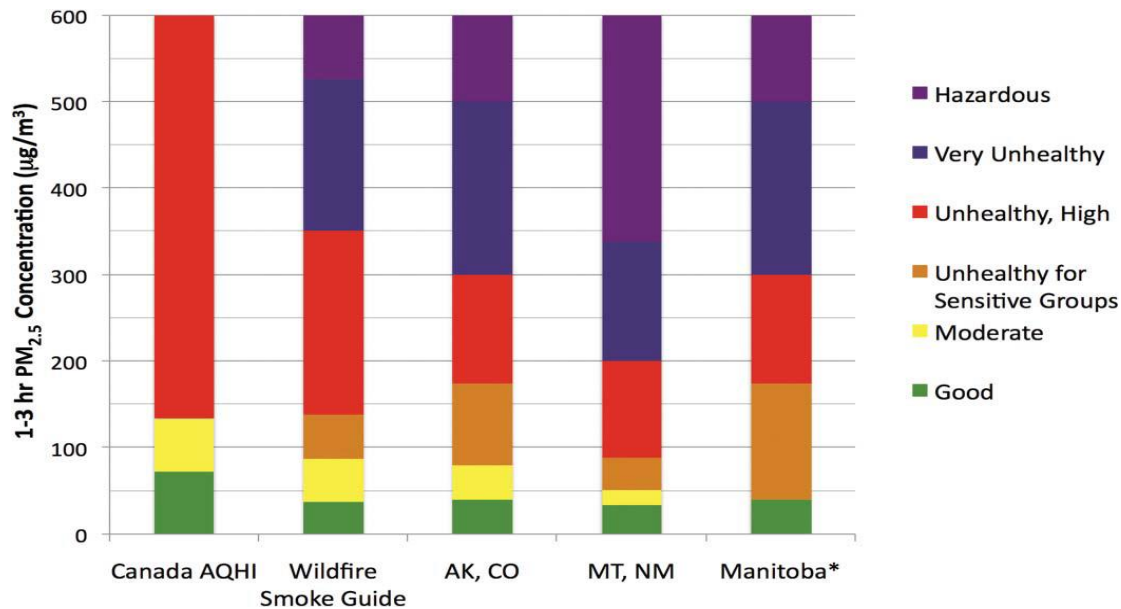


Figure 1.4: Summary of the relationships between human health impact categories and PM concentrations used by different agencies and states.

The underlying relationship between V_r and PM concentration proposed by O'Neill et al. (2013), the Montana (2013) equation, and those used by various states all rely on the assumption that $V_r * PM = CNST$ for all ambient conditions and for all parts of the United States. Objectives of the following analysis are to

1. examine the validity of a $V_r * PM = CNST$ relationship,
2. develop a physical- and chemical-based recommendation for the value of CNST,
3. assess the uncertainty in the CNST value, based on known physical and optical characteristics of an aerosol,
4. assess the effects of uncertainties in estimating V_r ,
5. examine how this relationship may change as a function of national annual average background conditions and as a function of season and location within the continental United States,
6. make recommendations for the form of the $V_r PM$ relationship and
7. make recommendations for using this equation under varied background and location differences.

2. UNCERTAINTY IN ESTIMATING AN OBSERVED VISUAL RANGE

2.1 Nomenclature and Fundamental Equations

That light scatters preferentially in different directions as a function of particle size is extremely important in determining the effects that atmospheric particulates have on a visual resource (Malm, 1979, 2000; Middleton, 1952). The angular relationship between the sun and the observer in conjunction with the size of particulates determines how much of the sunlight is redistributed into the observer's eye. These concepts are schematically represented in Figure 2.1. When the atmospheric particle concentration is more than a few $\mu\text{g}/\text{m}^3$ and the viewing angle is

such that the observer is looking in the direction of or away from the sun, Mie, or particle scattering, will dominate Rayleigh or molecular scattering. On the other hand, if the observer views a vista such that the scattering angle between the sun and observer is about 90° , Mie scattering may be on the order of or less than Rayleigh scattering, and in many cases the sky will appear blue.

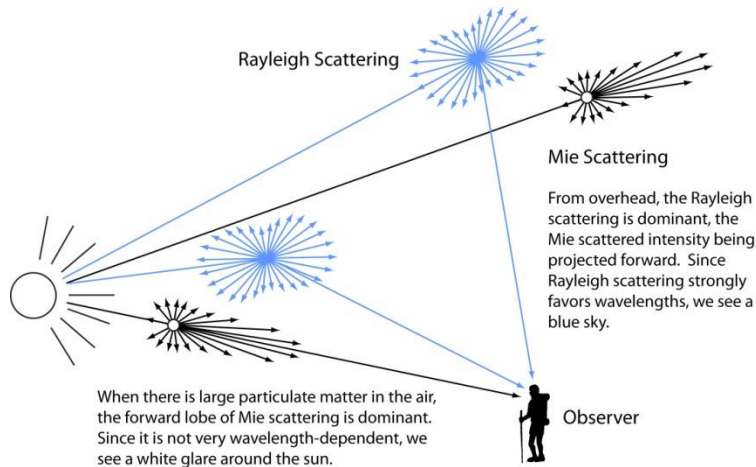


Figure 2.1: Schematic diagram contrasting how the effects of molecular volume scattering function on scattered radiation differ from those of the fine particle scattering function.

2.1.1 Quantifying the Transfer of Radiation through the Atmosphere

The alteration of radiant energy as it passes through the atmosphere is due to scattering and absorption by gases and particles. The effect of the atmosphere on the visual properties of distant objects theoretically can be determined if the concentrations and characteristics of air molecules, particles, and absorbing gases are known throughout the atmosphere and, most importantly, along the line of sight between the observer and object.

Radiometric concepts refer to radiant energy in a single wavelength, while photometric variables are radiant-energy-weighted in proportion to their ability to stimulate our sense of light.

Notations used here are similar to that used by Duntley et al. (1948). The basic symbol employed for the spectral radiance is N , and the symbol for luminance is B . In addition, the position in the atmosphere is denoted by \bar{r} . The direction of any path of sight is specified by a zenith-angle θ and an azimuth angle φ , the photometer being directed upward, $0 \leq \theta < \pi/2$, as in Figure 2.2; \bar{r} , θ , and φ are always written as parenthetic attachments to the parent symbol. When post-subscript r is appended to any symbol, it denotes that the quantity pertains to a path of length r . The subscript o always refers to the hypothetical concept of any instrument or observer located at zero distance from the object, as, for example, denoting the inherent radiance of a surface. Pre-subscripts identify the objects; pre-subscript b refers to background and l refers to landscape feature. Thus, the monochromatic, inherent spectral radiance of a landscape feature at positions \bar{r} as viewed in the direction (θ, φ) is ${}_l N_o(\bar{r}_l, \theta, \varphi)$. Post-superscript or post-subscript $*$ are employed as symbols signifying that the radiometric quantity has been generated by the scattering of ambient light reaching the path from all directions. Thus, $N_r^*(\bar{r}, \theta, \varphi)$ is the spectral

path radiance observed at position \bar{x} in the indicated direction, and $N_*(\bar{r}, \theta, \varphi)$ is used to denote the path function, two quantities to be defined later.

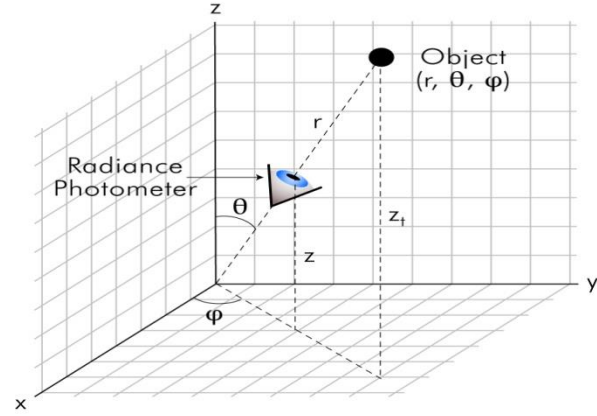


Figure 2.2: Illustrative geometry for a sight path.

Image-forming light is lost by scattering and absorption in each elementary segment of the path of sight, and contrast-reducing air light or path radiance is generated by the scattering of the ambient light that reaches the segment from all directions. The loss of image-forming light due to attenuation by scattering and absorption within any path segment is proportional to the amount of image-forming light present: the coefficient of proportionality is $b_{\text{ext}}(\bar{r})$, the attenuation or extinction coefficient at position \bar{r} . $b_{\text{ext}}(\bar{r})$ is a function of position within the path of sight; it does not depend upon the image transmission direction, it is independent of the manner in which the path segment is lit by the sun or sky, and it is a physical property of the atmosphere alone. Absorption refers to any thermodynamically irreversible transformation of radiant energy, including conversion of light into heat but also fluorescence and photochemical processes.

Attenuation by scattering results from any change of direction of radiant energy sufficient to cause the radiation to fall outside the area of detection, either by an eye or electro-optical detection device. Therefore,

$$b_{\text{ext}} = b_{\text{scat}} + b_{\text{abs}} = b_{\text{sg}} + b_{\text{ag}} + b_{\text{sp}} + b_{\text{ap}} \quad 2.1$$

where b_{scat} and b_{abs} are the atmospheric scattering and absorption coefficients, respectively. The scattering coefficient is further broken down into scattering by gases b_{g} and particles b_{sp} . Likewise, b_{ag} and b_{ap} refer to absorption by gases and particles, respectively (Van de Hulst, 1981).

Light does not scatter from gases or particles equally in all directions. Therefore,

$$b_{\text{scat}} = \int_{4\pi} \sigma(r, \beta) d\Omega \quad 2.2$$

where r and β are the position and scattering angles, respectively, while $d\Omega$ is an increment of solid angle and $\sigma(r, \beta)$ is defined as the volume scattering function. The volume scattering function is a measure of the atmosphere's ability to scatter light in a given direction.

The scattering function $\sigma'(r, \beta)$ is defined by

$$\sigma'(r, \beta) = \sigma(r, \beta)/b_{\text{scat}}(x) \quad 2.3$$

and, as such,

$$\int_{4\pi} \sigma'(r, \beta) d\Omega = 1 \quad 2.4$$

The scattering of light by air molecules, primarily nitrogen and oxygen, is typically referred to as Rayleigh scattering, named after the British physicist John William Strutt, more commonly known as Lord Rayleigh. Rayleigh scattering is applicable to spheres that are less than about 10 times the wavelength of the incident radiation, as is the case for sunlight incident on air molecules. The scattering is elastic in that the amount or energy of incident radiation is equal to that being scattered.

A schematic of how direct sunlight, reflected sunlight, and diffuse radiation affect the seeing of landscape features is shown in Figure 2.3. Image-forming information is lost by the scattering of imaging radiant energy out of the sight path and absorption within the sight path, while ambient light scattered into the sight path adds radiant energy to the observed radiation field. This process is described by

$$\frac{dN_r(\theta, \varphi, \vec{r})}{dr} = -b_{\text{ext}} N_r(\theta, \varphi, \vec{r}) + N_*(\theta, \varphi, \vec{r}) \quad 2.5$$

(loss) (gain)

where $N_r(\theta, \varphi, \vec{r})$ is the apparent radiance at some vector distance r from a landscape feature, $N_*(\theta, \varphi, \vec{r})$ (referred to as the path function) is the radiant energy gain within an incremental path segment, and $b_{\text{ext}}N_r(\theta, \varphi, \vec{r})$ is radiant energy lost within that same path segment. Although not explicitly stated, it is assumed that each variable in, and each variable derived from, equation 2.5 is wavelength dependent. The parenthetical variables $(\theta, \varphi, \vec{r})$ indicate that N_r and $N_*(\theta, \varphi, \vec{r})$ are dependent both on the direction of image transmission and the position within the path segment. For the sake of brevity, the parenthetical variables will be dropped in following equations. When the postscript r is appended to any symbol, it denotes that the quantity pertains to a path of length r . The subscript o always refers to the hypothetical concept of any instrument or observer located at zero distance from the object as, for example, in denoting the inherent radiance of a surface. Prescripts identify the objects, the prescript b referring to background and l to landscape feature.

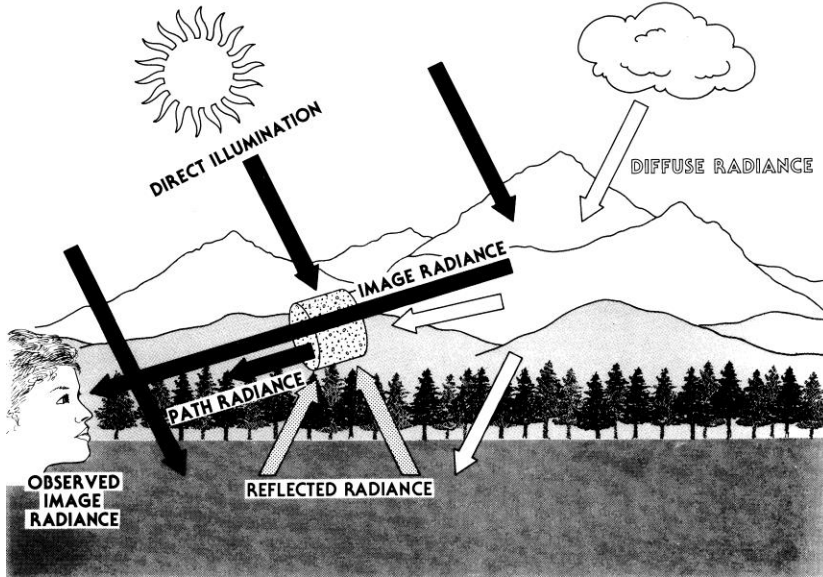


Figure 2.3: Diagram showing how path radiance and attenuated image-forming information combine to form the observed image at the eye of an observer. Direct, diffuse, and reflected radiance all contribute to illuminating the image, as well as the incremental volumes of atmosphere that sum to form sight-path radiance.

When N_r has some special value N_q , such that $b_{\text{ext}}N_q = N_*$, then $dN_q/dr = 0$. N_q is independent of r and is commonly referred to as the equilibrium radiance. Therefore, for every path segment

$$\frac{dN_r}{dr} = -b_{\text{ext}}(N_r - N_q). \quad 2.6$$

If N_q is constant, equation 1.6 can be integrated to yield

$$\frac{N_r - N_q}{N_o - N_q} = T_r \quad 2.7$$

where T_r is the transmittance over path length r and is given by

$$T_r = e^{-\int_0^r b_{\text{ext}}(r)dr}. \quad 2.8$$

Rearranging equation 2.7 yields

$$N_r = N_o T_r + N_q(1 - T_r) \quad 2.9$$

where the first term on the right of equation 2.9 is the residual image-forming radiance, while the second term is the path radiance (airlight) N_r^* , which results from scattering processes throughout the sight path. The parameter N_r^* is the sky radiance when $r = \infty$,

$$N_{\infty}^* = N_q(I - T_{\infty}). \quad 2.10$$

If T_{∞} is approximately zero, then $N_q = N_{\infty}^* = N_s$ and

$$N_r^* = N_s(I - T_r) \quad 2.11$$

where N_s is sky radiance. Equation 2.11 allows for a simple approximation of N_r^* when N_s is known.

The explicit dependence of N_r^* on illumination and directional scattering properties of the atmosphere given by

$$N_r^* = \int_0^r N^* T_r dr \quad 2.12$$

where

$$N^* = h_s \sigma + \int_{4\pi} N \sigma d\Omega. \quad 2.13$$

where N is the apparent radiance of the sun, sky, clouds, or ground and $d\Omega$ is an element of solid angle. The parameter h_s is sun irradiance, and σ is the volume scattering function.

2.1.2 Contrast and Contrast Transmittance

Any landscape feature can be thought of as consisting of many small pieces, or elements, with a variety of physical characteristics. For instance, the reflectivity of an element as a function of wavelength, along with characteristics of the incident radiation, determines its color and brightness. The brightness of a scenic element at some observing distance and at one wavelength is referred to as monochromatic apparent spectral radiance. The monochromatic apparent spectral radiance of any scenic element is given according to equation 2.6 by

$${}_l N_r = T_{rl} N_o + N_r^* \quad 2.14$$

where N_r^* is substituted explicitly for $N_q(1-T_r)$. The subscript l indicates that the radiance is associated with a specific uniform scenic landscape feature.

A scenic element is always seen against some background, such as the sky or another landscape feature. The apparent and inherent background radiances are related by an expression similar to equation 2.14:

$${}_b N_r = T_{rb} N_o + N_r^* \quad 2.15$$

Subtracting equation 2.15 from equation 2.14 yields the relation

$$[{}_l N_r - {}_b N_r] = T_r [{}_l N_o - {}_b N_o]. \quad 2.16$$

Thus, radiance differences are transmitted along any path with the same attenuation as that experienced by each image-forming ray.

The image-transmitting properties of the atmosphere can be separated from the optical properties of the object by the introduction of the contrast concept. The inherent spectral contrast C_o of a scenic element is, by definition,

$$C_o = [{}_l N_o - {}_b N_o] / {}_b N_o. \quad 2.17$$

The corresponding definition for apparent spectral contrast at some distance r is

$$C_r = [{}_l N_r - {}_b N_r] / {}_b N_r. \quad 2.18$$

If equation 2.16 is divided by the apparent radiance of the background ${}_b N_r$ and combined with equations 2.17 and 2.18, the result can be written as

$$C_r = C_o \frac{{}_b N_o}{{}_b N_r} T_r. \quad 2.19$$

Substituting equation 2.15 for ${}_b N_r$ and rearranging yields

$$C_t \equiv C_r / C_o = 1 / [1 + N_r^* / {}_b N_o T_r]. \quad 2.20$$

The right-hand member of equation 2.20 is an expression for the contrast transmittance C_t of the path of sight. Equation 2.20 is the law of contrast reduction by the atmosphere, expressed in the most general form. It should be emphasized that equation 2.20 is completely general and applies rigorously to any path of sight, regardless of the extent to which the scattering and absorbing properties of the atmosphere or the distribution of lighting exhibit nonuniformities from point to point.

2.1.3 Visual Range and Contrast

V_r has historically has been defined in the context of how far away a black object has to be such that it is just noticeable or visible. The distance at which a large dark landscape feature can just be detected is referred to as the visual range (V_r).

Starting with the contrast reduction equation

$$C_r = C_o \frac{{}_b N_o}{{}_b N_r} e^{-\bar{b}_{ext} r} = C_o \gamma e^{-\bar{b}_{ext} r}. \quad 2.21$$

where $\gamma = {}_bN_o/{}_bN_r$ and \bar{b}_{ext} is the average extinction over sight path r . Assuming the background is the sky (${}_bN_o = {}_sN_o$ and ${}_bN_r = {}_sN_r$), and further assuming the sky radiance at the observer and landscape feature are the same ($\gamma = 1$), equation 2.21 reduces the familiar Koschmeider relationship (Middleton, 1952):

$$C_r = C_o e^{-\bar{b}_{ext} r}. \quad 2.22$$

Solving equation 2.21 for \bar{b}_{ext} yields

$$\bar{b}_{ext} = -\frac{1}{r} \ln C_r / \gamma C_o. \quad 2.23$$

It should be emphasized that \bar{b}_{ext} is the average extinction coefficient of the atmosphere between the observer and landscape feature when they are separated by a distance equal to r .

Let $V_r \equiv r$ be the distance from a feature at which a threshold contrast of ε is achieved. Equation 2.23 can then be written as

$$V_r = -\frac{1}{\bar{b}_{ext, V_r}} \ln \frac{-\varepsilon}{C_o \gamma}. \quad 2.24$$

This relationship is the defining equation for a "monochromatic" V_r of an object with an inherent contrast equal to C_o . In this equation, \bar{b}_{ext, V_r} is the average attenuation coefficient between the observer and a landscape feature that is at a distance sufficient to reduce its apparent contrast to ε . It is not the same b_{ext} as determined by equation 2.23, unless $C_r = \varepsilon$ and r is equal to the V_r (b_{ext} may be a function of r). For a black object, $C_o = -1$, and equations 2.23 and 2.24 become

$$\bar{b}_{ext} = -\frac{1}{r} \ln(-C_r / \gamma) \quad 2.25$$

and

$$V_r = -\ln(-\varepsilon / \gamma) / \bar{b}_{ext, V_r}. \quad 2.26$$

Equation 2.26 allows the contrast reduction equation represented by equation 2.22 to be written as

$$C_r = C_o e^{-\ln(-\varepsilon) r / V_r}. \quad 2.27$$

If the earth is assumed to be flat, if the atmospheric particle distribution is horizontally homogeneous, if the object is viewed at a zenith angle of 90° , and if the object is viewed under a cloudless sky (or uniform illumination), then $\gamma = 1$ (the sky radiance at the landscape feature and sky radiance at the observation point are equal) and $\bar{b}_{ext} = \bar{b}_{ext, V_r} = b_{ext}$. If these assumptions are met, equation 2.26 yields

$$V_r = -\ln(-\varepsilon)/b_{ext} \quad 2.28$$

Sometimes this equation is further simplified by ignoring the absorption component of the extinction coefficient or assuming that it is equal to zero. Then,

$$V_r = -\ln(-\varepsilon)/b_{sp} \quad 2.29$$

Much of the early visibility perception research concentrated on quantifying ε , the contrast between an object and its background that is "just noticeable" or visible. If ε , the threshold contrast, is taken to be -0.02, then equation 1.28 becomes

$$V_r = 3.912/b_{ext} \quad 2.30$$

Equation 2.30 allows V_r data to be interpreted in terms of extinction and, vice versa, extinction measurements to be interpreted in terms of V_r . Equation 2.30 implies that if the atmosphere is in optical equilibrium and the zenith angle is 90° , that is to say $\gamma = 1$, the V_r is independent of sun angle. When one looks toward or away from the sun, the distance at which a large, black landscape feature can be just seen is the same.

2.1.4 Standard Visual Range

In equation 2.30, b_{ext} is the sum of Rayleigh and particle scattering and extinction; Rayleigh scattering varies with altitude and temperature. Because it is desirable at times to compare across monitoring networks V_r estimations that are directly reflective of atmospheric extinction other than Rayleigh scattering, it is convenient to define a V_r that is normalized to some constant b_{sg} . This normalized V_r is referred to as standard visual range (V_{SVR}) and is defined as

$$V_{SVR} = 3.912/(b_{sp} + b_{ap} + b_{ag} + 0.01) \quad 2.31$$

where b_{sg} has been set equal to 0.01 km^{-1} .

2.1.5 Relationship between Visual Range and Atmospheric Mass Concentration

Assuming an externally mixed aerosol, the extinction coefficient and mass concentration are related to each other by

$$b_{ext} = \alpha m + b_{sg} \quad 2.32$$

where α is the average mass extinction coefficient for an ambient aerosol. It includes total mass (fine + coarse) plus water. If the aerosol is externally mixed,

$$\alpha m = \sum_i \alpha_i m_i \quad 2.33$$

where α_i and m_i are the mass extinction efficiencies associated with each aerosol species and m_i is the aerosol species concentrations.

Equation 2.33 also holds for an internally mixed aerosol in which the chemical species are mixed in fixed proportions to each other, the index of refraction is not a function of composition or size, and the aerosol density is independent of volume. When computing total extinction using Mie theory, the microscopic structure of the aerosol (that is, the extent of internal or external mixing) is found to be relatively unimportant, so that the assumption of internally versus externally mixed particles does not have much impact on the predicted results (White, 1986). The mass extinction (or scattering) efficiency is a stronger function of density and size than optical properties such as refractive index.

Equation 2.33 implies

$$\alpha = \sum_i \alpha_i \frac{m_i}{m} \quad 2.34$$

where the average mass extinction coefficient α is just the mass-weighted extinction efficiencies associated with each species' mass extinction efficiencies. The mass extinction efficiencies as written in equation 2.32 include the effects of water. The inflation of α associated with water can be written as

$$\alpha_{i,w} = \alpha_{i,dry} f(RH) \quad 2.35$$

and will be referred to as the wet mass extinction efficiency (Tang et al., 1981; Sloane and Wolff, 1985; Malm et al., 2005a, 2005b). $f(RH)$ is a function of RH that accounts for the increase in scattering cross sections associated with absorbed water on hygroscopic aerosol species such as sulfate and nitrate particles. Under high relative humidity conditions, $f(RH)$ can exceed 5 or more.

Substituting equation 2.32 into equation 2.30 yields

$$V_r = \frac{3.912}{\alpha m + b_{sg}}. \quad 2.36$$

Equation 2.31 expresses V_r in terms of atmospheric mass concentration. Rearranging yields

$$m = \frac{3.912}{\alpha V_r} - \frac{b_{sg}}{\alpha} = \frac{3.912/\alpha}{V_r} - \frac{b_{sg}}{\alpha}. \quad 2.37$$

For low V_r s, the term $\frac{3.912/\alpha}{V_r}$ in equation 2.36 is much greater than $\frac{b_{sg}}{\alpha}$; under these conditions equation 2.36 can be written as $m = \frac{3.912/\alpha}{V_r}$, which is the form of the O'Neill and Montana V_r PM relationships, with V_r PM = CNST, where CNST = 3.912/ α . If the units of V_r are in km, PM in $\mu\text{g}/\text{m}^3$, and α in m^2/gm , then CNST = 3912/ α .

Equation 2.36 shows that, as a limiting case, when smoke aerosol concentrations increase, the atmospheric extinction coefficient and thus V_r become primarily dependent on smoke aerosol concentration. In this limiting case, the relationship between V_r and aerosol concentration is

dependent on the choice of the smoke mass extinction coefficient α_s . The variability of α_s as a function of fuel type, age of smoke plume, and humidity will be discussed in another section.

The two relationships, $m = 724/V_r$ and $m = 622/V_r$, can be checked to see if they are physically reasonable since $3912/\alpha = 724$ and 622 . If $CNST = 3912$ (contrast threshold of -0.02), then $\alpha = 5.4 \text{ m}^2/\text{gm}$ and $6.3 \text{ m}^2/\text{gm}$, respectively. An α of either 5.4 or $6.3 \text{ m}^2/\text{gm}$ is physically possible, depending on background conditions and the physical optical properties of the smoke aerosol. For an inorganic aerosols such as sulfates and nitrates, an α above $5 \text{ m}^2/\text{gm}$ implies a high RH and water absorption. On the other hand as will be discussed later, a smoke aerosol that both scatters and absorbs and is weakly hygroscopic can have mass extinction efficiencies well above $5 \text{ m}^2/\text{gm}$.

2.2 Estimated Mass Concentration Dependence on Lighting Conditions and Haze Distribution

2.2.1 Uniformly Distributed Haze

Apparent contrast with some limiting assumptions can be used to estimate atmospheric extinction, either of the ambient atmosphere or the transmittance (opacity = $1/T$) of a plume (Malm, 1979). Figure 2.4 outlines the measurement of a sky-landscape feature's C_r .

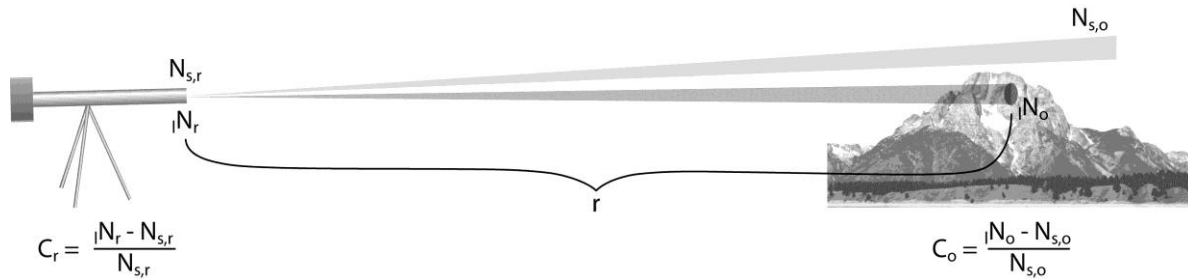


Figure 2.4: Schematic of a teleradiometer measurement of sky/landscape apparent contrast.

If the sky at the landscape feature and observation point are equal ($\gamma = 1$) and if C_o is known, b_{ext} can be easily calculated. However, $\gamma = 1$ requires assumptions that are not usually met. The first criterion that must be met is uniform illumination between the observer and basically infinity. In the presence of cloud fields this rarely happens. Second, in a clean background atmosphere, the earth's curvature will result in an atmosphere where $\gamma \neq 1$, as will an observation zenith angle other than 90° . And then there is the variability of C_o as the sun's illumination of the landscape feature changes throughout the day, cloud cover shadows the landscape, and in the case of natural landscape features, vegetation changes from one season to another, as do things such as snow cover. The uncertainty associated with some of these assumptions will be addressed in the next section.

If $\bar{b}_{ext} = b_{ext}$, then

$$b_{ext} = -\frac{1}{r} \ln(C_r/C_o\gamma) \quad 2.38$$

Equation 2.38 relates the sky landscape feature contrast to the extinction between that landscape feature and observer.

Equation 2.38 can be expressed in terms of atmospheric mass concentration assuming $b_{ext} = \alpha m + b_{sg}$. Substituting this mass extinction relationship into equation 2.35 yields

$$m = -\frac{1}{\alpha r} \ln(C_r/C_o\gamma) - \frac{b_{sg}}{\alpha}. \quad 2.39$$

Equation 2.39 allows for a measurement or judgment of apparent contrast to be interpreted in terms of atmospheric mass concentration.

If V_r is defined as the distance r at which C_r equals some threshold contrast ϵ , and it is assumed that the landscape feature is black ($C_o=-1$), then equation 2.38 becomes

$$b_{ext} = -\frac{1}{V_r} \ln(-\epsilon/\gamma). \quad 2.40$$

If it is further assumed that the threshold contrast ϵ is -0.02, then

$$b_{ext} = -\frac{1}{V_r} \ln(0.02/\gamma) \quad 2.41$$

and equation 2.39 becomes

$$m = \frac{-\ln(0.02/\gamma)}{\alpha V_r} - \frac{b_{sg}}{\alpha} \quad 2.42$$

Equation 2.42 is the same as equation 2.32, assuming $\gamma = 1$.

2.2.2 Nonuniform Smoke Haze – Haze between Observer and Landscape Feature

Consider the case where a smoke haze layer or plume is dispersed between the observer and landscape feature. The landscape feature has a radiance at the eye of $N_p^* + {}_lN_oT_p$, where ${}_lN_o$ is the landscape feature inherent radiance, T_p is the transmittance of the haze layer or plume between the landscape feature and observer, and N_p^* is the plume or haze layer path radiance. The sky radiance at the observer is just the sum of the attenuated sky radiance at the landscape feature and plume path radiance, ${}_sN_oT_p + N_p^*$. Therefore the contrast of the landscape feature at the observer is

$$C_r = \frac{{}_lN_o - {}_sN_o}{{}_sN_o} = \frac{(N_p^* + {}_lN_oT_p) - ({}_sN_oT_p + N_p^*)}{({}_sN_oT_p + N_p^*)} \quad 2.43$$

$$C_r = \frac{({}_lN_o - {}_sN_o)}{({}_sN_oT_p + N_p^*)} T_p. \quad 2.44$$

Solving for T_p , the plume transmittance,

$$T_p = \frac{N_p^* C_r}{{}_l N_o - {}_s N_o (C_r + 1)}. \quad 2.45$$

Using equations 2.37 and 2.41 and solving for M, the average mass concentration of the smoke plume between the observer and landscape feature, one finds

$$m = -\frac{1}{\alpha r} \ln \left[\frac{N_p^* C_r}{{}_l N_o - {}_s N_o (C_r + 1)} \right] - \frac{b_{sg}}{\alpha}. \quad 2.46$$

If C_r is taken to be 0.02, then $r = V_r$. The ratio ${}_s N_o / N_p^*$ should be compared to $\gamma = {}_s N_o / {}_s N_r$ in equation 2.21. They essentially are the same variable, the ratio of the sky above the landscape feature to the landscape feature sky radiance. In the case of a plume or spatially limited distribution of haze between the landscape feature and observer, the sky radiance at the observer is just the plume apparent radiance, while in both cases the sky radiance at the landscape feature is the same. What cannot be explicitly explained here is the difference between the sky radiance at the observer and landscape feature. Even in the case of horizontally uniform haze, if the observation or zenith angle is something other than 90° , these two variables can be quite different. In the case of a plume, the denominator of the variable γ is the path radiance of the plume, which will be quite different from the equilibrium sky radiance observed above the landscape feature being viewed. The next section will explore the effect of assuming a hypothetical difference in these radiances.

2.3 Uncertainty in Mass Estimate Associated with Use of the Koschmieder Relationship

2.3.1 Uncertainty Associated with Nonuniform Lighting or Aerosol Distribution.

First, assume that the landscape feature is approximated by a black object where ${}_l N_o = 0.0$. Figures 2.5 and 2.6 are plots of the distance to an object that has just reached its threshold contrast, which is the V_r , and the corresponding ambient mass concentration is estimated using equation 2.46. α is set equal to $4.52 \text{ m}^2/\text{gm}$ and $b_{sg} = 10 \text{ Mm}^{-1}$. If N_p^* is considered to be a factor of 6 greater than ${}_s N_o$, then $\gamma \approx 0.17$. This corresponds to a forward scattering geometry and a plume aerosol concentration of approximately $250 \text{ }\mu\text{g}/\text{m}^3$. In a backscatter case, the ratio would be greater than 0.17 and quite possibly positive.

Figure 2.5 is a linear plot of m versus V_r for $\gamma = 1$ and 0.17 as well as the mass difference between the assumption of $\gamma = 1$ and 0.17. Figure 2.6 corresponds to the same data but plotted on a log-log scale. The green graph refers to the estimated mass with $\gamma = 0.17$, the red graph corresponds to $\gamma = 1.0$, and the graph labeled ‘‘Uncertainty’’ is the difference between the mass estimates, assuming $\gamma = 0.17$ and $\gamma = 1.0$. On a log-log scale, the relationship between V_r and PM is easier to visualize at higher PM and low V_r values. Notice that for any PM value the uncertainty is about half the PM level, which corresponds to an overall uncertainty of approximately 50%, independent of V_r or PM level. Of course, for different observer sun angles and landscape geometries, the uncertainty will vary. The uncertainty could be considerably greater, and under conditions less ideal than those assumed here, it could be less. However, for purposes of this report, the uncertainty in estimated ambient mass concentrations due to

nonuniform lighting and mass concentration distributions estimated from an observed V_r will be assumed to be about 50%.

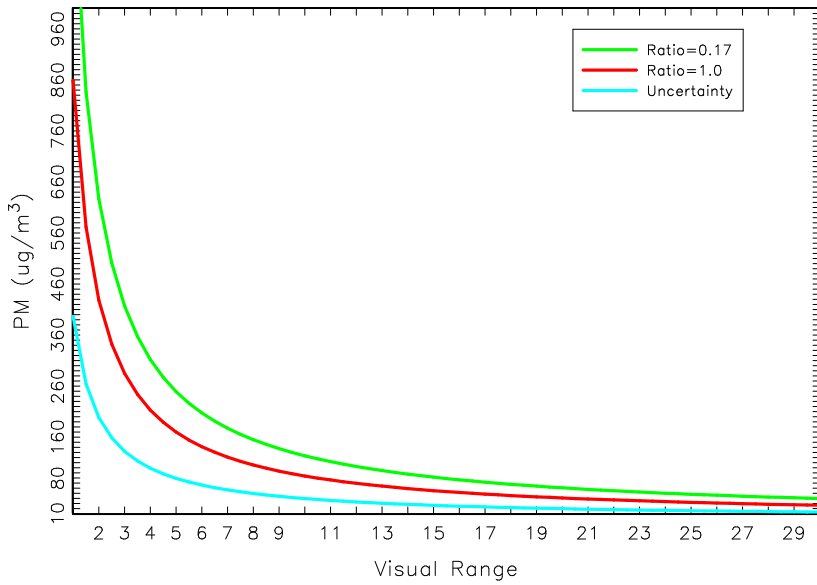


Figure 2.5: Plot of PM as estimated using equation 1.43 as a function of VR. The green graph refers to the estimated mass with $\gamma = 0.17$, the red graph corresponds to $\gamma = 1.0$, and the line labeled “Uncertainty” is the difference between the mass estimates, assuming $\gamma = 0.17$ and $\gamma = 1.0$.

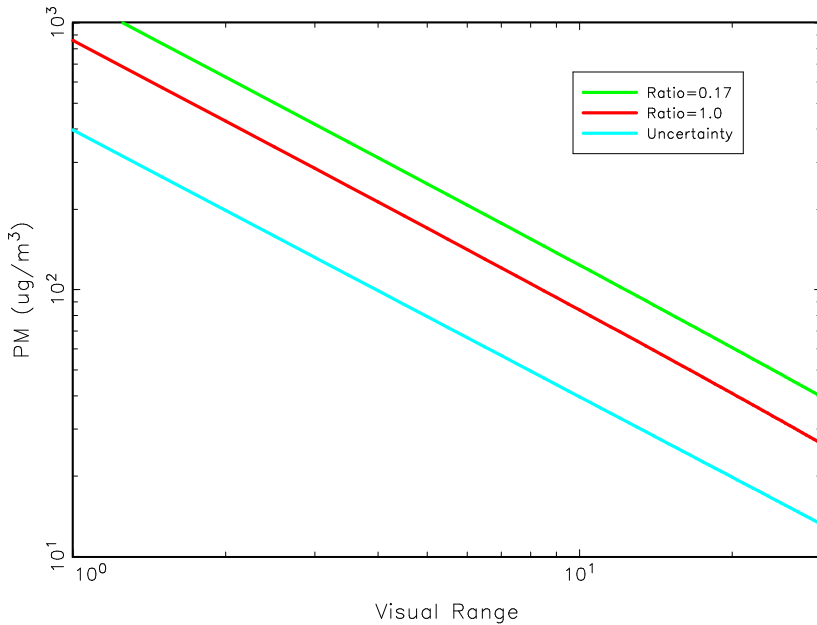


Figure 2.6: Same plot as Figure 2.5, but on a log-log scale. The green graph refers to the estimated mass with $\gamma = 0.17$, the red graph corresponds to $\gamma = 1.0$, and the line labeled “Uncertainty” is the difference between the mass estimates, assuming $\gamma = 0.17$ and $\gamma = 1.0$.

2.3.2 Uncertainty in Estimated Mass Associated with Uncertainty in C_o

Equation 2.36 is a general equation that relates apparent and inherent contrast and the ratio of sky radiance at the landscape feature and observer to atmospheric mass concentration.

Differentiating equation 2.36 with respect to C_o ,

$$\frac{dm}{dC_o} = \frac{1}{\alpha r C_o}. \quad 2.47$$

Dividing equation 2.47 by equation 2.32 expresses the uncertainty in estimated mass in terms of the uncertainty in C_o as a function of V_r :

$$\frac{dm}{m} = \frac{\frac{dC_o}{C_o}}{\frac{r3.912}{V_r} - r b_{sg}} \quad 2.48$$

and when $r = V_r$, then equation 2.48 reduces to

$$\frac{dm}{m} = \frac{\frac{dC_o}{C_o}}{3.912 - V_r b_{sg}}. \quad 2.49$$

Equation 2.49 can be used to approximate the uncertainty in a mass estimate due to an uncertainty in C_o at some V_r or mass loading. For a tree-covered landscape feature judged to be at the V_r that is assumed to be black, dm/m is at least a 50%. If the landscape feature is rock-covered or tree-free and covered in grass, such as a meadow, the error is significantly greater and will vary depending on sun angle. Equation 2.32 was used to estimate m at some V_r in Figure 2.7, which is a plot of dm/m , predicted by equation 2.49, as a function of m , assuming $dC_o/C_o = 0.5$.

Error From C_o Uncertainty

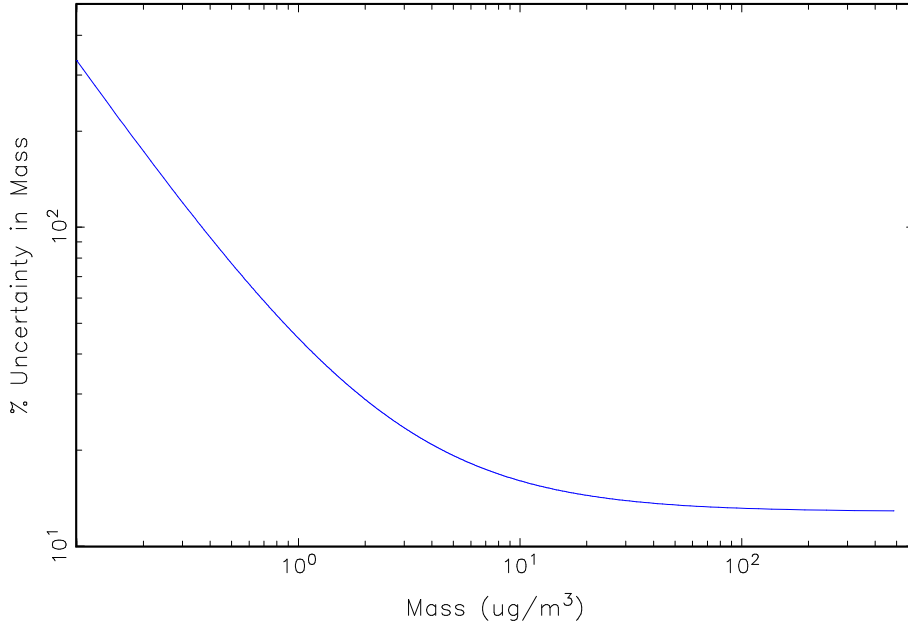


Figure 2.7: Uncertainty in estimated mass dm/m as a function of m and uncertainty in C_o of 50%.

At high mass loadings, the uncertainty is about 15%, while at lower mass loadings, the uncertainty is much greater. For the lowest health breakpoint, the uncertainty in an estimated mass will be on the order of 20%.

2.3.3 Uncertainty Associated with Contrast Judgments

The limitations of using V_r to estimate ambient atmospheric mass concentrations associated with the ability of a human observer to estimate some level of contrast can be explored using Webers Law (Ross and Murray, 1996)

Webers law states that

$$\Delta C = kC \quad 2.50$$

where C is vista sky contrast and k is some proportionality constant. Therefore

$$\Delta C / C = k. \quad 2.51$$

Equation 2.51 states that a fractional change in apparent contrast is perceived to be the same, independent of the initial contrast. Assuming the threshold contrast $\epsilon = -0.02$ and differentiating equation 2.33 yields

$$\frac{dC_r}{dV_r} = -C_o \frac{3.912 r}{V_r^2} e^{-const r/V_r} \quad 2.52$$

$$\frac{dC_r}{C_r} = \frac{3.912 r}{V_r^2} dV_r . \quad 2.53$$

If $r = V_r$, that is, the landscape feature is at the VR, then $r/V_r = 1$, and invoking equation 2.51 yields

$$\frac{dC_r}{C_r} = 3.912 \frac{dV_r}{V_r} = k \quad 2.54$$

That is, a percent change in V_r is perceived to be constant for any VR. A satisfying relationship!

$$\frac{dV_r}{V_r} = k/3.912 \quad 2.55$$

Now, differentiating equation 2.32 with respect to V_r yields

$$\frac{dm}{dV_r} = -\frac{3.912}{\alpha} \frac{1}{V_r^2} \quad 2.56$$

Dividing equation 2.56 by equation 2.32 and rearranging results in an expression relating a fractional change in mass to a V_r :

$$\frac{dm}{m} = -\frac{\frac{dV_r}{V_r}}{1 - \frac{V_r b_{sg}}{3.912}} = -\frac{k}{3.912 - V_r b_{sg}} \quad 2.57$$

Notice that equation 2.57 is functionally the same as equation 2.49, which relates the uncertainty in C_o to estimated mass uncertainty as a function of mass concentration or V_r . Equation 2.57 states that a percent change in mass is a function of a negative percent change in V_r , and a perceived percent change in V_r is the same for all V_r if the landscape feature is at a distance equal to the V_r . For a small V_r (high mass loadings), the fractional uncertainty in mass equals the fractional uncertainty in V_r , or $k/3.912$ as defined above, and infinity is at $m = 0$, or at the Rayleigh limit.

Equations 2.57 and 2.32 are used to estimate mass as a function of V_r for Figure 2.8, which is a plot of the percent uncertainty in a mass estimate, dm/m , based only on the ability of an observer to judge whether the contrast is at the assumed limit of visibility. Assuming a 20% uncertainty in V_r estimation or determination implies a 20% uncertainty in mass estimation at high mass levels (anything above $100 \mu\text{g}/\text{m}^3$) and higher uncertainties at low concentrations.

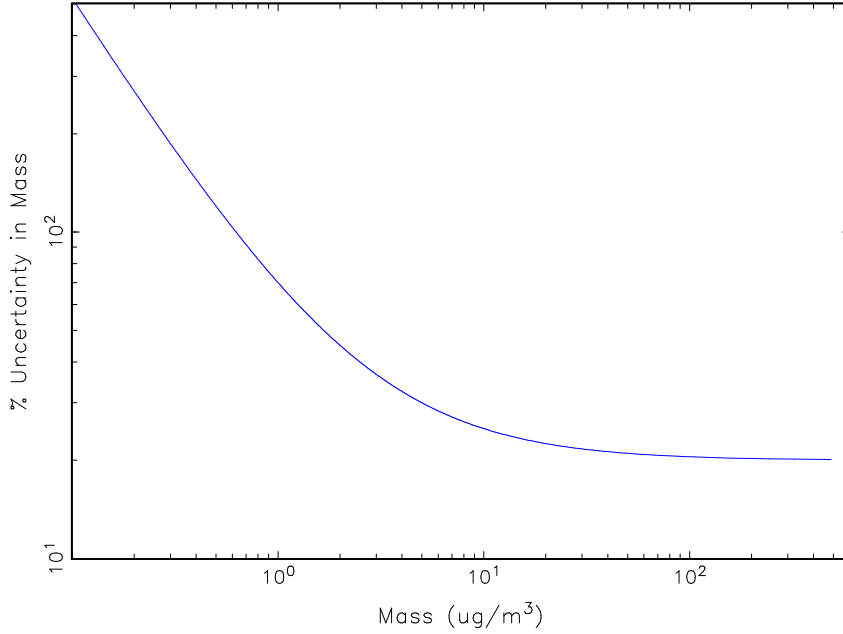


Figure 2.8: A plot of uncertainty in mass estimates, dm/m , as a function of ambient mass concentration, based on the ability of an observer to determine whether a landscape feature has reached the threshold contrast of -0.02.

3. DERIVING MASS SCATTERING EFFICIENCY FROM MEASUREMENTS OF ATMOSPHERIC SCATTERING AND MASS CONCENTRATIONS.

Assuming that

$$V_r = -\ln(-\varepsilon)/b_{ext} \quad 3.1$$

where V_r is visual range, b_{ext} is atmospheric extinction, and ε is the threshold contrast of some landscape feature viewed against a background sky and

$$b_{ext} = \alpha m + b_{sg} \quad 3.2$$

where α and m are wet mass extinction efficiency and total mass concentration, including coarse mass, respectively, and b_{sg} is atmospheric scattering due to naturally occurring gases in the atmosphere, then substituting equation 3.2 into 3.1 yields

$$V_r = -\ln(-\varepsilon)/(\alpha m + b_{ray}). \quad 3.3$$

Dividing through by α yields

$$V_r = \frac{-\ln(-\varepsilon)}{\alpha} \bigg/ \left(m + \frac{b_{ray}}{\alpha} \right). \quad 3.4$$

For $m \gg \frac{b_{ray}}{\alpha}$,

$$V_r = \frac{-\ln(-\varepsilon)}{\alpha} / m = CNST/m. \quad 3.5$$

Integrating nephelometers have been operated at a number of IMPROVE sites. The concurrent datasets of measured b_{scat} and fine and coarse mass allow for a site by site estimation of the relationship between V_r and mass. Table 3.1 is a list of lat/lon coordinates for those IMPROVE monitoring stations with concurrent integrating nephelometer and particle measurements.

Table 3.1: List of IMPROVE sites with nephelometer and particle data.

Site	Longitude	Latitude
MORA	-123.274	46.7579
THSI	-123.226	44.291
SNPA	-122.857	47.4204
CORI	-122.614	45.6678
JARB	-119.256	41.8926
PHOE	-117.257	33.5038
HANC	-117.19	35.9731
SYCA	-117.182	35.1406
IKBA	-117.009	34.3403
LOPE	-116.776	40.4449
GICL	-114.941	33.2204
BIBE	-111.907	29.3028
UPBU	-105.922	35.8259
BOWA	-104.898	47.9464
MACA	-101.689	37.1315
SENY	-101.568	46.2881
GRSM	-100.365	35.6334
OKEF	-99.277	30.7404
DOSO	-97.6558	39.107
SHEN	-97.0608	38.5229
ACAD	-90.9567	44.3771

Taking the natural log of equation 3.5 yields

$$\ln(V_r) = \ln\left(\frac{-\ln(-\varepsilon)}{\alpha}\right) - \ln\left(m + \frac{b_{ray}}{\alpha}\right). \quad 3.6$$

A curve fit between V_r and m is carried out using

$$\ln(V_r) = a_0 - \ln(m + a_1). \quad 3.7$$

Comparing equation 3.7 to equation 3.6 shows that

$$a_0 = \ln\left(\frac{-\ln(-\varepsilon)}{\alpha}\right) \text{ and } a_1 = \frac{b_{ray}}{\alpha}. \quad 3.8$$

The advantage of doing the curve fit on the transformed equation is to derive more equal weighting between high and low mass numbers.

Figure 3.1 shows scatterplots of V_r derived from nephelometer measurements and PM, as well as the curve fit, using equation 3.4. Fine particle absorption was estimated as $10 * \text{LAC}$ and was added to the reported nephelometer-derived b_{scat} values. Because IMPROVE particle samples are collected over 24-hr time periods, the continuous nephelometer data are average up to 24 hr. As such, the variability in the scatterplots of V_r versus PM does not reflect the variability between these two variables associated with diurnal variability of the $f(\text{RH})$ factor.

The nephelometer utilized in the IMPROVE network is of an open-air design that measures a portion of coarse mass scattering as well as fine particle scattering; however, it has been calculated that coarse particle scattering is underestimated by about a factor of 2. An estimation of coarse particle scattering was subtracted from the nephelometer-measured scattering.

Figure 3.1 shows a number of $V_r = f(\text{PM})$ relationships, both as log-log plots and as more conventional V_r versus m plots. If $V_r = \frac{3.912}{\alpha} / \text{PM}$, then a log-log plot will be linear. On the

other hand, if mass loadings are low enough, the effect of Rayleigh scattering, b_{sg} , must be considered, and the relationship between V_r and m becomes nonlinear.

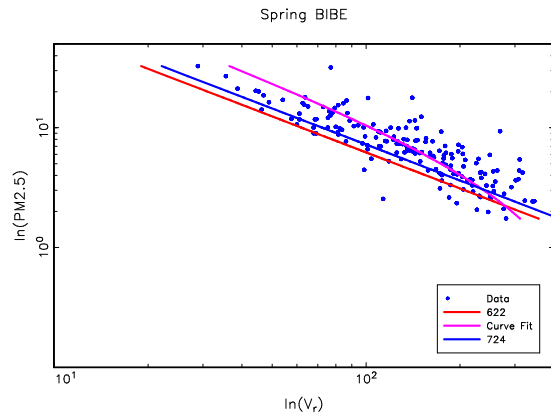
Shown on each graph is the relationship between V_r and PM, assuming $3.912/\alpha$ is equal to 724 and 622, the measured b_{scat} and PM data, and the curve fit for that dataset. Because $3.912/\alpha = 622$ or 724, which is only about 14% different, the two V_r versus mass curves using these two proportionality constants are similar. The analysis was done by season and for all seasons combined.

These inherent nonlinear biases are highlighted in the graphs for Big Bend (BIBE), Hance (HANC-Grand Canyon), and Phoenix (PHOE). The nonlinearity between $\log(V_r)$ and $\log(m)$ is highlighted in the HANC (Grand Canyon) data set, where the V_r is rarely lower than about 100 km.

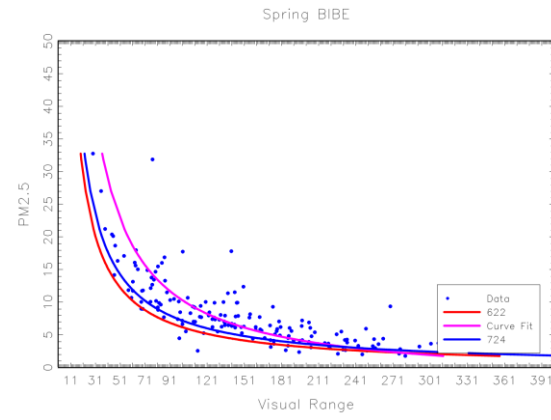
For the Great Smoky Mountains (GRSM) dataset, the $3.912/\alpha = 622$, and the curve fit V_r versus PM relationships are almost identical, as they are for most of the eastern United States. The implied α in the eastern United States is about $6 \text{ m}^2/\text{gm}$, which is a result of a significant amount of water on sulfate and nitrate aerosols, but it does not imply an enhanced mass extinction

efficiency of a smoke aerosol. The enhanced α is a result of measured scattering of a wet aerosol divided by a dry mass, yielding an inflated extinction to mass ratio.

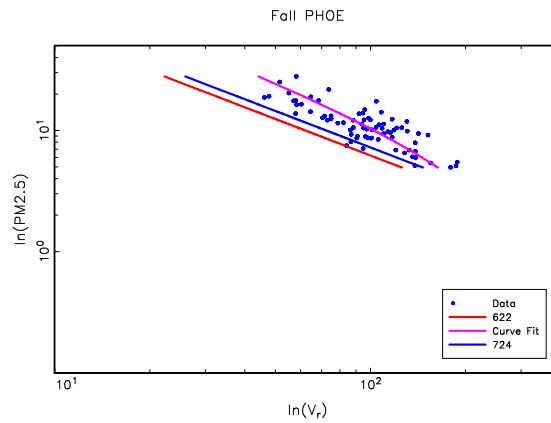
GAUSS Tue Jun 11 16:11:38 2013



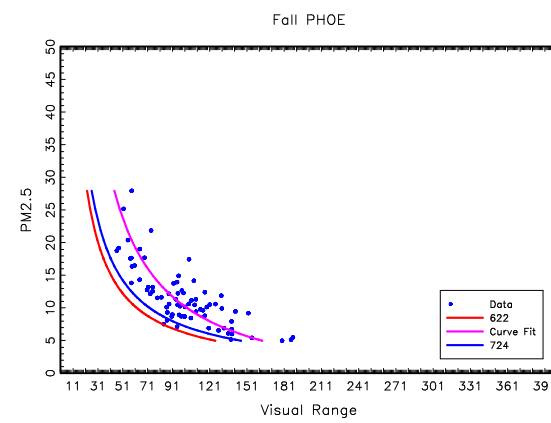
GAUSS Tue Jun 11 16:11:38 2013



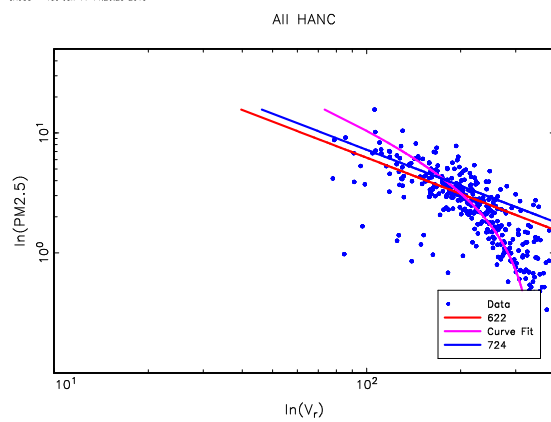
GAUSS Tue Jun 11 16:42:25 2013



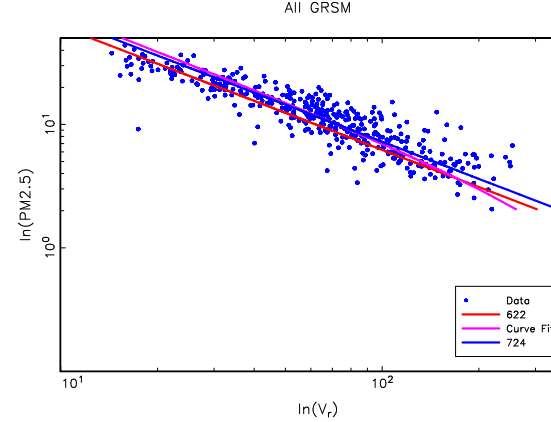
GAUSS Tue Jun 11 16:42:25 2013



GAUSS Tue Jun 11 14:26:23 2013



GAUSS Tue Jun 11 14:26:23 2013



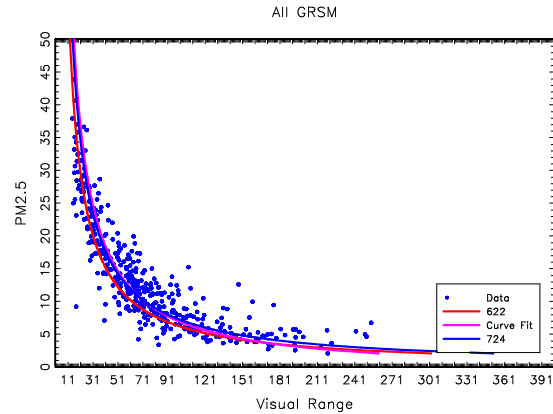


Figure 3.1: Plots of $PM_{2.5}$ vs. visual range as derived from open air nephelometer measurements of b_{scat} . Also shown in each of the graphs is a curve fit of the measured data and visual range vs. $PM_{2.5}$, assuming $3.912/\alpha = 724$ and 622 .

Table 3.2 contains the estimated average extinction efficiencies α and the standard deviation of derived mass extinction efficiencies σ as a function of season and for the entire year for each site listed in Table 3.1. α was derived from the curve fit between V_r and PM using equation 3.4, while σ corresponds to the standard deviation of calculated mass extinction efficiencies. The average mass extinction efficiency across all sites for all years is $4.16 \text{ m}^2/\text{gm}$, which corresponds to a $CNST = 940$. Figure 3.2 is a spatial plot of the average annual mass extinction efficiencies in Table 3.2, explicitly showing how α varies across the country.

Table 3.2: Average estimated extinction efficiencies, α , and standard deviation, σ , of α for each season and for the year as a function of monitoring site. Units of α are m^2/gm .

Name	Winter (α)	Winter (σ)	Spring (α)	Spring (σ)	Summer (α)	Summer (σ)	Fall (α)	Fall (σ)	All (α)	All (σ)
MORA	5.75	2.00	5.15	1.14	4.86	1.20	5.15	2.92	4.90	1.86
THSI	5.93	1.93	3.28	2.41	4.78	0.97	5.00	0.89	4.19	1.47
SNPA	6.73	2.47	3.46	1.71	4.32	0.80	6.25	1.33	4.54	1.54
CORI	8.25	2.82	4.19	1.56	3.32	1.03	3.86	1.55	3.89	1.76
JARB	2.66	4.05	3.04	2.34	3.54	1.20	2.63	2.13	2.92	2.12
PHOE	4.70	0.87	3.42	1.02	2.12	0.50	3.20	0.63	3.66	0.86
HANC	4.16	2.45	2.51	1.62	2.95	0.89	3.55	1.50	3.04	1.66
SYCA	1.53	1.84	1.37	1.22	1.11	0.79	1.65	0.94	1.55	1.14
IKBA	4.05	1.14	1.93	1.16	1.69	1.25	3.28	0.86	2.11	1.22
LOPE	6.75	2.75	2.58	1.95	3.27	0.80	3.92	1.38	3.55	1.80
GICL	3.48	1.50	2.98	1.02	4.85	1.20	4.86	1.13	3.65	1.29
BIBE	4.11	1.63	3.42	1.12	3.20	0.86	4.43	1.26	3.46	1.26
UPBU	6.45	1.52	4.65	1.93	5.79	1.75	4.63	1.68	5.00	1.86
BOWA	7.51	3.92	4.97	2.40	5.79	0.85	4.12	1.70	5.24	2.96
MACA	7.00	2.17	4.89	1.97	5.70	1.04	5.12	1.76	5.18	2.07

Name	Winter (α)	Winter (σ)	Spring (α)	Spring (σ)	Summer (α)	Summer (σ)	Fall (α)	Fall (σ)	All (α)	All (σ)
SENY	7.80	2.70	5.71	2.73	5.16	0.88	7.40	2.15	5.61	2.64
GRSM	4.81	1.93	4.18	1.40	6.33	1.31	4.97	1.39	4.98	1.57
OKEF	6.95	1.30	6.59	1.05	6.95	0.17	6.59	1.73	6.45	1.43
DOSO	5.18	5.39	5.82	1.98	6.63	1.63	3.43	2.60	4.48	2.81
SHEN	5.41	1.66	3.69	1.32	6.16	1.66	4.69	2.14	4.49	1.67
ACAD	5.01	1.53	4.31	1.39	4.53	1.58	4.61	1.68	4.45	1.58

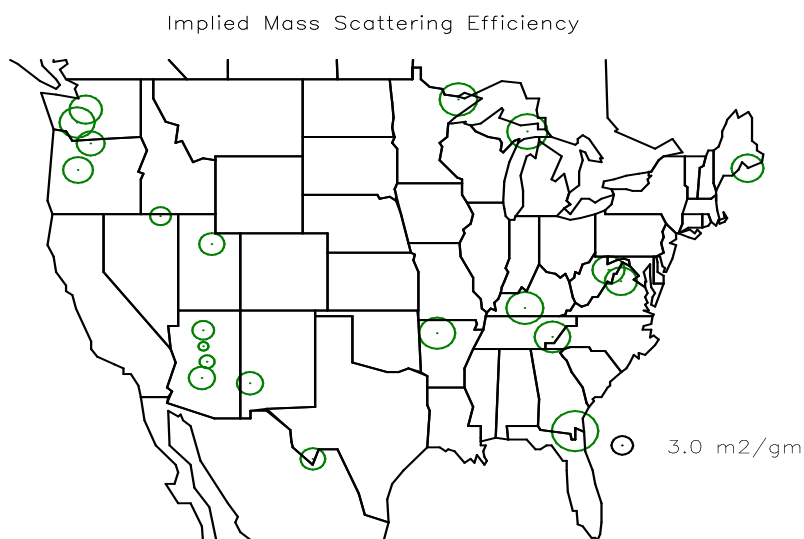


Figure 3.2: Spatial distribution of the average wet mass scattering efficiency α derived from the curve fit between measured b_{scat} and PM.

Figure 3.3 is a plot of α for each season and all data for each site sorted from west to east. Also plotted are these variables, assuming $3.912/\alpha = 724$ and 622 . The central-western United States has the lowest mass extinction efficiencies, with the interior eastern United States having the highest efficiencies. This is reflective of the higher RH and hygroscopic aerosol concentrations in the eastern United States. Again, because of higher RH levels, the northwestern U.S. sites have higher α values commensurate with the eastern United States. This inherent spatial bias is because in the West hygroscopic species concentrations tend to be low and the RH is also low, resulting in an average extinction to mass ratio that corresponds to a dry aerosol. As the humidity and hygroscopic species concentrations increase, the extinction to mass ratios increase dramatically.

Figure 3.3 shows that an α of 5.4 corresponding to $3.912/\alpha = 724$ is on the average about equal to mass scattering efficiencies in the East but about 35% too high in the West. $3.912/\alpha = 622$ is biased high even in the eastern United States and significantly high in the West. Also, winter α values tend to be higher than other seasons, although in general there is not a lot of seasonal dependence in the α values.

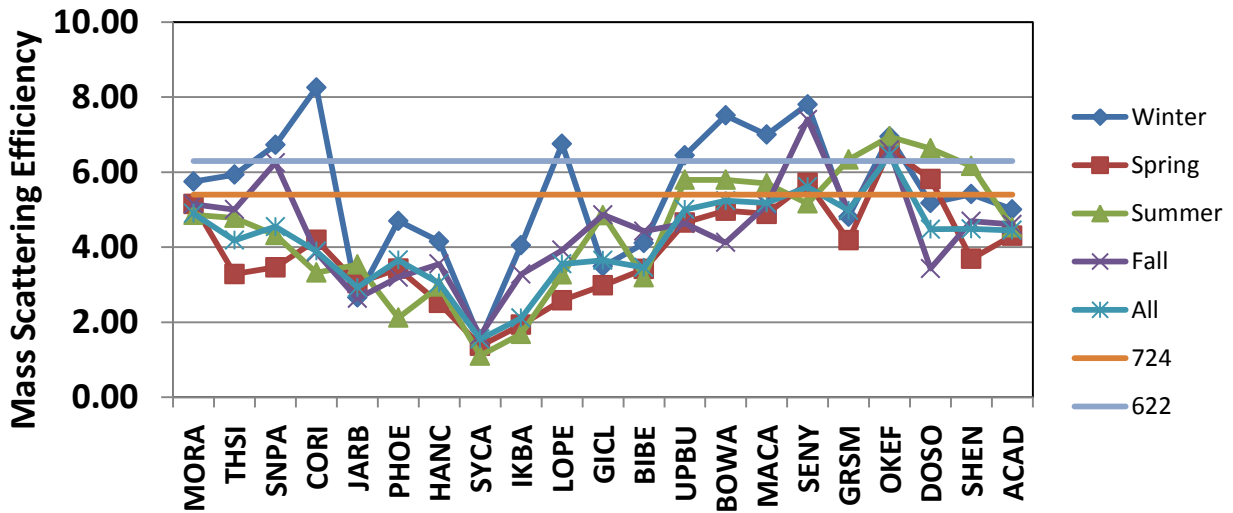


Figure 3.3: Mass scattering efficiencies for selected IMPROVE sites where integrating nephelometers are operated.

Figure 3.4 is a plot of the percent differences in the derived average α to the α implied by the $V_r\text{PM} = 622$ relationship, which is 6.3. A negative percent difference implies that a mass estimated from an observed V_r would be underestimated. In the East and Northwest, the difference is on the order of 20%, while in the central-western United States, the differences are close to 50%. As stated before, in many cases, especially in the western United States, $3.912/\alpha = 724$ also yields an underprediction of mass as a function of V_r .

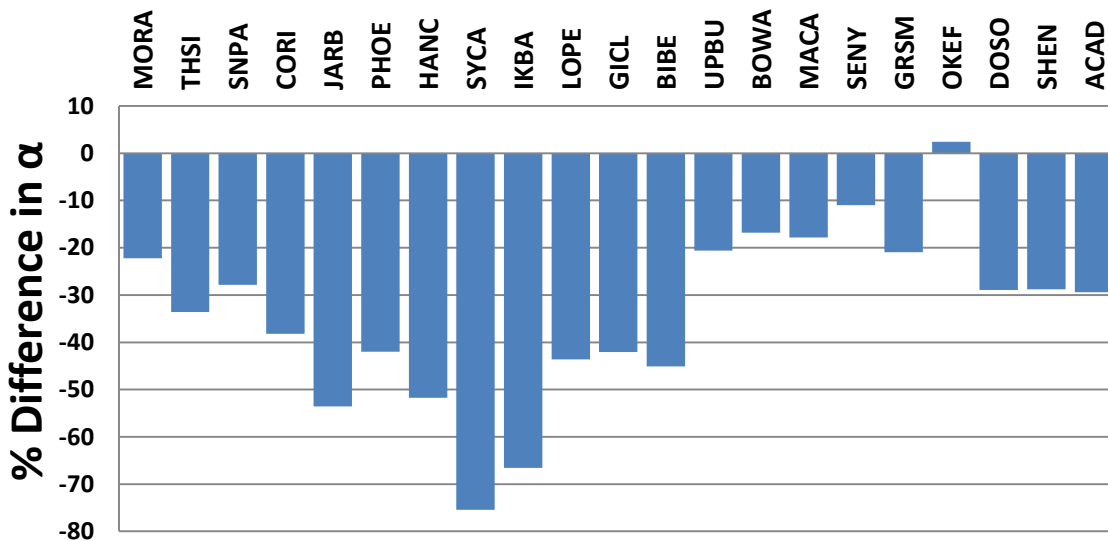


Figure 3.4: Plot of the percent differences between $\alpha = 6.3$ implied by the $V_r\text{PM} = 622$ relationship and the derived α obtained from nephelometer and fine mass measurements.

Table 3.3 shows the percents that one standard deviation σ of the derived α values are for each season and across all observed values. If the α values are normally distributed, $2*\sigma$ would

represent about 68% of all observed α values, with about 32% of the α values lying outside the range of α values represented by $\alpha - \sigma < \alpha < \alpha + \sigma$. Figure 3.5 is a plot of the average percent of the mean α represented by 2 standard deviations of the mean value (column 6).

Table 3.3: The average percent of the mean α represented by 2 standard deviations of the mean α value for each season and across all seasons.

Name	Winter(%)	Spring(%)	Summer(%)	Fall(%)	All(%)
MORA	69.62	44.42	49.41	113.66	76.02
THSI	65.15	146.64	40.68	35.66	70.31
SNPA	73.47	98.86	37.01	42.51	67.83
CORI	68.22	74.46	62.22	80.42	90.39
JARB	305.09	153.78	67.75	161.92	145.28
PHOE	36.98	59.42	46.91	39.46	46.86
HANC	117.72	128.91	60.45	84.69	109.04
SYCA	239.71	179.03	142.61	114.50	147.35
IKBA	56.36	119.86	148.53	52.15	115.34
LOPE	81.61	151.36	48.78	70.30	101.19
GICL	86.17	68.57	49.54	46.50	70.58
BIBE	79.40	65.42	54.00	57.12	72.72
UPBU	47.23	82.78	60.33	72.53	74.39
BOWA	104.51	96.42	29.40	82.53	113.04
MACA	61.92	80.85	36.52	68.86	79.85
SENY	69.15	95.46	34.00	58.12	94.25
GRSM	80.32	66.83	41.42	55.93	62.83
OKEF	37.51	31.99	4.87	52.61	44.38
DOSO	208.39	68.05	49.09	151.42	125.75
SHEN	61.50	71.39	53.91	91.04	74.40
ACAD	61.06	64.35	69.71	73.09	71.11

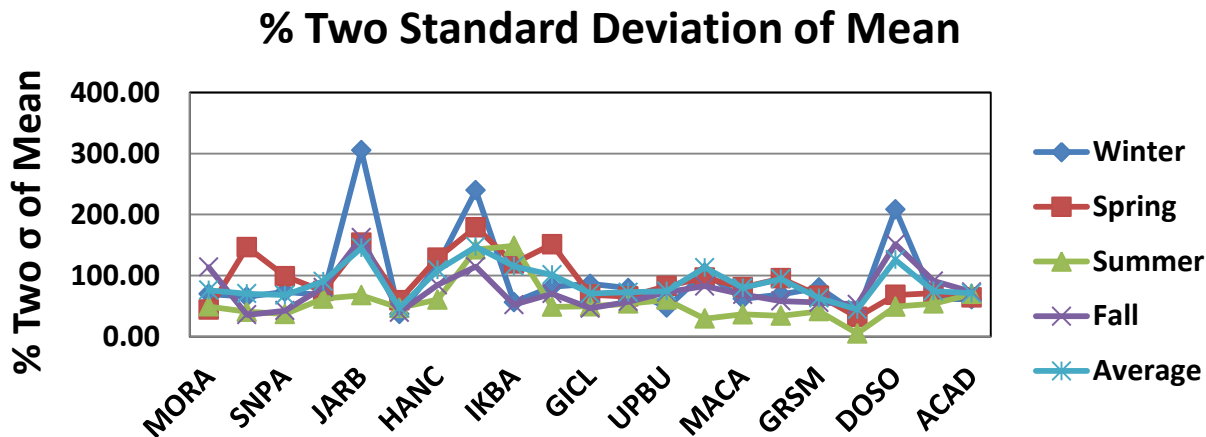


Figure 3.5: Plot of the average percent of the mean α represented by 2 standard deviations of the mean α value for each season and across all seasons.

Figure 3.5 can be generally interpreted to represent the uncertainty in estimated mass extinction efficiencies. It represents the variability in mass extinction efficiency due to variability in particle size distribution, aerosol density, and to some degree aerosol hygroscopicity. The variability in hygroscopicity resulting from diurnal variability in RH and thus $f(\text{RH})$ is not reflected in the above analysis because only 24 average mass and extinction values were used. It will be shown that the additional variability associated with diurnal-varying RH adds another factor of 2–3 (100–200%) variability in α . This estimated uncertainty is surprisingly constant, on a percent basis, at about 75%. The summer uncertainty is a bit less than winter, spring, and fall uncertainties.

4. MEASURED AND DERIVED MASS SCATTERING AND EXTINCTION EFFICIENCIES

4.1 Mass Scattering, Absorption, and Extinction Efficiency

In most instances, particle scattering and absorption are primarily responsible for visibility reduction. As discussed above, particle scattering and absorption properties can, with a number of limiting assumptions, be calculated using Mie theory. However, before such calculations are carried out, appropriate boundary conditions must be specified. Typically, particle models assume either external or internal mixtures of molecules and/or particles. Externally mixed particles exist in the atmosphere as pure chemical species that are mixed without interaction, while internally mixed particles are single particles made up of two or more species.

Aerosol models typically assume that aerosol species are mixed externally; the simplest example is a particle composed of a single chemical species such as ammonium sulfate, and for this case the extinction efficiency is referred to as “mass extinction efficiency”. However, realistically, particles in the atmosphere comprise a variety of inorganic and organic species. These types of particles are referred to as internal mixtures, and their extinction efficiencies are termed “specific mass extinction efficiencies”. Internally mixed particles can also be externally mixed from other

particle populations; the most obvious case would be internally mixed fine-mode aerosols externally mixed from coarse-mode aerosols.

In general, if externally mixed,

$$b_{ext,p} = \alpha_{mix}TM = \sum_i \alpha_i m_i \quad 4.1$$

where α_{mix} is the overall mass extinction efficiency and TM is total mass concentration including coarse mass, α_i is the mass scattering or absorption efficiency of each individual species, and m_i is the mass of each aerosol species. In the previous equations, PM was used to represent mass, while in equation 4.1, TM is used to explicitly include coarse mass CM. Also, equation 4.1 as written implies that α_{mix} includes scattering due to absorbed water.

As stated previously, equation 4.1, derived for externally mixed aerosols, also holds for an internally mixed aerosol in which the chemical species are mixed in fixed proportions to each other, the index of refraction is not a function of composition or size, and the aerosol density is independent of volume. When computing total extinction using Mie theory, the microscopic structure of the aerosol (that is, the extent of internal or external mixing) is found to be relatively unimportant, so that the assumption of internally versus externally mixed particles does not have much impact on the predicted results (Sloane, 1983, 1984, 1986; White, 1986; Malm and Kreidenweis, 1996). The mass extinction (or scattering) efficiency is a stronger function of density and size than optical properties such as refractive index.

Therefore

$$\alpha_{mix} = \sum_i \frac{m_i}{TM} \alpha_i \quad 4.2$$

Mass scattering and extinction efficiencies have been derived using a number of different approaches. They include a theoretical approach, direct measurement, a statistical approach, usually in the form of a regression model (MLR), and a combination of approaches referred to here as “partial”. For additional information on these approaches, the interested reader is directed to a review article by Hand and Malm (2007).

Average values of scattering to mass ratios α_i associated with each species are presented in Table 4.1. Estimates in Table 4.1 correspond to dry, fully neutralized fine-mode ammonium sulfate, dry, fine-mode ammonium nitrate, particulate organic material (POM) with a multiplier of 1.8, and dry sea salt. These estimates are averages (and one standard deviation) of many individual values that have been reported and derived by different methods. The number of studies is included in parentheses in Table 4.1. Values included in the average for each method have met the following criteria: the mass scattering efficiency for a given species is normalized (either by the cited authors or by us) to the above stated conditions; a given study had to clearly state the assumptions and methodology used to compute a reported efficiency; POM and dust are assumed to be nonhygroscopic; and estimates from the partial scattering method are computed assuming constant particle size.

Table 4.1: Average and one standard deviation of mass scattering efficiencies. “Fine”, “Coarse”, and “Total” correspond to the size range of the aerosol. “Mixed” refers to a mixed-composition aerosol. Sulfate efficiencies correspond to dry ammonium sulfate, nitrate entries correspond to dry ammonium nitrate, POM efficiencies have been normalized to an R_{oc} value of 1.8, and sea salt efficiencies have been adjusted to a dry state. The final column gives the overall average for all methods for the mixed-composition aerosols, and the average of three methods (theoretical, MLR, and partial) for the remaining species. The number of observations is given in parentheses. Estimates are for visible wavelengths (near 550 nm).

Species/ Mode	Theoretical ($\text{m}^2 \text{g}^{-1}$)	Measurement ($\text{m}^2 \text{g}^{-1}$)	MLR ($\text{m}^2 \text{g}^{-1}$)	Partial ($\text{m}^2 \text{g}^{-1}$)	All Methods ($\text{m}^2 \text{g}^{-1}$)
Fine mixed	4.3±0.7 (26)	3.4±1.2 (54)	3.1±1.4 (16)	3.4±1.6 (2)	3.6±1.2 (98)
Coarse mixed	1.6±1.0 (21)	0.40±0.15 (4)	0.7 ± 0.4 (26)		1.0±0.9 (51)
Total mixed	2.2±1.0 (9)	1.7±1.1 (11)			1.9±1.1 (20)
Fine sulfate	2.1±0.7 (34)		2.8±0.5 (53)	2.2±0.7 (6)	2.5±0.6 (93)
Fine nitrate			2.8±0.5 (42)	2.3±0.5 (6)	2.7±0.5 (48)
Fine POM	5.6±1.5 (19)		3.1±0.8 (39)		3.9±1.5 (58)
Coarse POM	2.6±1.1 (19)				2.6±1.1 (19)
Total POM	3.8±0.5 (7)		1.4 (1)		3.5±1.0 (8)
Fine dust	3.4±0.5 (19)		2.6±0.4 (4)		3.3±0.6 (23)
Coarse dust	0.7±0.2 (20)		0.40±0.08 (2)		0.7±0.2 (22)
Total dust	1.2±0.3 (9)	0.9±0.8 (5)	0.7±0.2 (3)		1.1±0.4 (12)
Fine sea salt	4.5±0.7 (22)		3.7±1.7 (3)		4.5±0.9 (25)
Coarse sea salt	1.0±0.2 (19)		0.72±0.02 (2)		1.0±0.2 (21)
Total sea salt	2.2±0.5 (8)		1.8±0.3 (2)		2.1±0.5 (10)

In an analysis of the IMPROVE data, Malm and Hand (2007) found that inorganic and organic species have a mass-dependent mass scattering efficiency, and this dependence was integrated into a new IMPROVE algorithm in which the POM mass scattering efficiency was scaled between 2.8 and 6.1 m^2/gm for POM mass concentrations between 0.0 and 20.0 $\mu\text{g}/\text{m}^3$ (Pitchford et al., 2007). It was hypothesized that the higher particle mass concentrations were associated with an aged aerosol that was more mono-disperse in a size range that is conducive to efficient light scattering. The POM mass concentrations associated with wildfire and prescribed fire, although high in mass loading, are not necessarily aged. In fact, the highest mass loadings are usually associated with a direct impact of a smoke plume. Therefore it should not be assumed

and would likely be wrong to link the higher mass scattering efficiencies used in the new IMPROVE algorithm to those found in an aerosol containing high levels of smoke particulates. Furthermore, the new IMPROVE equation is essentially an empirical fit between measured atmospheric scattering and particle concentrations. The new equation is actually less precise but more accurate on the average.

4.2 Mass Scattering and Extinction Efficiencies of Smoke

The extinction efficiencies and $f(\text{RH})$ for smoke depend on the chemical composition and size distribution of the smoke particulate matter. These properties vary widely depending on the fuels burned and a variety of contrasting conditions, including smoldering versus flaming fires, wet versus dry fuel, crown versus understory fires, and fresh versus aged smoke, as well as differing meteorological and climate conditions. Therefore the smoke extinction to mass ratio will vary over the evolution of a single fire as well as the time of day. In addition, systematic spatial and seasonal differences are expected.

Given the variety of smoke's chemical physical and optical properties, there has not been an extensive set of field and lab studies to fully understand this variability. Reid et al. (2005a,b) reviewed and summarized the available studies through the early 2000s. This included field studies conducted around the world, controlled laboratory studies as well as detailed analyses of some routine monitoring data when known to be impacted by smoke.

Since the Reid et al. (2005a,b) reviews, there have been a number of field and lab studies to characterize biomass burning emissions and smoke, but only a few examined its optical properties. The most extensive were the Fire Lab at Missoula Experiment (FLAME) laboratory studies (McMeeking et al., 2009). FLAME primarily examined the physical, chemical, and optical properties of fuels commonly burned in mid-latitude forests, including the western and southeastern United States. This included fresh emissions, i.e., minutes post-combustion, where the smoke was funneled through a stack to the instruments (Chen et al., 2007); and young emissions where the fuels were burned in a closed chamber and allowed to mix and age for 1–3 hr (Levin et al., 2010; Mack et al., 2010). In another laboratory study, the optical properties of fresh smoke from burning peat were examined (Chand et al., 2005). In the summer of 2003, the Yosemite Aerosol Characterization Study (YACS) was conducted to assess ambient aerosol in Yosemite National Park (Malm et al., 2005b). During this study, the monitoring site was heavily impacted by aged smoke from a large wildfire in Oregon as well as young smoke from more nearby prescribed and wildfires. With the increased awareness of the importance of absorption from short-lived climate forcers on the global radiation balance, there have been several detailed studies examining the absorption properties of brown and black carbon from biomass burning and other sources (e.g., Schwarz et al., 2008; Lack et al., 2013)

Results from these studies are summarized in Tables 4.2 to 4.6. Following is a discussion of these study results and the processes driving their variability.

4.2.1 Dry Mass Scattering Efficiency α_s

Dry mass scattering efficiency α_s is often estimated as the ratio of measured light scattering by a nephelometer divided by the measured mass concentration collected on a filter. These measurements are subject to systematic errors that can bias the results. Nephelometers have a forward-scattering truncation issue, thus underestimating forward scattering, which is most severe for large particles, while mass measurements of a smoke aerosol are subject to negative artifacts. For example, TEOM instruments are heated to some degree, which can cause a loss of volatile compounds, such as some organics. These biases in the “measured” α_s need to be taken into consideration when comparing results across studies. An alternative method is to measure the particle size distribution and then use assumed particle densities and refractive indices to derive α_s . These derived α_s do not suffer from the same biases as the other bulk measurements but can have large uncertainties in the assumed physical parameters.

As shown in Table 4.2, Chen et al. (2007) reported α_s for fresh emissions from stack burns. These types of burns allow the isolation of fuels and combustion processes. There is a broad range of α_s varying from 0.4 to 3.6 m²/gm. The α_s during the smoldering phase is generally a little larger than during the flaming phase. This is evident in the peat fires studied by Chand et al. (2005) (Table 4.2) in which the smoldering smoke had $\alpha_s \sim 7$ m²/gm. Note that these are high α_s and are likely overestimated due to Chand et al. (2005) using heated TEOM mass measurements in their lab experiments. It is thought that increased α_s during smoldering is due to larger particles that scatter light more efficiently and less-absorbing black carbon than those emitted during flaming (Reid et al., 2005a; Chen et al., 2006; Chand et al., 2005).

Table 4.2: Optical properties of smoke from the FLAME and YACS Studies. Phase: F = Flaming, M = Mixed, S = Smoldering. Data are from FLAME 2.

Fuel	Fuel Type	Phase	α_s Measured	α_s Derived	α_a Measured	α_e	Scattering Albedo	EC/TC (TOR)	Salt Mass Fraction (%)	f(90)
Levin et al. (2010) and Mack et al. (2010); Young smoke from laboratory chamber burns										
Longleaf pine needles and wire grass	Trees and grass	M	3.0	4.0	0.21	3.2	0.93±0.01	0.07	9	
Black needlerush	Grass	M	3.4	4.2	0.31	3.7	0.92±0.01	0.12	23	
Douglas fir needles and branches, dry	Tree	M	4.0	4.2	0.18	4.2	0.96±0.00	0.07	2	
Douglas fir needles and branches, dry	Tree	M	5.7	4.6	0.17	5.9	0.98±0.00	0.06	3	
Alaskan duff	Duff	M	4.2	4.2	0.04	4.2	0.99±0.00	0.02	1	
Wiregrass	Grass	M	2.9	3.5	0.51	3.4	0.85±0.01	0.17	7	
Black needlerush	Grass	M	4.4	4.7	0.49	4.9	0.90±0.01	0.11	21	
Sagebrush	Desert shrub	M	2.2	2.9	0.94	3.2	0.70±0.02	0.27	24	
Longleaf pine needles	Tree	M	3.9	4.8	0.19	4.1	0.95±0.01	0.04	3	

Fuel	Fuel Type	Phase	α_s Measured	α_s Derived	α_a Measured	α_e	Scattering Albedo	EC/TC (TOR)	Salt Mass Fraction (%)	f(90)
Oak and hickory	Trees	M					0.85±0.01	0.08	11	
Douglas fir needles and branches, fresh	Tree	M					0.53±0.03			
Florida palmetto leaves	S.E U.S. shrub	M					0.43±0.03	0.70	51	
Mississippi palmetto leaves	S.E U.S. shrub	M					0.62±0.03	0.39	42	
Alaskan duff	Duff	M					0.97±0.00	0.03	2	
Rhododendron leaves	S.E U.S. shrub	M					0.81±0.02	0.12	8	
Black spruce needles and branches	Tree	M					0.67±0.03	0.34	3	
Chamise	Desert shrub	M					0.43±0.03	0.50	21	
Gallberry	S.E U.S. shrub	M					0.45±0.03	0.48	7	
White spruce	Tree	M					0.91±0.01	0.11	10%	
Chen et al. (2007), Fresh smoke from laboratory stack burns										
Ponderosa pine wood	Tree	F	1.8±0.4		6.3±1.4	9.2±1.9	0.19±0.06			
Ponderosa pine needles	Tree	F	1.8±0.3		4.3±0.7	7.2±1.2	0.24±0.06			
White pine needles	Tree	F	3.0±0.4		2.0±0.3	6.2±0.6	0.49±0.08			
Sagebrush	Desert shrub	F	1.4±0.2		4.0±0.8	5.8±1.0	0.23±0.05			
Excelsior	Tree	F	2.3±0.4		4.3±0.6	6.8±1.2	0.34±0.08			
Dambo grass	Grass	F	3.1±1.5		1.5±0.8	5.8±4.2	0.55±0.48			
Montana grass	Grass	F	2.9±1.1		0.2±0.1	3.4±2.1	0.84±0.59			
Ponderosa pine wood	Tree	S	0.4±0.7		0.4±0.6	1.0±1.6	0.46±1.08			
Ponderosa pine needles	Tree	S	1.2±0.5		1.0±1.0	2.9±2.0	0.41±0.33			
White pine needles	Tree	S	3.6±1.1		0.0±0.0	4.9±1.9	0.74±0.36			
Sagebrush	Desert shrub	S	2.1±0.6		1.2±0.4	3.4±1.9	0.61±0.38			
Excelsior	Tree	S	2.8±1.7		0.5±0.3	3.9±3.4	0.72±0.76			

Fuel	Fuel Type	Phase	α_s Measured	α_s Derived	α_a Measured	α_e	Scattering Albedo	EC/TC (TOR)	Salt Mass Fraction (%)	f(90)
Dambo grass	Grass	S	1.1±2.3		0.1±0.2	1.5±3.7	0.73±2.36			
Montana grass	Grass	S	3.2±1.7		0.0±0.0	5.0±3.9	0.64±0.61			
Ponderosa pine wood	Tree	M	1.7±0.4		6.0±1.6	8.8±2.3	0.19±0.07	0.84±0.09	4.97±0.58	
Ponderosa pine needles	Tree	M	1.7±0.3		3.9±0.7	6.7±1.2	0.26±0.07	0.65±0.07	18.75±3.39	
White pine needles	Tree	M	3.4±0.7		0.8±0.2	5.3±1.2	0.63±0.19	0.25±0.06	3.17±0.31	
Sagebrush	Desert shrub	M	1.7±0.3		2.7±0.5	4.7±1.0	0.35±0.10	0.56±0.07	45.43±0.78	
Excelsior	Tree	M	2.4±0.4		3.7±0.7	6.4±1.6	0.38±0.12	0.63±0.09	10.23±0.56	
Dambo grass	Grass	M	3.0±1.5		1.5±0.8	5.4±4.0	0.55±0.49	0.36±0.14	8.37±3.85	
Montana grass	Grass	M	3.0±30.7		0.1±0.9	4.2±43.4	0.71±10.22	0.07±0.10	1.32±0.21	
Chand et al. (2005), Fresh smoke in laboratory stack burns										
German peat	Peat	S	7.4±0.7		0.04	7.8±0.7	0.99			1.05
Indonesian peat	Peat	S	8.1±1.7		0.05	8.6±1.7	0.99			1.02
Indonesian peat	Peat	S	7.6±0.9		0.04	8.0±0.9	0.99			1.00
Indonesian peat	Peat	S								1.05
Indonesian peat	Peat	S	6.4±0.7		0.06	7.0±0.7	0.99			1.02
Malm et al. (2005a), Young to aged smoke from prescribed and wildfires										
Northwestern United States fuels	Mixed	M		4.5 - 5.5						

The chamber burns shown in Table 4.2 (Levin et al., 2010) are for a more mixed set of fuels; have aged for 1–3 hr before sampling; and comprise both flaming and smoldering stages of combustion. The α_s are in general larger than those for either the fresh flaming or smoldering smoke, varying from 2.2 to 5.7 m²/gm, estimated from measured light scattering and PM_{2.5}, and 2.9–4.8 m²/gm, derived from size distribution measurements. The more efficient scattering is thought to be due to the particle growth from condensation of semivolatile VOCs (volatile organic carbon) and coagulation (Reid et al., 1998b). It is also noteworthy that the range in α_s

from the chamber experiments is smaller than from the stack experiments, a possible reflection of averaging across fuels, combustion phases, and narrowing of size distributions in more realistic fire scenarios.

This narrowing of range can also be seen in the field studies of young smoke in Table 4.3. As shown, the range of typical α_s for temperate and boreal forests of North America and grassland/savanna is 3.1–4.2 m²/gm. This is also in line with the chamber study results. Extreme values of α_s do occur in the field. During YACS, thick smoke from an Oregon fire was transported to Yosemite over a couple of days, during which it was processed by clouds. This created a narrow particle size distribution that efficiently scattered light with $\alpha_s \sim 5.5$ m²/gm (Table 4.2) (Malm et al., 2005a). During the same study, smoke from nearby wild and prescribed fires had $\alpha_s \sim 4.5$ m²/gm.

Different mass scattering efficiencies are expected for different seasons and regions of the United States. However, the available data are not sufficient to distinguish α_s between the different seasons and regions.

Table 4.3: Optical properties of smoke from Reid et al. (2005b). WL = White light. Phase: F = Flaming, M = Mixed, S = Smoldering.

Reference	Fuel/Location	# Fires	Wave length (nm)	Phase	MSE	MAE	Scattering Albedo
¹Fresh smoke							
Eccleson et al. (1974) in Reid et al. (2005b)	Temperate and boreal		540	F	4.2		
Hobbs et al. (1996)	Temperate and boreal	1	540	F			0.85±0.03
Hobbs et al. (1996)	Temperate and boreal	4	550	M	3.8±0.2	0.8±0.4	0.90±0.06
Hobbs et al. (1996)	Temperate and boreal	2	540	S			0.97±0.02
Martins et al. (1996a)	Temperate and boreal	4	WL	F		1.2±0.2	
Martins et al. (1996)	Temperate and boreal	4	WL	M		0.9±0.2	
Martins et al. (1996)	Temperate and boreal	1	WL	S		0.2±0.5	
Miller and O'Neill (1997)	Temperate and boreal	1	550	F			0.7
Miller and O'Neill (1997)	Temperate and boreal	1	672	F			0.6
Nance et al. (1993)	Temperate and boreal	3	540	F	4.1±0.1		
Radke et al. (1991)	Temperate and boreal	17	540	M	3.2	0.7±0.4	0.83±0.11
Radke et al. (1988)	Temperate and boreal	7	550	M	3.9	0.7±0.4	0.86±0.11
Tangren (1982)	Temperate and boreal		550	F	3.6		

Reference	Fuel/Location	# Fires	Wave length (nm)	Phase	MSE	MAE	Scattering Albedo
Martins et al. (1998a)	Tropical forest	7	WL	F		1.0±0.3	
Martins et al. (1998a)	Tropical forest	2	WL	S		0.6±0.2	
Reid and Hobbs (1998)	Tropical forest	6	450	F	4.5±0.4		
Reid and Hobbs (1998)	Tropical forest	6	550	F	2.8±0.5	1.0±0.2	0.74±0.06
Reid and Hobbs (1998)	Tropical forest	6	700	F	1.6±0.3		
Reid and Hobbs (1998)	Tropical forest	6	450	S	5.5±0.5		
Reid and Hobbs (1998)	Tropical forest	6	550	S	3.6±0.4	0.7±0.1	0.84±0.02
Reid and Hobbs (1998)	Tropical forest	6	700	S	1.9±0.3		
Yamasoe et al. (2000)	Tropical forest	19	WL	F		1.1±0.8	
Yamasoe et al. (2000)	Tropical forest	42	WL	S		0.6±0.2	
Martins et al. (1998a)	Scrub forest/cerrado	8		F		0.8±0.4	
Reid and Hobbs (1998)	Scrub forest/cerrado	6	450	F	5.1±0.5		
Reid and Hobbs (1998)	Scrub forest/cerrado	6	550	F	3.4±0.6	1.0±0.1	0.77±0.03
Reid and Hobbs (1998)	Scrub forest/cerrado	6	700	F	1.8±0.3		
Yamasoe et al. (2000)	Scrub forest/cerrado	55	WL	F		1.65±1	
Yamasoe et al. (2000)	Scrub forest/cerrado	33	WL	S		0.9±1	
Abel et al. (2003)	Grasslands/savanna	1	559	F			0.84
Evans et al. (1976) in Reid et al. (2005b)	Grasslands/savanna	1	550	F	3.1		
Reid and Hobbs (1998)	Grasslands/savanna	6	450	F	4.6±0.6		
Reid and Hobbs (1998)	Grasslands/savanna	6	550	F	3.5±0.5	1.1±0.2	0.76±0.08
Reid and Hobbs (1998)	Grasslands/savanna	6	700	F	1.9±0.3		
Vines (1971) in Reid et al. (2005b)	Grasslands/savanna	1	500	F	4		
2_{aged smoke}							
Abel et al. (2003)	Africa	1	550	M			0.9
Haywood et al. (2003)	Africa	many	567	M			0.91±0.04
Pilweskie et al. (2003)	Africa	2	450	M			0.85–0.88
Pilweskie et al.	Africa	2	550	M			0.84–0.88

Reference	Fuel/Location	# Fires	Wave length (nm)	Phase	MSE	MAE	Scattering Albedo
(2003)							
Pilweskie et al. (2003)	Africa	2	700	M			0.76-0.87
Formenti et al. (2003)	Africa	many	567	M	4.2–4.6		0.93±0.06
Magi et al. (2003)	Africa	many	567	M			0.83±0.02
Iziomon and Lohman (2003)	North America	many	567	M			0.91±0.04
Artaxo et al. (1994)	South America	150	WL	M		~1.1	
Artaxo et al. (1998)	South America	60	WL	M		0.5±0.2	
Echalar et al. (1998)	South America	126	WL	M		0.9–1.1	
Guyon et al. (2003)	South America	many		M			0.89±0.02
Hobbs et al. (1997)	South America	62	550	M	3.3±0.75		0.84±0.04
Martins et al. (1998a,b)	South America	20	WL	M		0.45±0.2	
Reid et al. (1998b)	South America	62	450	M	5.2±1.5		
Reid et al. (1998b)	South America	62	550	M	4.1±0.9	0.7±0.2	0.86±0.05
Reid et al. (1998b)	South America	62	700	M	2.4±0.6		
Formenti et al. (2002)	Canada to Europe	many	450	M			0.91
Formenti et al. (2002)	Canada to Europe	many	550	M			0.89
Formenti et al. (2002)	Canada to Europe	many	700	M			0.85
¹ . These data are from Reid et al. (2005b) Table 1 and are in situ optical properties from fresh smoke.							
² . These data are from Reid et al. (2005b) Table 2 and are in situ optical properties for regional aged smoke.							

4.2.2 Hygroscopicity

Soluble particulate matter absorbs water, increasing the particle size and the effective scattering efficiency. This hygroscopicity increases with RH, and is often accounted for by a hygroscopic growth function $f(\text{RH})$, a multiplication factor that describes the increase in scattering with increased RH. The $f(\text{RH})$, often taken at $\text{RH} = 80\%$ for reference ($f(80\%)$), is defined as the ratio of light scattering by the aerosol at an RH of 80% to the light scattering of the dry aerosol, usually at $\text{RH} < 35\%$.

The $f(\text{RH})$ is highly dependent on the composition of the particulate matter. Organic compounds are generally not very hygroscopic and have $f(80\%) < 1.1$ (Malm et al., 2005b), whereas salts, such as ammonium sulfate, are highly hygroscopic and can have $f(80\%) \sim 2.9$. Inorganic salts can be a significant fraction of the smoke. Consequently, RH can have a significant effect on the aerosol extinction efficiency and V_r and any resulting estimate of particulate matter and needs to be taken into account.

Few studies have looked at the hygroscopicity of smoke compared to its scattering and absorption properties. Field measurements have been summarized by Reid et al. (2005a,b) and Day et al. (2006) and are summarized for $f(\text{RH} \sim 80\%)$ in Table 1.9. As shown, with the exception of the Yosemite study (Malm et al., 2005a), field measurements were taken outside of North America, and there is a broad range of $f(80\%)$ varying from 1 to 2.1. Kotchenruther and Hobbs (1998) found that fresh smoke had an $f(80) = 1.1$, which increased with plume aging to 1.35. This can be explained by the formation of secondary salts in the aged plume. However, measured $f(\text{RH})$ in the African savanna (Magi et al., 2003) decreased as the plume aged (Table 4.4), defying a simple explanation of the evolution of smoke plume hygroscopicity. The one North American study in Yosemite found a lower $f(80)$ of 1.1–1.2. In this study, both fresh and aged smoke was sampled.

Laboratory studies have been conducted to better understand the hygroscopicity of North American fuels (Day et al., 2006; Hand et al., 2010; Levin et al., 2010), and the results are summarized in Tables 4.4 and 4.5. As shown in Table 4.4, a series of stack burns of fresh smoke found $f(80)$ varied from 1.1 to 1.76, with an average of 1.29 (Day et al., 2006).

Table 4.4: Published values of biomass burning humidification factors ($f(\text{RH})$) using nephelometry (Day et al., 2006).

f(RH) Range	Average	RH(%) Humid/Dry	Fire Type	Location/Fuel	Instrument Platform	λ, nm	Reference
1.01–1.51	Fresh: ~1.1 Aged: ~1.35	80/30	Plume and regional haze	Brazil/Cerrado and pasture/forest	Aircraft	550	Kotchenruther and Hobbs (1998)
1.1–1.7	Fresh: ~1.37	80/20	Flame and smoldering	North Australia/wooded savannah	Aircraft	530	Gras et al. (1999)
1.2–2.1	Aged: ~1.65	80/20	Smoldering, haze	Indonesia/rain forest, peat deposit	Aircraft	530	Gras et al. (1999)
1.44 ± 0.02	Aged: ~1.44	80/30	Ambient aged heavy smoke	African savannah	Aircraft	550	Magi and Hobbs (2003)
1.66 ± 0.08	Fresh: ~1.66	80/30	Plumes within 10 min of emission	African savannah	Aircraft	550	Magi and Hobbs (2003)
1.1–1.2		80–85/10–15	Aged regional smoke/haze	Yosemite National Park, California (Oregon fires)	Ground-based	530	Malm et al. (2005a)
1.60 ± 0.20	Aged: ~1.6	85/40	Aged regional smoke	Gosan, Korea (Russian and North Korean fires)	Ground-based	550	Kim et al. (2006)
1.01 ± 0.05–1.76 ± 0.05	1.29	75–80/10	Fresh minutes-old	laboratory/ midlatitude forest fuels	Laboratory	530	Day et al., (2006)

Table 4.5: Measured smoke characteristics for biomass fuels burned from Hand et al. (2007). All burns were conducted in a chamber, were integrated over flaming and smoldering stages, and aged an hour or more. Measured $f(\text{RH})$ is reported for $\text{RH} = 80\text{--}85\%$, with dry $\text{RH} = 20\text{--}25\%$, wavelength of 530 nm, and experimental uncertainty of ± 0.08 .

Fuel	Fuel Type	Inorganic Salts Mass Fraction (%)	Carbon Mass Fraction (%)	$f(\text{RH})$ (80–85%)
Ponderosa pine	Forest/pine	2	98	1
Lodgepole pine	Forest/pine	2	98	1.02
Southern pine	Forest/pine	2	98	1.07
Chamise	Shrub	30	70	1.58
Chamise (repeat)	Shrub	32	68	1.45
Juniper	Shrub	13	87	1.14
Sage/rabbit	Shrub	42	58	1.81
Manzanita	Shrub	22	78	1.34
Ceanothus	Shrub	16	84	1.15
Puerto Rico fern	SE U.S./Tropical	10	90	1.07
Puerto Rico wood	SE U.S./Tropical	7	93	1.06
Wax myrtle	SE U.S./Tropical	26	74	1.34
Ponderosa pine duff	Other	3	97	1.04
Alaskan duff	Other	2	98	1.07
Lignin	Other	2	98	0.99

Table 4.5 presents the $f(80\%)$ and fraction of the particulate mass composed of inorganic salts for a series of chamber burns that were aged for an hour or more (Hand et al., 2007). The $f(80\%)$ varies from 1 to 1.81 and is highly correlated with the inorganic salt fraction. Hand et al. (2010) showed that almost all of the hygroscopicity could be explained by these inorganic salts, suggesting that the carbonaceous aerosols, even though water soluble, do not absorb significant amounts of water. In addition, it is evident that shrubs are significantly more hygroscopic than trees and duff, with $f(80\%)$ of 1.41 and 1.04, respectively. This appears to be independent of the United States region with $f(80\%)$ for southern pine from the southeastern United States of 1.07 and 1–1.02 for western ponderosa and lodgepole pine. A similar pattern can also be seen in the chamber and stack burns in Table 4.2, with smoke from trees having a lower inorganic salt content than shrubs. Grasses on the other hand have a broader range of inorganics, from 1% for Montana grass to 23% for black needlerush. Any wild and prescribed fire will contain a mixture of grasses, duff, trees, and shrubs, which should reduce the variability seen in the laboratory studies.

4.2.3 Absorption Efficiency α_a

Similar to α_s , absorption efficiency can be estimated from the ratio of measured light absorption divided by the measured mass concentration collected on a filter. Note that the influence of particulate hygroscopic growth on α_a is generally small and neglected. The measurement of

absorption is one of the more difficult radiative parameter to measure (e.g., Campbell et al., 1996; Heintzenberg et al., 1997; Bond et al., 1999; Russell et al., 2002). The principal methodologies commonly used are to measure the attenuation of a light beam through an ambient sample (e.g., extinction cell) or a filter sample (e.g., aethalometer) or the photoacoustic method that measures the acoustics from the heating and cooling effects on an ambient sample from cycling a light beam on and off through the sample.

Absorption can also be modeled by measuring elemental or black carbon and assuming that all absorption is due to elemental carbon (EC). Absorption is then the mass absorbing efficiency of EC multiplied by the EC mass. This method has a number of shortcomings, including the fact that many EC measurements are operationally defined and have large errors, other compounds including iron oxides and some organic carbon compounds absorb light, and there are large errors in EC absorption efficiencies. Therefore the review concentrates on studies that estimate α_a from absorption and mass measurements. However, these absorption measurements are also subject to varying errors and biases that can lead to high uncertainties (see instrument section), and these errors are reflected in the varying α_a presented in Tables 4.2 and 4.3.

The highest α_a occurs during flaming combustion, which produces carbonaceous aerosol rich in EC. This is shown in the stack burns listed in Table 4.2. The majority of the PM was generated during the flaming stage, and EC accounted for about half of the measured total carbon (TC) over the entire burn. These high EC concentrations result in high α_a , e.g., $\alpha_a = 6.3 \text{ m}^2/\text{gm}$ for ponderosa pine wood (Table 4.2). Smoldering combustion produces a whiter, less EC-rich aerosol and correspondingly smaller α_a , with average values for the stack burns of about $0.5 \text{ m}^2/\text{gm}$.

The stack burns are ideal combustion scenarios, and in more real world conditions, the α_a is significantly smaller. As shown in Table 4.3, α_a measured in the field during primarily flaming conditions had α_a between 1 and $1.4 \text{ m}^2/\text{gm}$ for green light. Although α_a as high as $3 \text{ m}^2/\text{gm}$ was measured from smoke plume during intense fires (Martins et al., 1996; Reid and Hobbs, 1998). In more-typical mixed and smoldering combustion, α_a ranged between 0.6 to $1.0 \text{ m}^2/\text{g}$ and 0.2 to $0.7 \text{ m}^2/\text{g}$, respectively (Table 4.3) (Reid et al., 2005b).

The field experiments suggest that as the biomass burning plume ages, α_a significantly decreases, with aged smoke particles having reported values on the order of $0.5\text{--}1 \text{ m}^2/\text{gm}$. This can be seen in the scattering albedo in Table 4.3. The scattering albedo is the relative contribution of scattering to total extinction or $\alpha_s/(\alpha_s + \alpha_a)$. As the albedo increases, α_s increases relative to α_a . As shown in Table 4.3, the average scattering albedo for the fresh temperate and boreal burns is 0.82, while it is 0.89 for the aged North American, Canadian, and European burns. The decrease in α_a in an aged plume is thought to be partly due to increased concentrations of scattering particles through secondary particles formation, as well as the reduced absorbing efficiency of EC due to the collapse of any chain aggregates (Abel et al., 2003).

Reid et al. (2005b) notes that there is credible evidence (e.g., Reid et al., 1998a; Bond et al., 1999; Russell et al., 2002) that the absorption measurements used in the studies listed in Table 4.3 are generally overestimated absorption and thus α_a . The photoacoustic absorption method

used in the stack and chamber burn results presented in Table 4.2 should not suffer from this bias. As shown, the α_a from the chamber burns is generally lower than measured in the field, with $\alpha_a \sim 0.34 \pm 0.3 \text{ m}^2/\text{gm}$ (Table 4.2) (Levin et al., 2010).

4.2.4 *Brown Carbon Absorption*

Absorption is often assumed to be due to particulate black carbon that absorbs in all visible wave lengths. However, there is increasing evidence that organic carbon compounds such as organonitrates absorb light in the near ultraviolet- blue wave lengths (Claeys et al., 2012; Kitanovski et al., 2012; Lack et al., 2013). This absorption can be significant, with organic mass absorption efficiencies at $\sim 400 \text{ nm}$ in a smoke plume varying between $0.25 \text{ m}^2/\text{gm}$ and $2.9 \text{ m}^2/\text{gm}$ (Kirchstetter et al., 2004; Hoffer et al., 2006; Yang et al., 2009; Lack et al., 2013). This absorption is missed by measurement methods that focus on green wavelengths, i.e., $\lambda \sim 550 \text{ nm}$.

The absorption of brown carbon in the blue wavelengths is important from a radiation balance standpoint. However since brown carbon has little to no absorption in the green and red wavelengths, this should have only a small effect on human V_r and any optical measurement operating in the green wavelengths. Therefore, we ignore the impact of brown carbon absorption on the estimation of PM from V_r , but leave this as an area of concern for potential future research.

4.2.5 *Optical Parameters*

Scattering and absorbing efficiencies of smoke have broad ranges and are dependent on the fuels burned, e.g., grass versus trees, combustion phase, i.e., flaming versus smoldering, young versus aged smoke, and more. Reid et al. (2005b) took a careful look at the smoke optical properties from most of the field and laboratory studies conducted through the early 2000s and reviewed in this report. In addition, they looked at the optical properties derived from sun photometers in the AERONET monitoring network. They considered the results from all of these studies and tried to account for potential sampling biases to arrive at best estimates of the smoke optical properties for different fuels and fresh and aged smoke. These estimates are for general biomass burning conditions and thus represent mixed-phase combustion. The results are presented in Table 4.6 for temperate/boreal grass/savanna and tropical fuels. The smoke optical parameters likely vary within these biomes, but the data are not available for these finer-scale distinctions. Table 4.6 also provides the recommended optical properties from the Intergovernmental Panel on Climate Change (IPCC) (2001).

Table 4.6: Likely optical properties for dry biomass-burning smoke at 550 nm, estimated by Reid et al. (2005b) in Table 4.3.

Parameter	IPCC Fresh	IPCC Aged	Temperate/Boreal Forest Fresh	Temperate/Boreal Forest Aged	Grass/Savanna Fresh	Grass/Savanna Aged	Tropical Forest Fresh	Tropical Forest Aged
Mass extinction efficiency (m^2/g)	4.1±1.0	4.0±1.1	4.3±0.5	4.7±0.5	4.4±0.5	4.6±0.5	4.2±0.5	4.7±0.4
Mass scattering efficiency (m^2/g)	3.6±1.0	3.6±1.1	3.8±0.4	4.3±0.4	3.6±0.4	4.0±0.4	3.6±0.4	4.2±0.4
Mass absorbing efficiency (m^2/g)	0.54±0.2	0.45±0.2	0.5±0.3	0.4±0.3	0.80±0.3	0.65±0.3	0.6±0.3	0.50±0.2
Single scattering albedo	0.87±0.06	0.89±0.06	0.88±0.05	0.92±0.05	0.82±0.05	0.86±0.05	0.85±0.05	0.89±0.05
Hygroscopic growth, f (80%RH)	1.1±0.1	1.2±0.2	1.35±0.2	1.35±0.2	1.35±0.2	1.35±0.2	1.35±0.2	1.35±0.2

In this work we are interested not in the individual scattering and absorption efficiencies but their sum, the total particulate extinction efficiency α_e . As shown in Table 4.6, the recommended average dry α_e for fresh and aged smoke from the different biomass has a relatively small variation of 4.3–4.7 m^2/gm , with an uncertainty of about 0.5 m^2/gm . These average values are higher than the IPCC (2001) recommendations from 2001 of $\sim 4 \pm 1 \text{ m}^2/\text{gm}$.

We can test the suitability of the Reid et al. (2005b) estimate against the more recent chamber and field study results in Table 4.2. Note the stack burn results in Table 4.2 are not taken into account here since they are not representative of real-world fires. In Table 4.2, the average α_e for the western U.S. fuels is $4.1 \pm 0.9 \text{ m}^2/\text{gm}$. The chamber studies measured relatively young smoke, and these values are similar to the temperate/boreal α_e for fresh smoke of $4.3 \pm 0.5 \text{ m}^2/\text{gm}$. In addition, a wild or prescribed fire will likely burn a combination of wood, shrubs, and grasses, and the variability in α_e should be less than estimated from the chamber study. The results from the Yosemite study (Malm et al., 2005a) are also consistent with the Reid et al. (2005b) results, with $\alpha_e \sim 4.5 \text{ m}^2/\text{g}$ for the young smoke from a mix of wild and prescribed fires. The aged, cloud-processed smoke sampled in the Yosemite study with $\alpha_s \sim 5.5 \text{ m}^2/\text{g}$ validates the upper uncertainty bounds.

Based on these results, we recommend using an average of the Reid et al. (2005b) temperate/boreal α_e for fresh and aged smoke as a typical North America smoke dry α_e . Therefore, North America smoke dry $\alpha_e = 4.5 \pm 1.0 \text{ m}^2/\text{g}$.

As shown in Table 4.6, Reid et al. (2005b) recommend an $f(80\%) = 1.35 \pm 0.5$. This is a crude estimate based on averaging results from two non-North-American field studies. The Yosemite study (Malm et al., 2005a) measured a lower $f(80\%)$ of 1.1–1.2, indicating that $f(80\%) = 1.35$ may be too high. Tables 4.2, 4.4, and 4.5 have measured smoke hygroscopicity and/or inorganic salts content for a number of fuels burned in North America. As discussed, the hygroscopicity varied significantly by fuel type, e.g., trees, shrubs, and grasses. Aging and most likely other

biomass burning characteristics such as moisture content and combustion phase are important, but the data to evaluate their influence are not available.

Using the $f(80\%)$ in Table 4.5 and deriving $f(80\%)$ from the inorganic salt contents in Table 4.2, an average $f(80\%)$ for trees, shrubs, and grass was estimated as 1.1, 1.5, and 1.2, respectively. Assuming a fire burns equal amounts of each fuel, a typical $f(80\%)$ for North American fires is 1.3 with a standard deviation of ~ 0.2 . Therefore, we recommend an $f(80\%) = 1.3 \pm 0.2$ and a 95% confidence interval of 1 to 1.7. This range encompasses most of the field study data taken to date. A lower bound of 1 is used since it is unlikely that increased RH will decrease scattering.

At an RH of 80%, the recommended North America smoke α_e would be about $5.3 \pm 1 \text{ m}^2/\text{g}$ and a corresponding 95% confidence interval of 3.3–7.3. However, $f(\text{RH})$ is highly nonlinearly dependent on RH, and RH varies widely with location, time of day, and current meteorology. For example, higher RH generally occurs in the morning compared to daytime, and during summer months, RH will often be low in the arid western United States, with correspondingly low hygroscopic growth and $f(\text{RH}) \sim 1$, but in the southeastern United States, RH is regularly above 80%, with $f(\text{RH}) > 1.3$. Therefore any α_e based on an assumed RH will have large uncertainties.

4.3 Mass Scattering Efficiencies Derived from IMPROVE Data.

4.3.1 IMPROVE Monitoring Program

The Interagency Monitoring of Protected Visual Environments (IMPROVE) monitoring network consists of about 181 sites, approximately 170 of which are in nonurban areas. Their names and abbreviations are listed in Table 4.7. The $\text{PM}_{2.5}$ speciation target analytes consist of an array of ions, carbon species, and trace elements (Malm et al., 1994). Each series of analytes requires sample collection on an appropriate filter medium to allow chemical analysis with methods of adequate sensitivity. The methods used for analyses of these filter media include gravimetry (electro-microbalance) for mass; energy dispersive x-ray fluorescence for trace elements; ion chromatography (IC) for anions and cations; and controlled-combustion thermal optical transmittance and reflectance (TOT/TOR) analysis for carbon.

It is assumed that sulfates are fully neutralized as ammonium sulfate, nitrates are in the form of ammonium nitrate, organic carbon mass is estimated from measured organic carbon that has been estimated using TOT/TOR techniques, soil mass is estimated assuming oxide forms of measured soil elements, and sea salt is estimated from chloride measurements (Malm et al., 1994, 2004). Each of these estimates may be high or low, depending on the actual molecular composition of the aerosol. Semivolatile organic compound (SVOC) species may volatilize, causing organic carbon to be underestimated, while the Roc factor (organic mass/organic carbon) varies as a function of carbon molecular structure.

Table 4.7: A list of the names of each IMPROVE monitoring site along with its abbreviation and its latitude and longitude coordinates.

Abbreviation	Name	Lon	Lat
ACAD	Acadia National Park ME	-90.9567	44.3771
ADPI	Addison Pinnacle NY	-96.3259	42.0911
AGTI	Agua Tibia CA	-120.182	33.4637
AREN	Arches National Park UT	-96.3847	39.9231
BADL	Badlands National Park SD	-111.165	43.7435
BALD	Mount Baldy AZ	-115.664	34.0584
BAND	Bandalier National Monument NM	-113.76	35.7797
BIBE	Big Bend National Park TX	-111.907	29.3028
BLIS	Bliss State Park CA	-122.061	38.9756
BLMO	Blue Mounds MN	-107.715	42.7158
BOAP	Bosque del Apache NM	-114.111	33.8695
BOND	Bondville IL	-103.023	40.0514
BOWA	Boundary Waters Canoe Area MN	-104.898	47.9464
BRCA	Bryce Canyon National Park UT	-117.304	37.6184
BRET	Breton LA	-103.524	29.1186
BRID	Bridger Wilderness WY	-115.854	42.9749
BRIG	Brigantine National Wildlife Refuge NJ	-94.6695	39.465
BRLA	Brooklyn Lake WY	-113.745	41.3662
BRMA	Bridgton ME	-92.4376	44.1074
CABA	Casco Bay ME	-92.0386	43.8325
CABI	Cabinet Mountains MT	-119.403	47.955
CACO	Cape Cod MA	-92.0148	41.9758
CACR	Caney Creek AR	-106.486	34.4543
CADI	Cadiz KY	-102.71	36.7854
CANY	Canyonlands National Park UT	-115.893	38.4587
CAPI	Capitol Reef National Park UT	-116.776	38.3022
CEBL	Cedar Bluff KS	-109.94	38.7
CHAS	Chassahowitzka National Wildlife Refuge FL	-99.5329	28.7485
CHER	Cherokee Nation OK	-108.21	36.9333
CHIR	Chiricahua National Monument AZ	-115.633	32.0089
CLPE	Cloud Peak WY	-114.174	44.3335
COGO	Columbia Gorge WA	-123.327	45.5695
COHI	Connecticut Hill NY	-95.9921	42.4009
COHU	Cohutta GA	-100.776	34.7852
CORI	Columbia River Gorge WA	-122.614	45.6678
CRES	Crescent Lake NE	-111.46	41.7627
CRLA	Crater Lake National Park OR	-123.282	42.8962

Abbreviation	Name	Lon	Lat
CRMO	Craters of the Moon National Park ID	-118.133	43.4606
DENA	Denali National Park AK	-139.381	63.7233
DEVA	Death Valley National Park CA	-120.108	36.5088
DOME	Dome Lands Wilderness CA	-120.883	35.7279
DOSO	Dolly Sods Wilderness WV	-97.6558	39.107
ELDO	El Dorado Springs MO	-106.421	37.69
ELLI	Ellis OK	-109.961	36.0852
EVER	Everglades National Park FL	-98.4084	25.391
FLAT	Flathead MT	-118.561	47.7734
FOPE	Fort Peck MT	-113.061	48.308
GAMO	Gates of the Mountains MT	-117.026	46.8263
GICL	Gila Wilderness NM	-114.941	33.2204
GLAC	Glacier National Park MT	-118.398	48.5105
GRBA	Great Basin National Park NV	-118.53	39.0052
GRCA	Grand Canyon National Park AZ	-117.19	35.9731
GRGU	Great Gulf Wilderness NH	-92.7306	44.3082
GRR1	Great River Bluffs MN	-104.843	43.9374
GRSA	Great Sand Dunes National Monument CO	-113.311	37.7249
GRSM	Great Smoky Mountains National Park TN	-100.365	35.6334
GUMO	Guadalupe Mountains National Park TX	-112.886	31.833
HALE	Haleakala National Park HI	-143.769	20.8086
HAVO	Hawaii Volcanoes National Park HI	-143.155	19.4309
HECA	Hells Canyon OR	-120.104	44.9932
HEGL	Hercules-Glades MO	-105.727	36.6713
HILL	Hillside AZ	-117.778	34.4289
HOOV	Hoover CA	-121.506	38.0887
IKBA	Ike's Backbone AZ	-117.009	34.3403
INGA	Indian Gardens AZ	-117.277	36.0776
ISLE	Isle Royale National Park MI	-102.887	47.4607
JARB	Jarbidge Wilderness NV	-119.256	41.8926
JARI	James River Face Wilderness VA	-97.7075	37.6266
JOSH	Joshua Tree National Park CA	-119.833	34.0695
KAIS	Kaiser CA	-121.493	37.2181
KALM	Kalmiopsis OR	-124.435	42.5519
LABE	Lava Beds National Monument CA	-122.904	41.7117
LASU	Lake Sugema IA	-105.193	40.6883
LAVO	Lassen Volcanic National Park CA	-122.947	40.5403
LIGO	Linville Gorge NC	-99.1599	35.9722
LIVO	Livonia IN	-101.756	38.5347

Abbreviation	Name	Lon	Lat
LOST	Lostwood ND	-111.441	48.642
LYBR	Lye Brook Wilderness VT	-93.876	43.1481
MACA	Mammoth Cave National Park KY	-101.689	37.1315
MELA	Medicine Lake MT	-112.685	48.4872
MEVE	Mesa Verde National Park CO	-115.094	37.1984
MING	Mingo MO	-104.086	36.9717
MKGO	M.K. Goddard PA	-98.0867	41.4269
MOHO	Mount Hood OR	-123.062	45.2927
MOMO	Mohawk Mountain CT	-93.9784	41.8214
MONT	Monture MT	-117.893	47.1222
MOOS	Moosehorn National Wildlife Refuge ME	-90.3597	45.1259
MORA	Mount Rainier National Park WA	-123.274	46.7579
MOZI	Mount Zirkel Wilderness CO	-114.006	40.5383
NEBR	Nebraska National Forest NB	-110.203	41.8887
NOAB	North Absaroka WY	-115.629	44.7448
NOCA	North Cascades WA	-122.639	48.7316
NOCH	North Cheyenne MT	-113.934	45.6493
OKEF	Okefenokee National Wildlife Refuge GA	-99.277	30.7404
OLTO	Old Town ME	-91.1874	44.9335
OLYM	Olympic WA	-123.784	48.0065
PASA	Pasayten WA	-121.957	48.3877
PEFO	Petrified Forest National park AZ	-115.861	35.0781
PHOE	Phoenix AZ	-117.257	33.5038
PINN	Pinnacles National Monument CA	-122.693	36.485
PMRF	Proctor Maple Research Farm VT	-93.7212	44.5286
PORE	Point Reyes National Seashore CA	-123.747	38.1199
PRIS	Presque Isle ME	-90.8201	46.6963
PUSO	Puget Sound WA	-123.387	47.5696
QUCI	Quaker City OH	-98.8027	39.9429
QURE	Quabbin Summit MA	-93.401	42.2988
QUVA	Queen Valley AZ	-116.771	33.2939
RAFA	San Rafael CA	-122.004	34.7339
REDW	Redwood National Park CA	-124.451	41.56
ROMA	Cape Romain National Wildlife Refuge SC	-97.7943	32.9415
ROMO	Rocky Mountain National Park CO	-113.327	40.2783
SACR	Salt Creek NM	-112.643	33.4597
SAFO	Sac and Fox KS	-107.341	39.9789
SAGA	San Gabriel CA	-120.817	34.2969
SAGO	San Geronio Wilderness CA	-120.141	34.1924

Abbreviation	Name	Lon	Lat
SAGU	Saguaro National Monument AZ	-116.442	32.1742
SAMA	St. Marks FL	-100.497	30.0926
SAPE	San Pedro Parks NM	-114.107	36.014
SAWE	Saguaro West AZ	-116.731	32.2486
SAWT	Sawtooth National Forest ID	-118.957	44.1706
SENE	Seney MI	-101.568	46.2881
SEQU	Sequoia National Park CA	-121.298	36.4894
SHEN	Shenandoah National Park VA	-97.0608	38.5229
SHRO	Shining Rock Wilderness NC	-99.6646	35.3937
SIAN	Sierra Ancha AZ	-116.565	34.0909
SIKE	Sikes LA	-105.46	32.058
SIME	Simeonof AK	-146.304	55.3255
SIPS	Sipsy Wilderness AL	-102.403	34.3433
SNPA	Snoqualmie Pass WA	-122.857	47.4204
SPOK	Spokane Reservation WA	-120.717	47.9045
STAR	Starkey OR	-121.108	45.2249
SULA	Sula Peak MT	-118.4	45.8599
SWAN	Swanquarter NC	-95.7244	35.451
SYCA	Sycamore Canyon AZ	-117.182	35.1406
TALL	Tallgrass KS	-107.96	38.3
THBA	Thunder Basin WY	-113.172	44.6634
THRO	Theodore Roosevelt ND	-112.027	46.8948
THSI	Three Sisters Wilderness OR	-123.226	44.291
TONT	Tonto NM	-116.665	33.6494
TRCR	Trapper Creek AK	-140.189	62.3153
TRIN	Trinity CA	-123.683	40.7865
TUXE	Tuxedni AK	-141.599	59.9925
ULBE	UL Bend MT	-115.232	47.5823
UPBU	Upper Buffalo Wilderness AR	-105.922	35.8259
VIIS	Virgin Islands National Park	-88.877	18.3384
VILA	Viking Lake IA	-107.026	40.9712
VOYA	Voyageurs National Park MN	-105.697	48.4126
WASH	Washington D.C.	-96.2206	38.8761
WEMI	Weminuche Wilderness CO	-114.68	37.6594
WHIT	White Mountain NM	-113.314	33.4698
WHPA	White Pass WA	-122.833	46.6244
WHPE	Wheeler Peak NM	-113.271	36.5855
WHRI	White River National Forest CO	-114.091	39.1517
WICA	Wind Cave SD	-112.09	43.5577

Abbreviation	Name	Lon	Lat
WIMO	Wichita Mountains OK	-109.229	34.7315
YELL	Yellowstone National Park WY	-116.24	44.5653
YOSE	Yosemite National Park CA	-121.823	37.7125
ZION	Zion National Park UT	-117.935	37.4591

Background or ambient extinction and mass other than an increase in smoke aerosol due to wildfire or control burn is given by

$$TM_{bg} = aSO_4 + aNO_3 + POM_{bg} + LAC_{bg} + SS + soil + CM \quad 4.3$$

where aSO_4 , aNO_3 , POM, LAC, SS, soil, and CM refer to ammonium sulfate, ammonium nitrate, particle organic mass, light absorbing carbon, sea salt, soil, and coarse mass of the ambient or background aerosol, respectively. Combining some terms

$$TM_{bg} = H + POM_{bg} + LAC_{bg} + R \quad 4.4$$

where $H = aSO_4 + aNO_3$ and $R = SS + soil + CM$.

Then,

$$b_{ext,bg} = \alpha_1 f(RH)H + \alpha_2 POM_{bg} + \alpha_3 LAC_{bg} + \alpha_4 R. \quad 4.5$$

α_1 , α_2 , α_3 , and α_4 are the mass scattering or extinction coefficients for ammonium sulfate and nitrate, POM, LAC, and the residual mass term R, respectively. Hand and Malm (2007), incorporating the review of mass scattering and extinction coefficients discussed above, suggest $\alpha_1 = 2.9$, $\alpha_2 = 3.7$, and $\alpha_3 = 10.0 \text{ m}^2/\text{gm}$. It also follows that $\alpha_4 = \frac{1.0}{R} soil + \frac{1.37}{R} SS + \frac{0.6}{R} CM$ where 1.0, 1.37, and 0.6 m^2/gm are the mass scattering efficiencies of soil, SS, and CM, respectively. $f(RH)$ is the increase in scattering as a function of the RH factor associated with hygroscopic aerosols. Equation 1.70 also assumes that POM is not hygroscopic, and therefore any ambient POM concentrations that are due to smoke aerosol in the IMPROVE monitoring database are not hygroscopic.

An average “wet” extinction to mass ratio can then be estimated by dividing equation 4.2 by 4.1 yielding

$$\alpha_{ext,wet} = \frac{b_{ext,bg}}{TM_{bg}} \quad 4.6$$

where $\alpha_{ext,wet}$ is the extinction to mass ratio of a wet aerosol.

4.3.2 Derived Average Mass Extinction Coefficients Using IMPROVE Data

Figure 4.1 is a plot of yearly average wet mass extinction efficiencies α for each of the IMPROVE monitoring locations. Figure 4.1 should be compared to Figure 3.2 where average α values were derived from independent nephelometer-measured scattering and mass measurements. Keep in mind that the nephelometer-derived mass extinction efficiencies neglected the scattering contribution of coarse mass (CM), while IMPROVE-derived mass extinction efficiencies do include coarse mass.

The two figures are quite similar, both showing lower α values of less than $2 \text{ m}^2/\text{gm}$ in the Intermountain West and over $5 \text{ m}^2/\text{gm}$ in the eastern and northwestern United States. The higher mass extinction efficiencies are due to absorbed water on hygroscopic aerosol species. The lower mass extinction efficiencies in the southwestern United States are a result of the contribution of CM with its low mass scattering efficiencies to total extinction. It is emphasized that any V_r observation will be dependent on CM as well as PM concentrations. Assuming $V_r \text{PM} = \text{CNST}$ and $\text{CNST} = 3912/\alpha$, a $2 \text{ m}^2/\text{gm}$ mass extinction efficiency corresponds to a $V_r * \text{PM} = 1950$, while a $5 \text{ m}^2/\text{gm}$ efficiency corresponds to $V_r * \text{PM} = 780$.

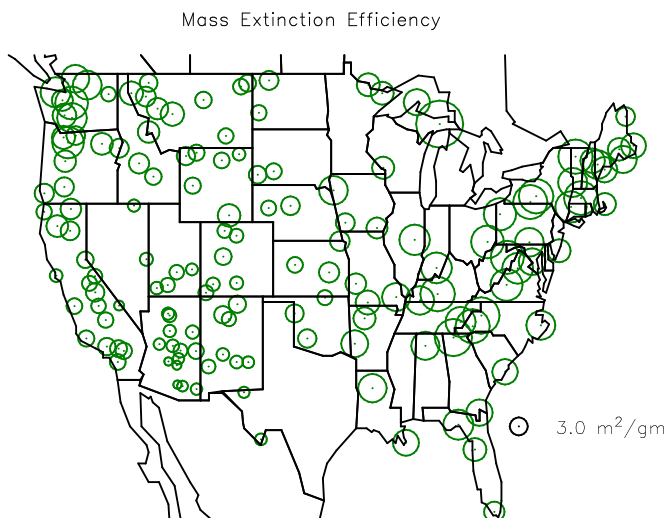


Figure 4.1: Yearly average mass extinction efficiencies for each of the IMPROVE monitoring locations.

Figure 4.2 is a plot of the same data as shown in Figure 4.1 along with the standard deviation of the calculated α values. The order of the sites presented in Figure 4.2 is from west to east. The standard deviation of α resulting from a variable mix of aerosols is a measure of the uncertainty in assuming some constant α over all time periods. The standard deviation varies from less than one in the Intermountain West to about 1.7 in the eastern and northeastern United States. Figure 4.2 should be compared to Table 3.2 in which standard deviations of mass scattering efficiencies were calculated from measured scattering and mass concentrations as opposed to calculating them from IMPROVE aerosol measurements and an algorithm to estimate scattering. The scattering measurement used to estimate mass scattering efficiencies included the effects of RH

as well as variability in the particle species mix. Both methods of estimating the standard deviation of mass scattering efficiencies yield about the same variability. The variability in mass scattering efficiency varies from a low near one up to a maximum near two. The higher variability is found for those sites where RH is higher such as the eastern and northwestern monitoring locations. It is this variability in α that will be used to estimate the variability in mass determination from a V_T observation resulting from an unknown background aerosol mix (see equation 5.5).

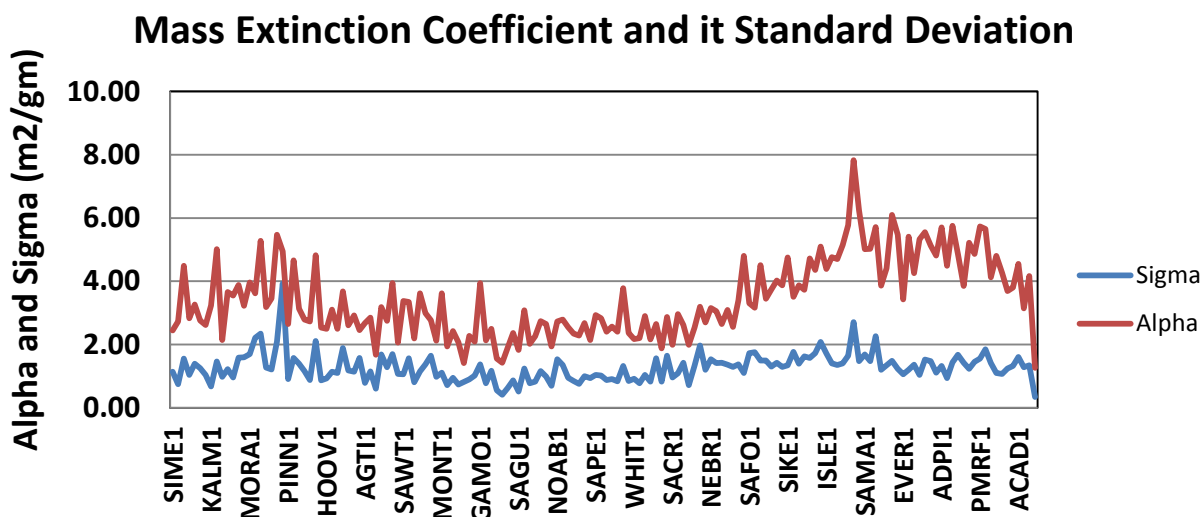


Figure 4.2: Plot of average mass extinction efficiency and its standard deviation for each of the IMPROVE monitoring sites.

Assuming $CNST = 3912/\alpha$, the proportionality constant can be calculated for each monitoring site. These values are plotted in Figure 4.3 and also in Figure 4.4 along with the $CNST = 622$ derived in the O'Neill analysis. $CNST$ varies from about 1700 in the West to values near but greater than 622 in the East. The higher $CNST$ values in the West reflect an aerosol with lower fractions of hygroscopic particles than in the eastern United States in combination with lower RH and relatively higher concentrations of CM.

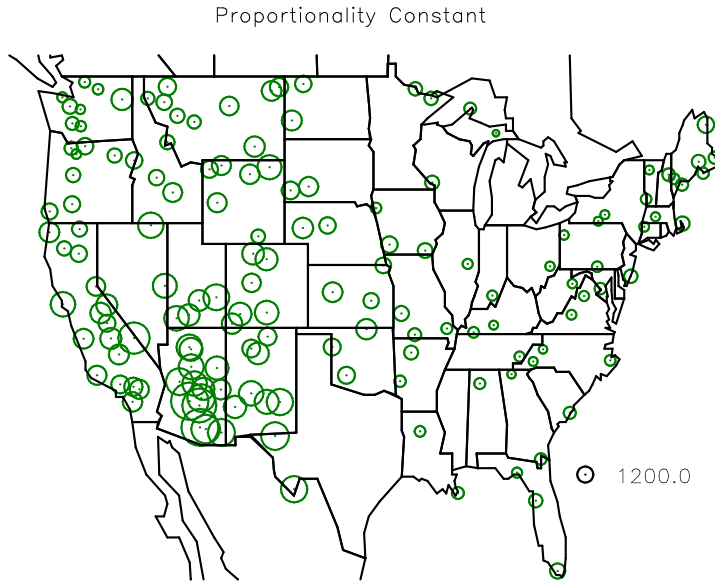


Figure 4.3: The proportionality constant between V_r and PM. $CNST = 3912/\alpha$.

Notice that in the East the CNST level is near the 622 suggested by the O'Neill (2013) analysis. The lower CNST values in the East reflect the higher wet mass extinction coefficients associated with high background levels of sulfates and nitrates in combination with higher RH levels. They do not reflect high mass extinction coefficients that are linked to smoke aerosols as implied in the O'Neill et al. (2013) analysis.

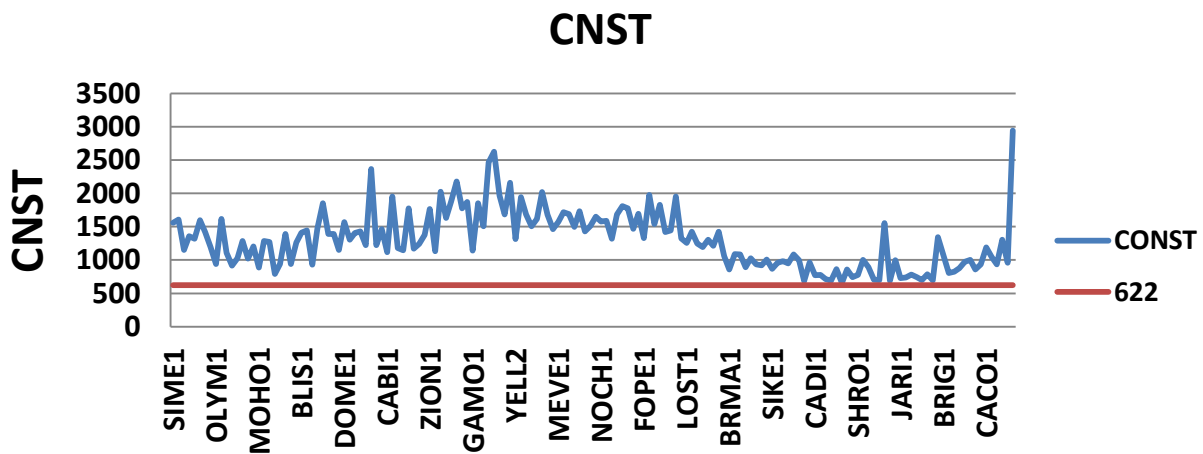


Figure 4.4: The proportionality constant between V_r and PM derived from $CNST = 3912/\alpha$ and $CNST = 622$.

4.4 Effect of Background Aerosol and RH Levels on PM Estimates, Assuming an Average Seasonal and Nationwide Mass Scattering Efficiency or CNST.

Total extinction, background plus smoke, is

$$b_{ext} = b_{ext,s} + b_{ext,bg} \quad 4.7$$

where

$$b_{ext,s} = \alpha TC_s = \alpha_2 POM_s + \alpha_3 LAC_s \quad 4.8$$

and total dry smoke mass TM_s is

$$TM_s = POM_s + LAC_s. \quad 4.9$$

Therefore

$$\alpha_s = \frac{3.7}{TM_s} POM_s + \frac{10.0}{TM_s} LAC_s. \quad 4.10$$

The average absorption albedo averaged across all sites, $\frac{LAC_s}{LAC_s + POM_s}$, is approximately 0.11. As such, $POM_s = 0.89TM_s$ and $LAC_s = 0.11TC_s$. Therefore $\alpha_s = 4.5 \text{ m}^2/\text{gm}$, which is the same as the best-estimate dry smoke mass extinction efficiency obtained from the literature review of smoke aerosol physical and optical properties.

Now,

$$TM_s = b_{ext,s}/\alpha_s = (b_{ext} - b_{ext,bg} - b_{ray})/\alpha_s. \quad 4.11$$

Then,

$$\begin{aligned} TM = TM_s + TM_{bg} &= (b_{ext}(RH) - b_{ext,bg}(RH) - 10) / 4.5 + TM_{bg} \\ &= \left(\frac{3.91}{V_r(RH)} - b_{ext,bg}(RH) - 10 \right) / 4.5 + TM_{bg} \end{aligned} \quad 4.12$$

which expresses total mass TM in terms of observed visual range V_r . It is also possible to write V_r in terms of TM :

$$V_r = 3.91 / (4.5TM_s + b_{ext,bg}(RH) + 10) \quad 4.13$$

In equation 4.12, if $b_{bg}(RH)$ and $b_{ext}(RH)$ are estimated at the same RH and smoke is assumed not to be hygroscopic, then TM is total dry mass or background mass plus incremental smoke mass. If $b_{ext}(RH)$ is calculated at some RH while $b_{bg}(RH)$ is calculated at $RH = 0$, then TM is the mass of the dry aerosol plus water. If TM_w is referred to as total mass plus water or wet mass and TM as dry mass, then water mass is

$$TM_{water} = TM_w - TM \quad 4.14$$

or

$$TM_{water} = \frac{\alpha_1 H}{\alpha_s} (f(RH) - 1) \quad 4.15$$

where the variables are defined above.

4.5 How Much Is Mass Estimate Inflated Because of Background Aerosol Hygroscopicity?

If the goal of a V_r observation is to estimate an ambient mass concentration, the relative level of hygroscopic to nonhygroscopic species is critical. Under even moderate RH conditions the scattering efficiencies of salts like ammonium sulfate or nitrate are increased significantly, and the resulting V_r will be decreased, not because of increase in dry ambient mass concentrations but because of absorbed water on the hygroscopic species. Therefore the effect of background aerosol concentration and RH on the estimation of ambient mass concentration from a V_r estimation will be explored. Humidity and therefore $f(RH)$ values vary significantly by area of the country and season, with lower RH levels found in the western United States. An average humidity and $RH = 90\%$ will be used, and average background and average background plus one standard deviation of each aerosol species will be explored. If concentrations are normally distributed, 16% of ambient concentrations will be greater than one sigma above the mean and 16% will be lower than the average minus one standard deviation.

In this next section, a constant α_s will be assumed and the amount of retained water due to background aerosol hygroscopicity will be explored at each of the IMPROVE sites.

4.5.1 Increase in Mass Concentration Due to Retained Water

Equation 4.15 allows for a calculation of water mass associated with background aerosols and would be included in any estimation of mass from a V_r estimate. TM_{water} is essentially an error term in that what is desired from a health, National Ambient Aerosol Quality Standard (NAAQS), or AQI standpoint is dry mass, the mass associated with visual range, is total mass or dry mass plus water mass.

Water mass will always be in addition to dry mass, so a background water mass of $35 \mu\text{g}/\text{m}^3$ creates an error of nearly 100% for a background dry mass of $38 \mu\text{g}/\text{m}^3$, but only about a 7% error if the background mass concentration is $500 \mu\text{g}/\text{m}^3$. In other words, as the ambient mass associated with smoke approaches high levels, the uncertainty associated with background water mass becomes smaller.

Figure 4.5 shows that the amount of water mass at $RH = 90\%$ is associated with average background hygroscopic aerosol concentrations at each of the IMPROVE monitoring sites, while Figure 4.6 is the same plot but with the background hygroscopic concentration set to average plus one standard deviation. The water associated with this background concentration of sulfate plus nitrate would only be exceeded about 8% of the time. The average background aerosol concentration was calculated as an average over a time period from 1992 to 2004.

At 90% RH and average background aerosol concentrations, water mass is significant at about $35 \mu\text{g}/\text{m}^3$ in much of the central-eastern United States, while at average plus one standard deviation, the water mass in the same region is near $70 \mu\text{g}/\text{m}^3$. A mass estimate from a V_r observation of measurement in the eastern United States can significantly overestimate the dry mass concentration. In the central mountainous western United States, the overestimate is small at only a few $\mu\text{g}/\text{m}^3$ for average background aerosol concentrations and about $5\text{--}10 \mu\text{g}/\text{m}^3$ for an average background plus one standard deviation.

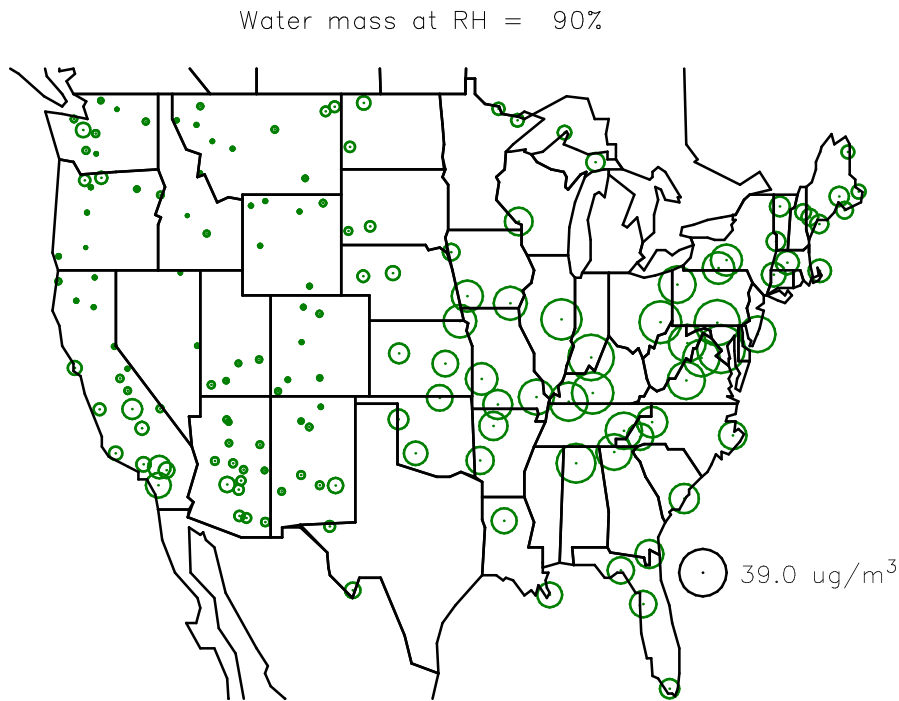


Figure 4.5: Amount of water mass concentration, assuming an average background particle concentration and $RH = 90\%$.

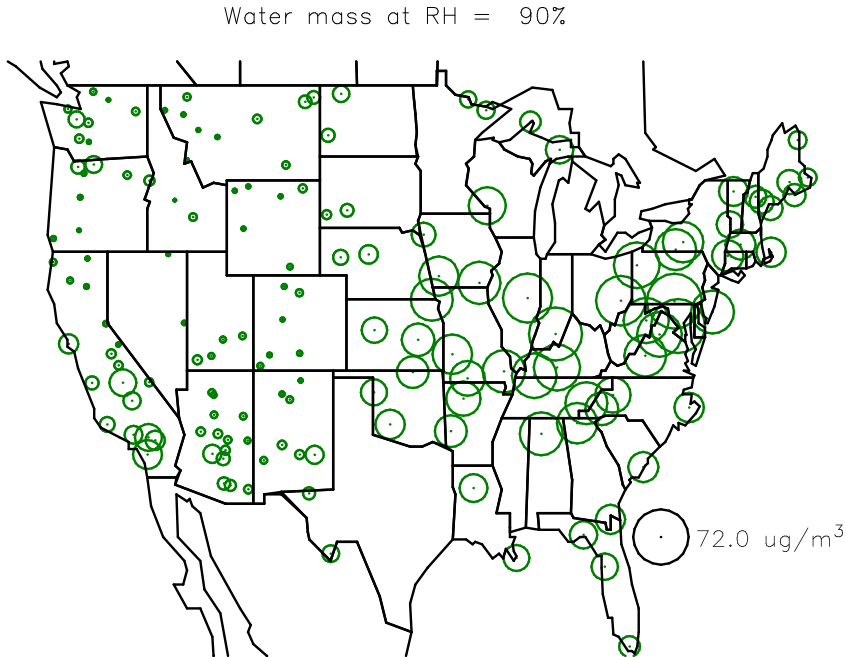


Figure 4.6: Amount of water mass concentration, assuming that the background particle mass is the average plus one standard deviation and an RH = 90%.

4.5.2 Examples of Uncertainty in Estimated Mass Concentration Due to Retained Water

The uncertainty in estimating true ambient mass concentration versus an implied mass concentration from an observed V_r that is dependent on background aerosol concentrations other than smoke will be explored.

The uncertainty of estimated mass concentration from a V_r observation will be dependent on both the uncertainty in α_s as well as the uncertainty in background concentration and RH.

An uncertainty term is calculated as

$$UNC = 100 * (TM_{implied} - TM_{true})/TM_{true} \quad 4.16$$

where $TM_{implied}$ and TM_{true} are the implied and true ambient mass concentrations, respectively. The implied mass concentration is calculated using equation 4.16. The calculation is carried out for the health derived mass concentration breakpoints shown in Figure 4.7 for the 1–3 hr mass concentration intervals. The PM smoke mass concentration is incremented above ambient concentrations so that the total mass concentration (background + smoke) is equal to the breakpoint shown in Figure 4.7.

Air Quality Index Category	PM _{2.5} or PM ₁₀ Levels (µg/m ³ , 1- to 3-hr avg.)	PM _{2.5} or PM ₁₀ Levels (µg/m ³ , 8-hr avg.)	PM _{2.5} or PM ₁₀ Levels (µg/m ³ , 24-hr avg.)
Good	0 – 38	0 – 22	0 – 12
Moderate	39 – 88	23 – 50	12.1 – 35.4
Sensitive Groups	89 – 138	51 – 79	35.5 – 55.4
Unhealthy	139 – 351	80 – 200	55.5 – 150.4
Very Unhealthy	352 – 526	201 – 300	150.5 – 250.4
Hazardous	≥ 526	> 300	> 250.5 - 500

Figure 4.7: Health breakpoints associated with 1–3 hr, 8 hr, and 24 hr average mass concentrations.

Figure 4.8 presents the uncertainty calculation associated with retained water for annual average $f(RH)$ and average annual aerosol mass concentrations and for the health breakpoint corresponding to $38.0 \mu\text{g}/\text{m}^3$. The uncertainty between real and implied mass ranges from about 37% down to less than a few percent in the Intermountain West. The maximum uncertainty occurs along the Ohio River valley where the annual average hygroscopic aerosol species are greatest, along with high average RH levels.

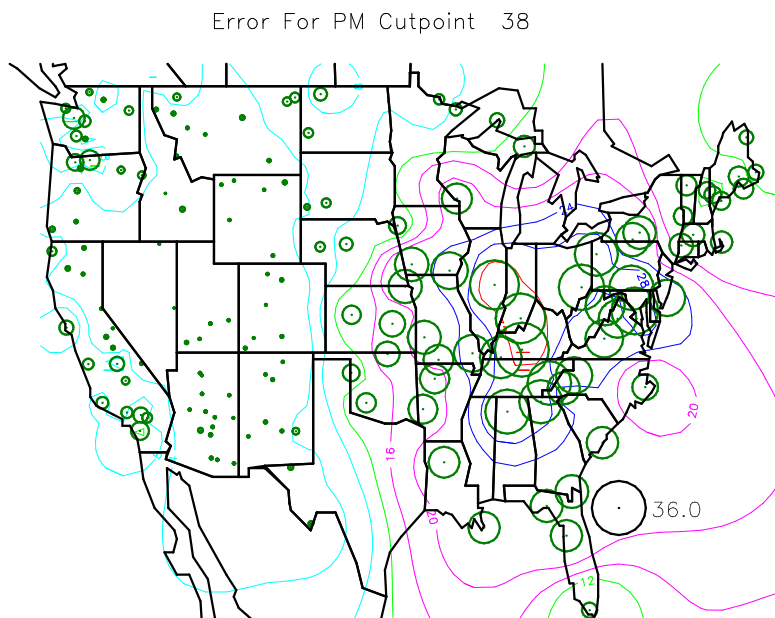
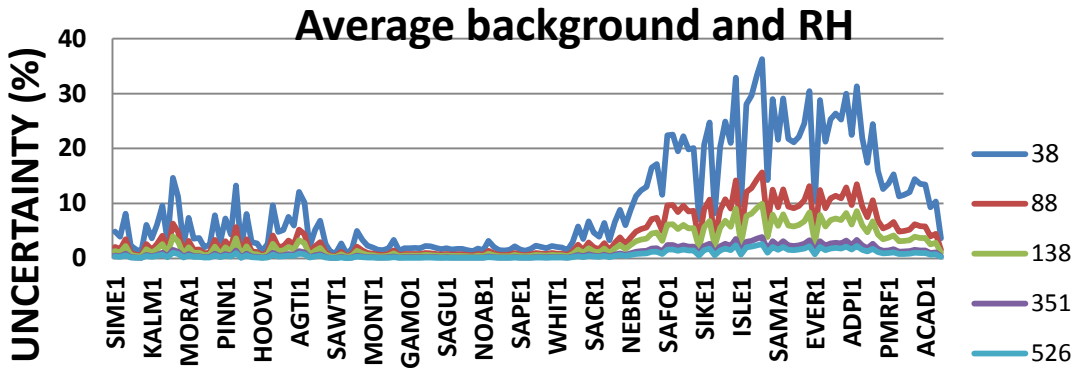


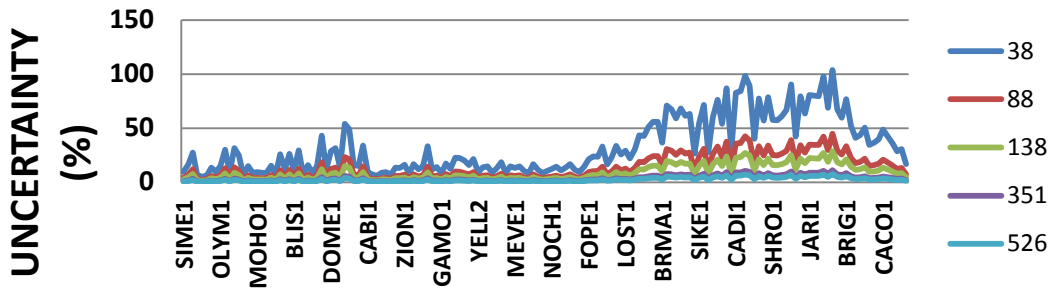
Figure 4.8: Uncertainty between implied mass concentration derived from a visual range observation and real mass concentrations for an average $f(RH)$ and average background .

Figure 4.9a summarizes the same data in a different way. The figure is a plot of uncertainty as defined by equation 4.13 for health breakpoints of 38, 88, 138, 351, and $526 \mu\text{g}/\text{m}^3$. The x axis is the IMPROVE monitoring sites plotted according to their longitudinal coordinates. Therefore the sites that are farthest west are on the left-hand side of the axis and eastern sites are on the right.



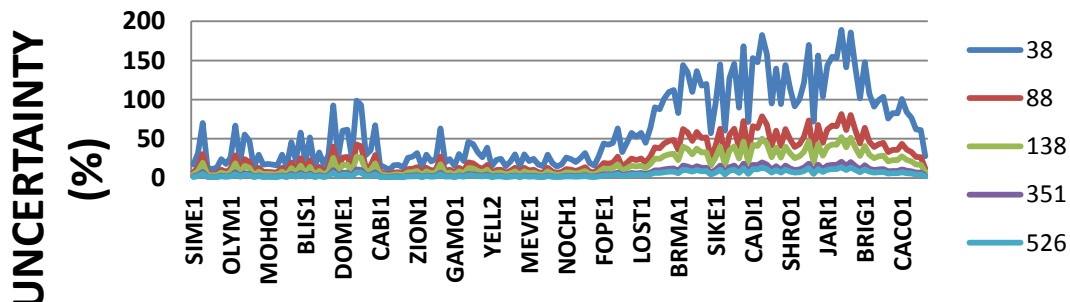
a

Average background and RH=90%



b

Average background + σ and RH=90%



c

Figure 4.9: “a” shows an average background aerosol concentration combined with an average $f(RH)$ value, while “b” and “c” correspond to an average background aerosol concentration but with an $f(RH)$ that corresponds to $RH = 90\%$ and an average background aerosol concentration plus one standard deviation associated with that background and $RH = 90\%$, respectively.

Figure 4.9a is for an average background aerosol concentration combined with an average $f(RH)$ value, while Figure 4.9b shows an average background aerosol concentration but with an $f(RH)$

that corresponds to $RH = 90\%$. Figure 4.9c shows the uncertainty for an average background aerosol concentration plus one standard deviation associated with that background and $RH = 90\%$.

Although the spatial patterns of uncertainty are similar for all three graphs, notice that the y axis scale for each graph is quite different. For an average background and RH , the scale is 0.0–40.0%, while for an average background plus one sigma and $RH = 90\%$, the scale extends to 200% uncertainty. The figures show that the sites with the lowest bias or uncertainty are in the West where hygroscopic species concentrations are lowest and highest along the Ohio River valley and the East in general where RH and hygroscopic species are highest. Also evident in all graphs is that as smoke, which is treated as a nonhygroscopic aerosol, concentrations are increased such that the atmospheric mass concentrations reach the identified health breakpoint, the uncertainty between implied and actual ambient mass decreases.

For average background and RH conditions, the error or uncertainty between implied and actual mass drops below about 10% for mass loadings above $88 \mu\text{g}/\text{m}^3$ and only a few percent for mass loadings above $138 \mu\text{g}/\text{m}^3$. However, for conditions where the concentrations are average plus one standard deviation and high RH levels, such as those that can occur during summer months, the error between implied and actual mass can be significant. In the eastern United States, implied mass is about a factor of 1.5 greater than true mass even at levels of $138 \mu\text{g}/\text{m}^3$. At levels above $351 \mu\text{g}/\text{m}^3$, the difference between true and implied mass drops to about 10%.

4.5.3 Uncertainty of Implied Mass When Using a Single Mass Extinction Efficiency

In this section the difference between an implied mass concentration and a “true” mass concentration based on some assumed but realistic aerosol optical and chemical parameters will be explored for illustrative purposes. First of all, assume a constant α of $6.3 \text{ m}^2/\text{gm}$, which corresponds to $CNST = 622$. The dry α for a smoke aerosol assumed in the “true” mass model is $4.5 \text{ m}^2/\text{gm}$ but could be any value from below $3.0 \text{ m}^2/\text{gm}$ to well above $6.0 \text{ m}^2/\text{gm}$ if the hygroscopic properties of smoke were included.

The next series of graphs compares implied mass to “true” mass for the same critical health mass concentrations discussed above. Figures 4.10 and 4.11 show the spatial distribution of this uncertainty, assuming average background and average RH conditions. Figure 4.10 shows that for an actual mass concentration of $38.0 \mu\text{g}/\text{m}^3$, the implied and actual mass compare quite favorably in parts of the United States. This is a consequence of the fact that the 622 relationship was derived from the IMPROVE dataset for average background and RH conditions, and because the higher background concentrations are found in the eastern United States, it is these sites that drive the curve fit between average mass RH conditions and the associated average V_r that yield the fitting parameter of 622. However, in the western United States, the implied mass is about 25% lower than true mass, while in parts of the Southwest, the underestimation is greater than 30%.

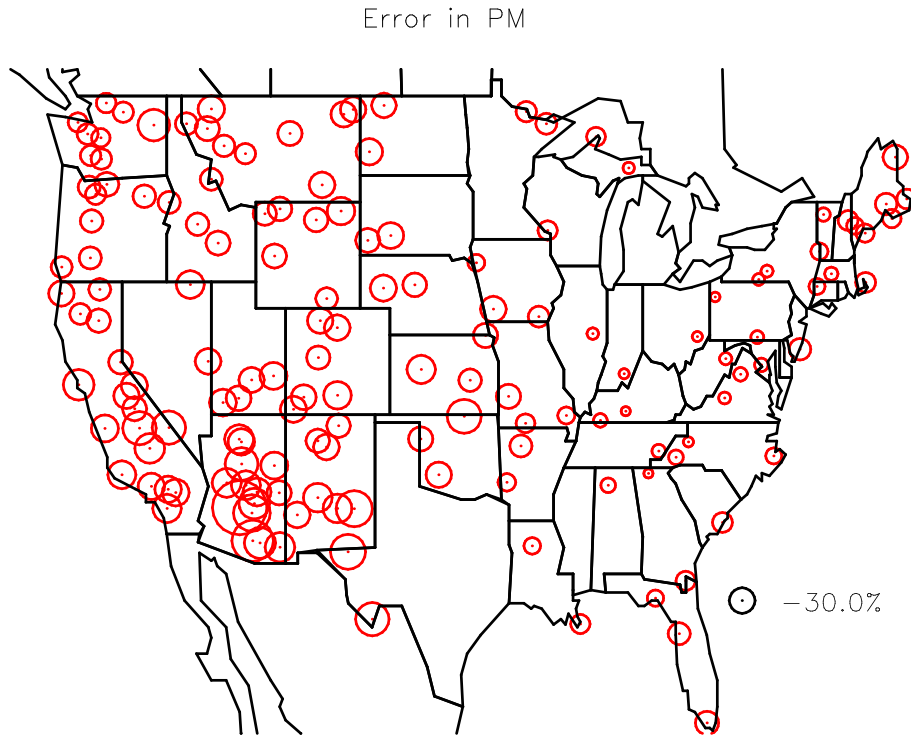


Figure 4.10: Average $f(\text{RH})$ and average background compared to $\text{TM} = 622/(\text{actual visual range})$ for a mass cutpoint of $38.0 \mu\text{g}/\text{m}^3$. Red color corresponds to implied mass being less than actual mass.

At higher mass loadings, the effect of background aerosol as compared to smoke mass becomes negligible. The difference between true and implied mass no longer depends on the concentration of hygroscopic species and ambient RH but rather on the difference between the actual mass extinction of the ambient smoke aerosol and the mass extinction coefficient implied by $\text{CNST} = 622$. In this illustrative example, it was assumed that the actual smoke extinction to mass ratio was $4.5 \text{ m}^2/\text{gm}$, while the constant 622 implies an α of about $6.3 \text{ m}^2/\text{gm}$.

These conclusions are highlighted in Figure 4.11 showing the uncertainty or bias between true mass and implied mass for the 622 relationship for all five mass concentration breakpoints. The plot again is for the all IMPROVE sites used in the analysis, with the westernmost sites on the left and the more eastern sites on the right. As ambient mass increases, the uncertainty for all sites approaches a constant value of about -27%, reflecting the difference in implied and actual smoke extinction to mass ratios.

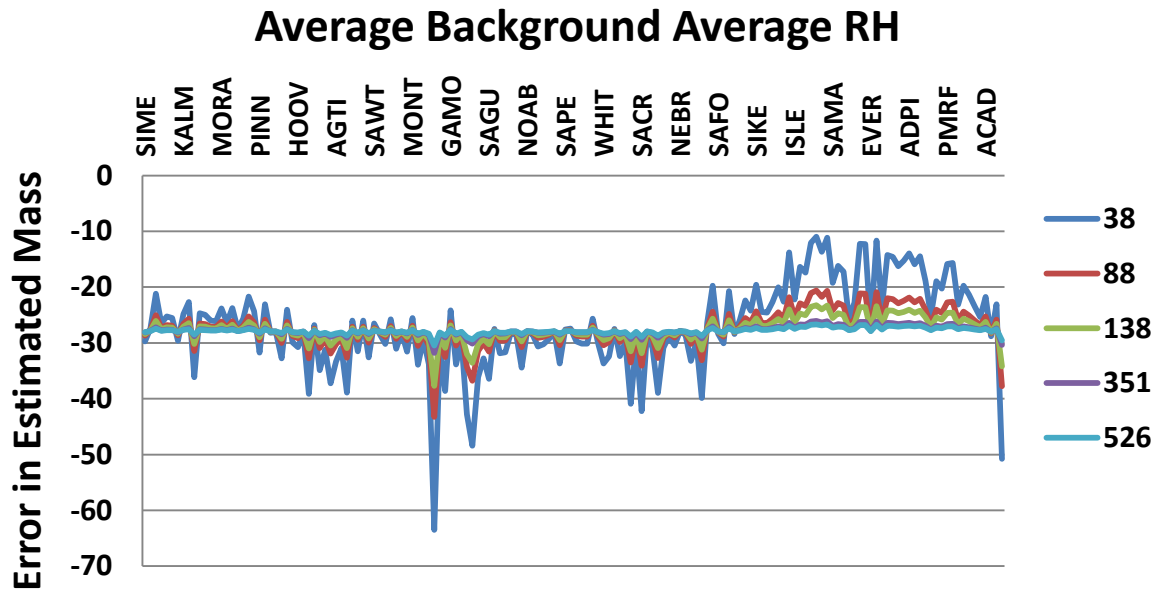


Figure 4.11: Plot of the percent difference between true mass and mass derived from $TM = 622/(\text{actual visual range})$ for average aerosol background and average RH for each IMPROVE site listed in Table 4.7. Order of sites is from west to east. The various colors correspond to the different mass concentration breakpoints associated with health endpoints.

Figures 4.12 and 4.13 show a similar set of plots but with the background RH set to 90%. The circle plot is for a mass concentration cutpoint of $38.0 \mu\text{g}/\text{m}^3$. Whereas in the average background and average RH case all the uncertainty values were negative, in the case of $RH = 90\%$, the V_r is low enough that the implied mass is greater than actual mass in the eastern United States, about the same in the central United States, and lower in the western portion of the United States. As in the average background, average RH case, as the mass concentration breakpoints increase, the uncertainty values approach approximately -27% , reflecting the inherent difference in the assumed extinction to mass ratio associated with smoke aerosol.

A point to be made here is that because a relationship such as the $622/V_r$ implies a constant extinction to mass ratio for all types of aerosols under all types of mass loadings and for all RH values, it will not reflect the changing characteristics of background aerosols or ambient RH conditions nor will it reflect the variability in smoke extinction to mass ratios.

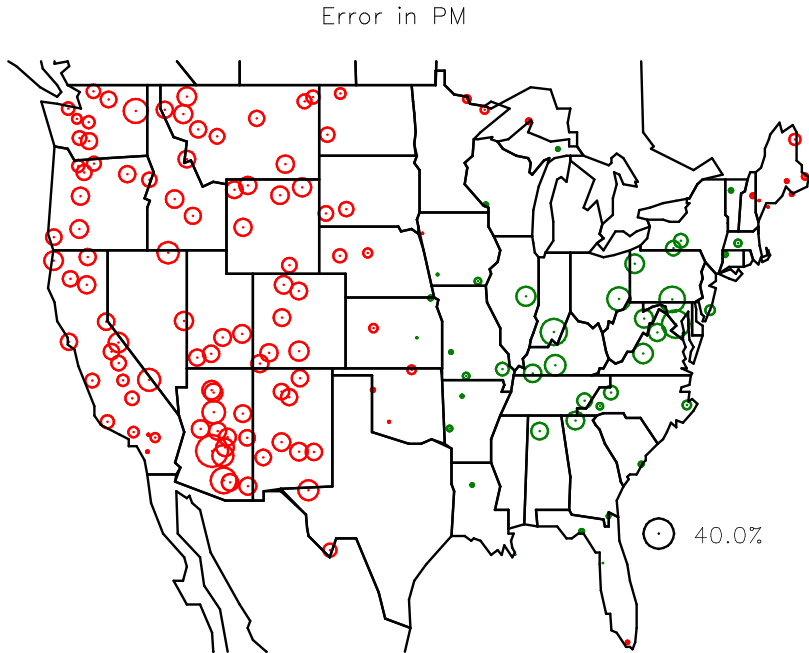


Figure 4.12: $f(\text{RH})$ corresponding to $\text{RH} = 90\%$ and average background compared to $\text{TM} = 622/(\text{actual visual range})$ for a mass cutpoint of $38.0 \mu\text{g}/\text{m}^3$. When implied mass is greater than actual mass, it is plotted in green, and when it is less than real mass, it is plotted in red.

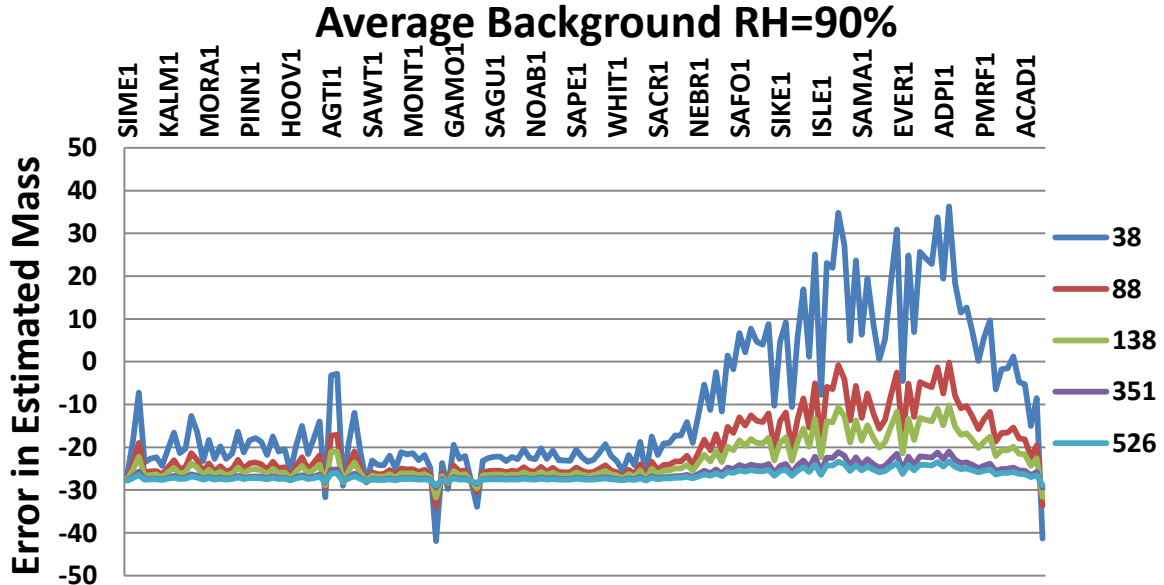


Figure 4.13: Plot of the percent difference between true mass and mass derived from $\text{TM} = 622/(\text{actual visual range})$ for average aerosol background and $\text{RH} = 90\%$ for each IMPROVE site listed in Table 4.7. Order of sites is from west to east. The various colors correspond to the different mass concentration breakpoints associated with health endpoints.

Figure 4.14 shows the same calculations as presented in Figures 4.12 and 4.13 but with the background aerosol concentrations equal to the mean plus one standard deviation and background RH = 90%. Here, the bias or uncertainty reaches 100% for 38.0 $\mu\text{g}/\text{m}^3$ in the eastern United States and is still 20% above its high mass limit of -27% and 138.0 $\mu\text{g}/\text{m}^3$.

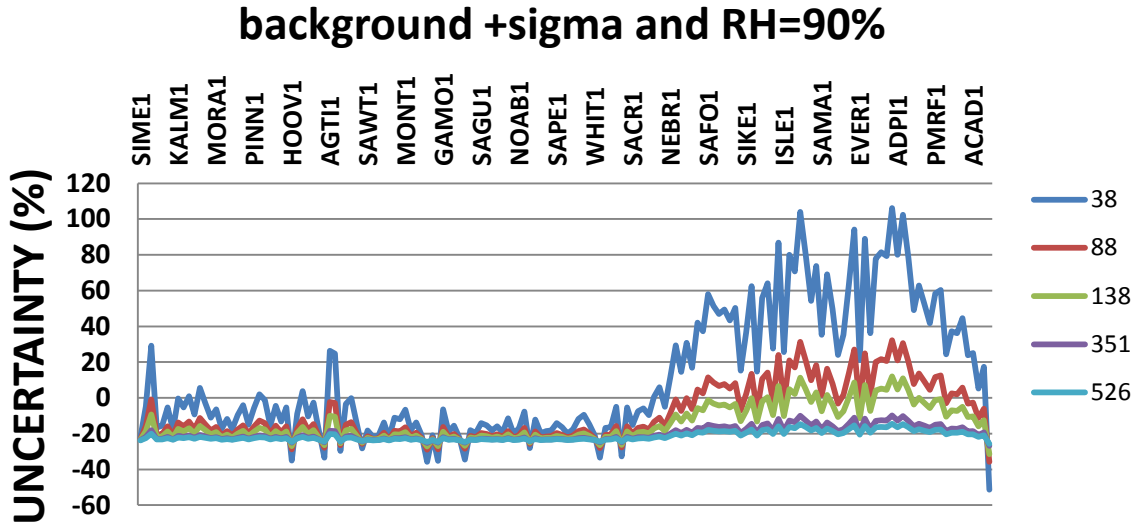


Figure 4.14: Plot of the percent difference between true mass and mass derived from $TM = 622/(\text{actual visual range})$ for average aerosol background plus one standard deviation and $RH = 90\%$ for each IMPROVE site listed in Table 4.7. Order of sites is from west to east. The various colors correspond to the different mass concentration breakpoints associated with health endpoints.

5. INTEGRATING ALL THE UNCERTAINTIES/VARIABILITIES IN THE MASS EXTINCTION EFFICIENCY INTO AN OVERALL UNCERTAINTY IN MASS ESTIMATE.

The previous analysis showed the uncertainty in mass estimations for some specific examples of background aerosol mass concentrations combined with various average background RH conditions. This section will address the overall uncertainty in mass determination directly associated with an uncertainty in the wet extinction to mass ratio α_w .

Equation 2.37 shows that

$$TM = \frac{3.912}{\alpha_w V_r} - \frac{b_{sg}}{\alpha_w} = \frac{3.912/\alpha_w}{V_r} - \frac{b_{sg}}{\alpha_w}. \quad 5.1$$

Differentiating equation 5.1 with respect to α_w yields

$$\frac{dTM}{d\alpha_w} = -\frac{3.912}{V_r \alpha_w^2} - \frac{10}{\alpha_w^2} \quad 5.2$$

The contribution of the Rayleigh term in equation 5.2 to mass is less than 7% to implied mass at $38.0 \mu\text{g}/\text{m}^3$, the first health cutpoint, and will be neglected in the following calculations. With this approximation, dividing equation 5.2 by 5.1 yields

$$\frac{dTM}{TM} = -\frac{d\alpha_w}{\alpha_w} \quad 5.3$$

or the uncertainty in mass m is equal to minus the uncertainty in α_w . Now, the uncertainty in α_w over time and space is made up of two parts: the uncertainty in the background alpha and the uncertainty in knowledge of the mass extinction efficiency associated with a smoke aerosol α_s . The best estimate of dry α_s is $4.5 \pm 0.5 \text{ m}^2/\text{gm}$, while wet $\alpha_{s,w}$ varies with varying RH and $f_s(\text{RH})$ conditions. The uncertainty in the background alpha could be estimated by propagating the uncertainty in the alpha of each of the aerosol components that make up the combined average alpha along with the variability in alpha of the hygroscopic species associated with variability in humidity. However, as discussed above, it is assumed that the standard deviation of the estimated extinction to mass ratio is a measure of the uncertainty in the knowledge of the average true background alpha due to variability in aerosol mixture.

Now,

$$\alpha_{mix,w} = \frac{1}{TM_d} (\alpha_{s,w} TM_s + \alpha_{bg,w} TM_{bg}) \quad 5.4$$

where $\alpha_{mix,w}$ is the mixture of background aerosols and smoke and $\alpha_{s,w}$ and $\alpha_{bg,w}$ are the wet smoke and background mass extinction efficiencies, respectively. Since $\alpha_w = \alpha_d f(\text{RH})$,

$$\frac{d\alpha_w}{\alpha_w} = -\frac{TM_s (d\alpha_{s,d} f_s(\text{RH}) + \alpha_{s,d} df_s(\text{RH}))}{TM_d \alpha_w} - \frac{TM_{bg} (d\alpha_{bg,d} f_{bg}(\text{RH}) + \alpha_{bg,d} df_{bg}(\text{RH}))}{TM_d \alpha_w} \quad 5.5$$

where TM_s , TM_{bg} , and TM_d are the dry or true mass of smoke, background, and smoke plus background, respectively. $d\alpha_{s,d}$ and $d\alpha_{bg,d}$ are the variability in α due to inherent uncertainty in alpha, and in the case of background alpha, its variability due to varying aerosol mix over time and space. $df_s(\text{RH})$ and $df_{bg}(\text{RH})$ are the variability in smoke and background $f(\text{RH})$ values, respectively, resulting from varying RH over time but primarily associated with diurnal variability in RH.

Because RH is measured at only a few IMPROVE sites, equation 5.5 cannot be evaluated at each site. Therefore, one site in the East, Great Smoky Mountains, and one site in the West, Grand Canyon, where continuous RH measurements are made at the IMPROVE sites, will be used as examples. These sites will be used to represent the eastern and western United States. The variables $d\alpha$ and $d(\text{RH})$ will be represented by one standard deviation of α and $f(\text{RH})$ values. At Great Smoky Mountains National Park, the $d(\text{RH})$ term, as represented by the standard deviation of $f(\text{RH})$, is approximately equal to 4 for all $\text{RH} < 95\%$ but only at 1.9 for $\text{RH} < 90\%$. At Grand

Canyon it is 2.67 and 1.65 for RH < 95% and 90%, respectively. The difference between the RH = 95 and 90% cutoff is presented to highlight the extreme nonlinearity in the f(RH) correction at high RH levels.

Because the hygroscopicity of a smoke aerosol is primarily dependent on the hygroscopic minerals mixed with the smoke particle organic matter, the f(RH) values for smoke were estimated assuming an ammonium sulfate growth curve as a function of RH but normalized such that the f(RH) value for smoke was equal to 1.3 at RH = 80% as discussed above. The best-estimate dry α for smoke is $4.5 \pm 1.0 \text{ m}^2/\text{gm}$, while for a wet α it increases to 5.3 ± 1.2 and $6.3 \pm 1.39 \text{ m}^2/\text{gm}$ in the West and East, respectively. In the East the difference between wet and dry efficiencies is near 30%. In the west the mass extinction efficiencies for smoke are substantially greater than the background aerosol mix, while they are similar to the background aerosol mix in the East.

The yearly average f(RH), wet and dry mass extinction efficiencies for background and smoke aerosols along with one standard deviation of the mean are summarized in Table 5.1.

The above analysis assumes that the f(RH) values of the hygroscopic species are known exactly. Of course, in reality there can be a substantial variability or uncertainty in the f(RH) factor in and of itself. It has been the subject of a number of papers but should be significantly less than the inherent variability in any f(RH) value over time and space.

Table 5.1: Value of f(RH) and mass extinction efficiencies used to estimate total uncertainty or variability of mass extinction efficiency of background plus smoke aerosol mix.

	West	CNST (West)	East	CNST (East)
f(RH) Background	2.67±2.67		4.64±4.0	
f(RH) Smoke	1.2±0.32		1.44±0.48	
α Background,dry	2.1±1.36	1863	2.59±1.20	1510
α Background,wet	3.0±1.45	1304	5.29±1.32	740
α Smoke,dry	4.5±1.0	869	4.5±1.0	869
α Smoke,wet	5.3±1.2	738	6.3±1.39	621

Figure 5.1 is a plot of the absolute value of the first plus third term (smoke plus background α variability/uncertainty) in equation 1.86 for each of the IMPROVE monitoring sites for the 1–3 hr health breakpoints listed in the legend of Figure 5.1. This corresponds to the average uncertainty or variability in background plus smoke mass extinction efficiencies other than the effects of variable f(RH). It includes the inherent uncertainty of α and the variability of α due to changing aerosol mix.

For the $38 \mu\text{g}/\text{m}^3$ breakpoint, the uncertainty in mass estimate varies from about 23% to 30%, while at higher mass concentrations, the uncertainty in mass estimates is dominated by the inherent uncertainty in smoke mass extinction efficiency, which was assumed to be $1.0 \text{ m}^2/\text{gm}$. That uncertainty is about 22%.

Background + Smoke Uncertainty in Alpha

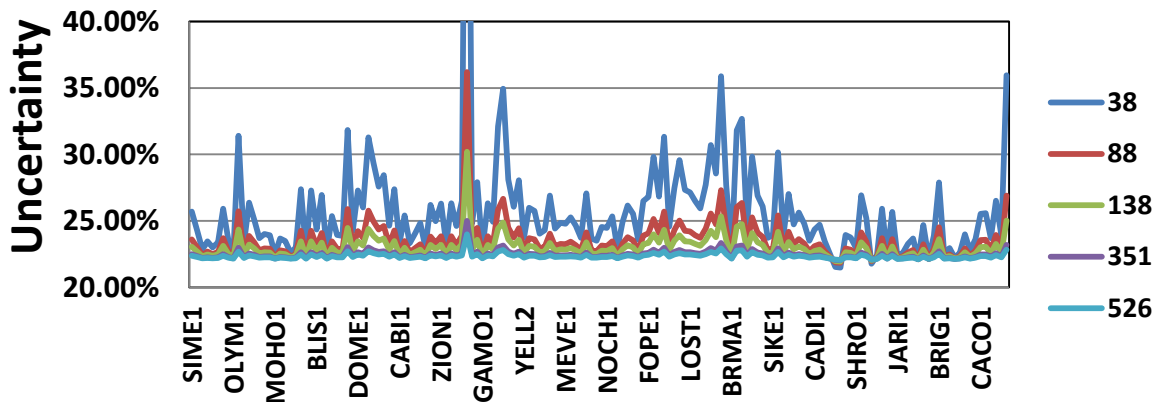


Figure 5.1: Average uncertainty in mass concentration resulting from the variability in mass extinction efficiencies.

Table 5.2 summarizes the uncertainties and variabilities associated with the four contributions to variability in mass extinction coefficients outlined in equation 1.86. The fractions in each cell are the estimated uncertainty in mass concentration from a V_r observation associated with the variable in column one. The first four rows are the four terms in equation 1.86 for an eastern and western situation. The first and second terms are the variability in background mass extinction efficiency due to uncertainty in mass extinction efficiencies of background aerosols and the inherent variability of the background aerosol mix, while the second term is associated with the variability of $f(RH)$ over time and aerosol mixture. The third and fourth terms are the same variables but for a smoke aerosol. The second and fourth columns, rows two and four, are the sum of $f(RH)$ and mass extinction uncertainties associated with the background and smoke aerosol for the western and eastern United States. The uncertainties associated with $f(RH)$ variability are large, in excess of 200% error for both the eastern and western United States. This large uncertainty was reflected in Figure 4.6 above in which the amount of water mass associated with a background eastern aerosol approached $70 \mu\text{g}/\text{m}^3$ at $RH = 90\%$. Next, because the total α_w uncertainty is dependent on the relative mix of background and smoke aerosol, rows 6–10 list the smoke plus background α_w uncertainty for the five health breakpoints listed in Figure 4.7. At $38 \mu\text{g}/\text{m}^3$, the uncertainty of a mass determination is 70% in the West and over 100% (factor of 2) in the East, just due to mass extinction variability primarily associated with variability of the $f(RH)$ factor. At smoke mass concentration levels that correspond to over $500 \mu\text{g}/\text{m}^3$, the mass uncertainties approach that of the uncertainty associated with smoke mass extinction characteristics, which are about 50% in the West and 57% in the East.

Table 5.2: Summary of the uncertainties in mass extinction efficiencies of smoke and background and smoke plus background for the western and eastern United States.

	Individual Uncertainty (West)	Combined Uncertainty (West)	Individual Uncertainty (East)	Combined Uncertainty (East)
Variability of α_w from uncertainty in α background and background aerosol mix	0.48		05.2	
Variability of α_w from variability in α background due to varying RH	1.87	2.35	1.96	2.21
Variability of α_w from uncertainty in α smoke	0.23		0.23	
Variability of α_w from variability in α smoke due to varying RH	0.27	0.50	0.34	0.57
Uncertainty of α (smoke plus background PM)				
38 ($\mu\text{g}/\text{m}^3$)		0.71		1.08
88 ($\mu\text{g}/\text{m}^3$)		0.59		0.79
138 ($\mu\text{g}/\text{m}^3$)		0.56		0.71
351 ($\mu\text{g}/\text{m}^3$)		0.52		0.63
526 ($\mu\text{g}/\text{m}^3$)		0.52		0.61
Uncertainty of α due to bias				
38 ($\mu\text{g}/\text{m}^3$)		0.25		0.05
88 ($\mu\text{g}/\text{m}^3$)		0.21		0.02
138 ($\mu\text{g}/\text{m}^3$)		0.20		0.01
351 ($\mu\text{g}/\text{m}^3$)		0.20		0.01
526 ($\mu\text{g}/\text{m}^3$)		0.19		0.00
Uncertainty of α from bias + α variability				
38 ($\mu\text{g}/\text{m}^3$)		0.96		1.14
88 ($\mu\text{g}/\text{m}^3$)		0.80		0.81
138 ($\mu\text{g}/\text{m}^3$)		0.76		0.73
351 ($\mu\text{g}/\text{m}^3$)		0.72		0.63
526 ($\mu\text{g}/\text{m}^3$)		0.71		0.61

The second type of uncertainty is associated with the difference between some assumed CNST in the $V_{rPM} = \text{CNST}$ relationship and the best estimate of CNST based on the literature review of mass extinction estimates of smoke and background aerosols. The implied CNST for the various wet and dry, background aerosol, and smoke mass extinction efficiencies are also listed in Table 5.1. If CNST is assumed to be 622 as suggested in the O'Neill et al. (2013) paper, then the implied constant alpha for all sites and all time is $6.3 \text{ m}^2/\text{gm}$. Therefore the bias uncertainty between the best estimate of alpha and $6.3 \text{ m}^2/\text{gm}$ can be calculated using

$$\text{Bias} = (6.3 - \alpha_w) / \alpha_w$$

$$5.6$$

where α_w is the mass extinction efficiency of the background plus smoke aerosol mix and will be unique to each site. For purposes of the calculation presented here it will only be approximated for the West and East because continuous RH measurements are not available at most IMPROVE sites. 6.3 is the implied α assuming CNST = 622. The second to last five rows in Table 5.2 summarize this bias uncertainty for the various mass breakpoints discussed above. In the western United States, this bias uncertainty is about 20%, reflecting the difference between 6.3 and the lower best-estimate smoke mass extinction efficiency. In the East the bias uncertainty is less than 5% because the best-estimate wet mass extinction efficiency of smoke was estimated to be 6.3 m²/gm, which corresponds to CNST = 622. The last five rows in Table 5.2 include both the bias and inherent mass extinction uncertainty. The total uncertainty varies from about a factor of 2 at 38 $\mu\text{g}/\text{m}^3$ to 60–70% under the highest mass concentrations.

The total variability or uncertainty in mass estimation is estimated using equation 5.7:

$$\frac{dm}{m} = \sqrt{\sum_i \left(\frac{dm}{m}\right)_i^2} \quad 5.7$$

where $\left(\frac{dm}{m}\right)_i$ are the individual uncertainties in mass determinations associated with $\gamma \neq 1$, non-black targets, perceptual uncertainty, and alpha.

Propagating the total variability or uncertainty in alpha (last five rows in Table 5.2) and those for a V_r observation (rows 1–3 in Table 5.3) according to equation 5.7, yields the overall uncertainty in making an atmospheric mass concentration estimate from a V_r observation. These estimations are presented in Table 5.3 in rows 6–10. In the West, the uncertainty at 38 $\mu\text{g}/\text{m}^3$ is about a factor of 2.1, while in the East it is about a factor of 2.3. Under higher mass loadings where it is the characteristics of the smoke aerosol that dominate, the uncertainty in both the East and West is about a factor of 2.0.

Table 5.3: Uncertainties in a mass estimated from a visual range observation associated with uncertainties in the visual range observation and in total mixed mass extinction efficiencies.

	Combined Uncertainty (West)	Combined Uncertainty (East)
Contrast threshold	0.20-0.30	0.20-0.30
Unknown C_o	0.15	0.15
Uneven illumination and dispersion	0.50	0.50
Total visual range judgment uncertainty (combination of previous three uncertainties)	0.58	0.58
Total uncertainty (alpha plus visual range uncertainty)		
38 ($\mu\text{g}/\text{m}^3$)	1.12	1.28
88($\mu\text{g}/\text{m}^3$)	0.99	1.00
138($\mu\text{g}/\text{m}^3$)	0.96	0.93
351($\mu\text{g}/\text{m}^3$)	0.92	0.86
526($\mu\text{g}/\text{m}^3$)	0.91	0.84

6. SUMMARY

Several state air quality agencies have developed policies to issue air quality index (AQI) warnings based on low values of visual range (V_r). AQI warnings are based on particulates (PM) resulting from fire smoke, often of 1–3 hr average concentrations. Because monitoring data are not available in all places where an AQI warning might potentially be given, states have used human-observed visual sightings (i.e., sighting distant targets to determine V_r) to estimate ambient particulate (PM) concentrations. Table 6.1 shows the V_r to PM relationship currently in “Wildfire Smoke, A Guide for Public Health Officials” (2008; herein referred to as “the smoke guide”), but other states and tribes have also adopted their own relationships. Concerns exist regarding the applicability of this methodology to humid environments, the applicability of this method to atmospheres that include significant levels of pollutants other than smoke, and potential errors in a human-sighted V_r .

Table 6.1. The “Wildfire Smoke, A Guide for Public Health Officials” linkage of air quality index categories with 1-hr, 8-hr and 24-hr $PM_{2.5}$ concentrations and visibility for arid conditions. The visibility scale is only linked with the 1–3 hr PM concentrations.

Air Quality Index Category	$PM_{2.5}$ or PM_{10} Levels ($\mu\text{g}/\text{m}^3$, 1–3 hr avg)	$PM_{2.5}$ or PM_{10} Levels ($\mu\text{g}/\text{m}^3$, 8 hr avg)	$PM_{2.5}$ or PM_{10} Levels ($\mu\text{g}/\text{m}^3$, 24 hr avg)	Visibility-Arid Conditions (miles)
Good	0-38	0-22	0-12	≥ 11
Moderate	39-88	23-50	12.1-35.4	6-10
Sensitive Groups	89-138	51-79	35.5-55.4	3-5
Unhealthy	139-351	80-200	55.5-150.4	1.5-2.75
Very Unhealthy	352-526	201-300	150.5-250.4	1-1.25
Hazardous	>526	>300	>250.5	<1

6.1 Background

The linkage between V_r and short-term (1–3 hr) PM concentrations in smoky conditions was originally created from a study performed in Helena, Montana, in the summer of 2000. The study used a tapered element oscillating microbalance (TEOM) to measure particle concentrations under smoky conditions associated with wildfire and reported V_r estimations derived from the Automated Surface Observing System (ASOS) at the Helena, Montana, airport.

The ASOS visibility monitoring system is calibrated to a fog-type aerosol and as such underestimates the V_r of a fine smoke aerosol by as much as a factor of 2. On the other hand, it measures only scattering when the observed V_r is sensitive to both atmospheric scattering and absorption. Typically, absorption is about 10% of total extinction; therefore, by neglecting absorption, V_r is overestimated by about 10%. Considering the calibration and absorption biases associated with an ASOS-type visibility measurement, the net effect is to significantly underestimate true V_r associated with a smoke-type aerosol. Furthermore, depending on the type of TEOM used, the measured mass can be significantly underestimated. Therefore in the $V_r * PM = CNST$ relationship derived from a combination of TEOM and ASOS measurements, the CNST value will likely be underestimated. The best-estimate mass scattering efficiency is 3.7

m^2/gm , corresponding to $\text{CNST} = 1057$. A curve fit between the two Montana measurements suggested that the V_r mass relationship is given by $V_r * \text{PM} = 450$ where V_r is expressed in miles. If V_r is expressed in km, then $V_r * \text{PM} = 724$. Both the TEOM and ASOS visibility measurement biases are addressed section 2 where mass measurement instrumentation is reviewed.

O'Neill et al. (2013) report on an analysis in which they developed the following relationship between V_r and PM using the IMPROVE aerosol species concentration database and the new Interagency Monitoring of Protected Visual Environments (IMPROVE) algorithm linking particle mass to particle extinction: $V_r^{0.98} \text{PM} = 622$. Here, V_r is expressed in km, and PM is particle concentration less than $2.5 \mu\text{m}$ and in units of $\mu\text{g}/\text{m}^3$. Their relationship is an average across IMPROVE monitoring sites in the arid Intermountain West and Great Plains, and they used the new IMPROVE equation for estimating extinction as a function of particulate mass concentrations.

The equation relating V_r to TM can be formulated in terms of fundamental physical and optical characteristics of an aerosol. Equation 2.37 states that

$$TM = \frac{3.912/\alpha_w}{V_r} - \frac{b_{sg}}{\alpha_w} \approx \frac{3.912/\alpha_w}{V_r} = \frac{\text{CNST}}{V_r} \quad 6.1$$

where $\text{CNST} = 3.912/\alpha_w$, α_w is the wet mass extinction coefficient of background plus smoke aerosol, and b_{sg} is clear air or Rayleigh scattering and is usually standardized to 10 Mm^{-1} . Any estimate of V_r includes the effects of coarse mass, so equation 6.1 is written in terms of total mass, TM, which is the sum of fine and coarse mass concentration. For purposes of this discussion, clear air scattering in equation 6.1 will be ignored in that its contribution to the correction of mass estimation from a V_r observation is only about 6% for the first health cutpoint of $38 \mu\text{g}/\text{m}^3$ and less for higher mass loadings. A CNST of 622 implies an average extinction to mass ratio α_w of $6.3 \text{ m}^2/\text{gm}$, while a CNST of 724 implies an α_w of $5.4 \text{ m}^2/\text{gm}$.

In equation 6.1 there are uncertainties in estimating V_r and inherent variability of α_w , resulting in significant uncertainty in obtaining an accurate mass concentration estimate from a V_r observation. Furthermore, the variability in background aerosol mixture and ambient meteorological conditions, primarily RH, over time and space brings into question the validity of using a simple one-stop-fits-all approach to estimating TM from a V_r observation.

6.2 Uncertainties in Estimating Visual Range

There are five uncertainties that come into play when trying to estimate V_r :

1. Judging when a target or landscape feature has reached the contrast that defines the V_r
2. Variability in inherent contrast of any given target.
3. Influence of nonuniform distribution of aerosol mass and nonuniform lighting conditions resulting in violation of the Koschmieder assumptions, i.e., the sky radiance at the target and observer are equal.

4. Perhaps even a greater uncertainty in a V_r estimate than the three issues listed above is that there will rarely be a target or landscape feature exactly at the V_r . Therefore estimating V_r from targets that are at a contrast greater than the threshold or have disappeared introduces a V_r estimate that would have an uncertainty far greater than those associated with the three issues discussed above. This type of uncertainty could lead to errors in a mass concentration estimate that could easily be hundreds of percent in error.
5. Uncertainties in assumed mass scattering and extinction efficiencies.

6.2.1 Uncertainty in Estimated Mass Concentration Due to Judging When the Target Is at a Threshold Contrast

It was shown that the uncertainty in estimated mass concentration is related to the ability of an observer to judge when the contrast has reached the threshold contrast or the contrast below which an observer cannot not detect a landscape feature a certain percentage of the time. To a first-order approximation, dm/m is proportional to k , the Weber constant that defines the contrast change that can be perceived as a function of contrast. It literally is the fractional change in contrast that is perceptible. dm/m is related to k by

$$\frac{dm}{m} = - \frac{\frac{dV_r}{V_r}}{1 - \frac{V_r b_{sg}}{3.912}} = - \frac{k}{3.912 - V_r b_{sg}} \quad 6.2$$

This equation shows that dm/m is a function V_r , and at the first health cutpoint of $38 \mu\text{g}/\text{m}^3$, dm/m is about 30% and approaches 20% for higher atmospheric mass concentrations. It is emphasized that this calculation was done assuming that the observer is trained and that for a casual observer the uncertainty could approach well over 75%.

6.2.2 Uncertainty in Estimated Mass Concentration Due to Unknown Inherent Contrast

The following equation relates uncertainty in mass estimate to uncertainty in knowledge of inherent contrast C_o . For tree-covered landscape features in direct sunlight, dC_o/C_o will be on the order of 50%, relative to the assumption that the target is black. If the target landscape feature is rocky or a grass-covered meadow, the uncertainty of C_o can be much greater.

$$\frac{dm}{m} = \frac{\frac{dC_o}{C_o}}{3.912 - V_r b_{sg}} \quad 6.3$$

For a best-case scenario where the target is a tree-covered landscape feature, the uncertainty in a mass estimate is on the order of 15–20% for $38 \mu\text{g}/\text{m}^3$ and about 15% for higher mass concentrations.

6.2.3 Uncertainty in Estimated Mass Concentration Due to Nonuniform Lighting Conditions and Aerosol Mass Spatial Distribution

Nonuniform distribution of aerosol loadings between the observer and target landscape feature can result from uneven dispersion of aerosols such as smoke or merely result from viewing the landscape feature at some angle other than horizontal. The result is that the ratio of sky radiance

at the observer to that at the landscape feature, $\gamma = {}_sN_o/{}_sN_r$, is different from one. $\gamma \neq 1$ can also result from nonuniform lighting conditions. dm/m is related to the uncertainty in γ by

$$\frac{dm}{m} = \frac{\frac{d\gamma}{\gamma}}{3.912 + \ln(\gamma)} \quad 6.4$$

For any PM value, the uncertainty is about half the PM level, which corresponds to an overall uncertainty of approximately 50%, independent of V_r or PM level. Of course, for different observer sun angle and landscape geometries, the uncertainty will vary. The uncertainty could be considerably greater, and under more ideal conditions than those assumed here, it could be less. However, for purposes of this report, the uncertainty in estimated ambient mass concentration due to nonuniform lighting and mass concentration distribution estimated from an observed V_r will be assumed to be about 50%.

Assuming that the combined error can be estimated by

$$\frac{dm}{m} = \sqrt{\sum_i \left(\frac{dm}{m}\right)_i^2} \quad 6.5$$

where $\left(\frac{dm}{m}\right)_i$ are the individual uncertainties in mass determinations associated with $\gamma \neq 1$, non-black targets, and perceptual uncertainty. The combined uncertainty in mass determination associated with uncertainty in judged V_r is approximately 60%. These uncertainties in judged V_r are summarized in the first four rows of Table 6.1. It is emphasized that there are many assumptions in this estimate of uncertainty, but most are conservative and the uncertainty could be much greater than 60%.

6.3 Uncertainties in an Assumed Wet Mass Extinction Efficiency α_w

In an analysis of the IMPROVE data, Malm and Hand (2007) found that inorganic and organic species have a mass-dependent mass scattering efficiency, and this dependence was integrated into the new IMPROVE algorithm in which the POM mass scattering efficiency was scaled between 2.8 and 6.1 m^2/gm for POM mass concentrations between 0.0 and 20.0 $\mu g/m^3$. It was hypothesized that the higher particle mass concentrations were associated with an aged aerosol that was more mono-dispersed in a size range that is more conducive to efficient light scattering.

O'Neill et al. (2013) applied this algorithm in an attempt to estimate a relationship between observed V_r and smoke mass concentration. In the way they applied the equation, they ignored smoke absorption and implicitly assumed that smoke was aged and had the higher mass scattering coefficient used in the new IMPROVE algorithm. However, the POM mass concentrations associated with wildfire and prescribed fire may be associated with high mass loadings that are not necessarily aged. In fact, the highest mass loadings are usually associated with a direct impact of a smoke plume. Therefore it should not be assumed, and would likely be erroneous, to link the higher mass scattering efficiencies used in the new IMPROVE algorithm to those found in an aerosol containing high levels of smoke particulate.

The use of the new IMPROVE algorithm in the O'Neill et al. (2013) analysis resulted in an implied dry smoke aerosol mass scattering efficiency of $6.3 \text{ m}^2/\text{gm}$ in both the eastern and western United States. In the review of literature on smoke aerosol optical properties, an average best-estimate of a smoke aerosol mass scattering efficiency is on the order of $3.4\text{--}4.0 \text{ m}^2/\text{gm}$, and the Hand and Malm (2007) general review of mass scattering efficiencies recommended a value of $3.7 \text{ m}^2/\text{gm}$ for background POM. Both these values are substantially lower than the mass scattering efficiency implied by the O'Neill et al. (2013) analysis. The best estimate of dry mass extinction efficiency (includes the extinction due to absorption) for smoke is $4.5 \text{ m}^2/\text{gm}$.

Furthermore, in the analysis carried out in this report, it was found that actual average background wet mass scattering values of less than $2 \text{ m}^2/\text{gm}$ were found in the Intermountain West and were over $5 \text{ m}^2/\text{gm}$ in the eastern and northwestern United States. The higher mass scattering efficiencies are due to absorbed water on hygroscopic aerosol species, not an inflated mass scattering efficiency associated with an aged smoke aerosol.

Including the absorption of water by a smoke aerosol will serve to further increase its mass extinction efficiency. The literature suggests that for a smoke aerosol, $f(\text{RH}) \approx 1.3$ at $\text{RH} = 80\%$. The growth of organic smoke particles as a function of RH is primarily due to the presence of hygroscopic salts mixed in with the organic aerosol. Therefore an ammonium sulfate $f(\text{RH})$ curve was normalized to $f(\text{RH}) = 1.3$ at $\text{RH} = 80\%$ and was incorporated into an average extinction efficiency for western and eastern smoke extinction efficiencies. The wet mass extinction efficiency for smoke is 5.3 ± 1.2 and $6.3 \pm 1.39 \text{ m}^2/\text{gm}$ for the western and eastern United States, respectively. That means that on the average the mass of a smoke aerosol will have about 20% water content in the West and almost 40% water content in the East. It was shown that a one sigma (one standard deviation) variability of mass due to RH variability is about 27% in the West and 34% in the East!

The overall uncertainty in the wet mass extinction efficiency (resulting from a mixture of background aerosol and smoke) over time and space is made up of the uncertainty in the background mass extinction efficiency and the uncertainty in knowledge of the mass extinction efficiency associated with a smoke aerosol. The uncertainty in the background mass extinction efficiency could be estimated by propagating the uncertainty in the mass extinction efficiency of each of the aerosol components that make up the combined average mass extinction efficiency, along with the variability in mass scattering efficiency of the hygroscopic species associated with variability in humidity. However, it is assumed that the standard deviation of the measured or estimated extinction to mass ratio of the background aerosol is a measure of the uncertainty in the knowledge of background mass extinction efficiency, due to the variability of mass extinction efficiency resulting from a varying mixture of particle species over time. The variability in 24-hr average mass scattering efficiency varies from a low near one up to a maximum near two. The higher variability is found for those sites where RH is higher, such as the eastern and northwestern monitoring locations. It is emphasized that the above discussion does not address the short-term, diurnal variability associated with varying $f(\text{RH})$.

For the $38 \text{ }\mu\text{g}/\text{m}^3$ breakpoint, the uncertainty in mass estimate associated with just the variability in 24-hr average background mass extinction efficiency varies from about 23% to 30%, while at higher mass concentrations, the uncertainty in mass estimates is dominated by the uncertainty in

smoke mass extinction efficiency, which was assumed to be $1.0 \text{ m}^2/\text{gm}$. That uncertainty is about 22%. Additional uncertainty is associated with making estimates of mass concentration on shorter timescales, which is implicitly required when making a V_r observation that is essentially instantaneous. Then the uncertainty in $f(\text{RH})$ plays a significant role. The uncertainty in mass concentration estimation resulting from the uncertainty in $f(\text{RH})$ for a background aerosol will be at least on the order of 200% in both the East and Intermountain West. For higher mass loadings, it will be the hygroscopicity of the smoke aerosol that dominates the $f(\text{RH})$ -related mass uncertainty.

The above discussion pertains to the variability of estimated mass associated only with the variability of mass extinction efficiency around some mean mass extinction efficiency that is different for every monitoring site. Another important uncertainty associated with using one V_r PM relationship is that it assumes a constant mass extinction efficiency for all sites and for all times. If CNST were chosen based on the best estimate of a dry smoke extinction to mass ratio of $4.5 \text{ m}^2/\text{gm}$, then the V_r mass relationship would be $V_r\text{PM} = 870$. In general, on the average this would yield an underestimate of mass in the Intermountain West and would be about right in the East. The O'Neill value of $\text{CNST} = 622$ implicitly assumes a mass extinction efficiency of $6.3 \text{ m}^2/\text{gm}$.

For the $\text{CNST} = 622$ assumption, it was shown that the uncertainty in mass estimates just due to assuming one CNST for all time and space is about 20–25% in the West and less than 5% in the East. The 20–25% bias in the West is associated with an overestimate of mass. The total variability or uncertainty in mass extinction efficiency for the various health breakpoints is summarized in rows 6–10 in Table 6.2.

6.4 Quantifying Total Uncertainty

Propagating the total variability or uncertainty in mass extinction efficiency (rows 6–10 in Table 6.2) and those for a V_r observation (rows 1–4 in Table 6.2) according to equation 6.5, yields the overall uncertainty in making an atmospheric mass concentration estimate from a V_r observation. In the West, the uncertainty at $38 \mu\text{g}/\text{m}^3$ is about a factor of 2.1, while in the East, it is about a factor of 2.3. **Under higher mass loadings where it is the characteristics of the smoke aerosol that dominate, the uncertainty in both the East and West is about a factor of 2.0.**

Table 6.2: Uncertainties in a mass estimated from a visual range observation associated with uncertainties in the visual range observation and in total mixed mass extinction efficiencies.

	Combined Uncertainty (West)	Combined Uncertainty (East)
Contrast threshold	0.20-0.30	0.20-0.30
Unknown C_o	0.15	0.15
Uneven illumination and dispersion	0.50	0.50
Total visual range judgment uncertainty (combination of previous three uncertainties)	0.58	0.58
Uncertainty of α_w from bias + α variability		
38 ($\mu\text{g}/\text{m}^3$)	0.96	1.14
88 ($\mu\text{g}/\text{m}^3$)	0.80	0.81
138 ($\mu\text{g}/\text{m}^3$)	0.76	0.73

	Combined Uncertainty (West)	Combined Uncertainty (East)
351 ($\mu\text{g}/\text{m}^3$)	0.72	0.63
526 ($\mu\text{g}/\text{m}^3$)	0.71	0.61
Total uncertainty (mass extinction efficiency plus visual range uncertainty)		
38 ($\mu\text{g}/\text{m}^3$)	1.12	1.28
88 ($\mu\text{g}/\text{m}^3$)	0.99	1.00
138 ($\mu\text{g}/\text{m}^3$)	0.96	0.93
351 ($\mu\text{g}/\text{m}^3$)	0.92	0.86
526 ($\mu\text{g}/\text{m}^3$)	0.91	0.84

6.5 V_r * PM = CNST Relationships

Any V_r observation will include the effects of water on the aerosol, background particles including coarse mass, and smoke. Therefore the implied mass associated with a $V_r\text{PM} = \text{CNST}$ relationship includes all aerosols in the atmosphere. However, at higher mass concentrations, it is the physical and optical characteristics of smoke that will dominate the $V_r\text{PM}$ relationship. Therefore, the choice of CNST should reflect the extinction to mass ratio characteristics of a smoke aerosol. A literature review of the optical properties of smoke suggests a dry extinction to mass ratio of $4.5 \pm 1.0 \text{ m}^2/\text{gm}$ (CNST = 870) and a variable wet extinction to mass ratio depending on the variability of ambient RH levels. In the Intermountain West, the wet extinction to mass ratio would be around $5.3 \text{ m}^2/\text{gm}$ (CNST = 738), while in the East it would be about $6.3 \text{ m}^2/\text{gm}$ (CNST = 621). The higher wet extinction to mass ratios reflect about an average 18% water content of the smoke aerosol in the Intermountain West and about 40% in the East.

Furthermore, the uncertainty in making a V_r observation plus the uncertainty and variability in extinction to mass ratios results in a one standard deviation uncertainty in mass estimation of more than a factor of 2. That is, any mass determination may be at least a factor of 2 high or a factor of 2 low.

An issuance of an AQI warning should reflect the possibility that the mass determination may underestimate the true mass by at least a factor of 2. Even if a CNST is chosen such that it is a factor of 2 greater than the best estimate of CNST, 16% of the time the true mass will be even greater than estimated mass. Or stated in another way, 84% of the time, true mass will be less than the upper bound estimated mass.

Tables 6.3a and 6.3b summarize the smoke guide's 1–3 hr health break points for the West and the East, their upper and lower one-standard-deviation uncertainty bounds, the smoke guide's recommended V_r associated with each health breakpoint, the best-estimate V_r for each breakpoint under dry conditions (RH <30%, CNST = 870), the best-estimate V_r for average RH conditions (CNST = 738 and 621 for the West and East, respectively), and the recommended V_r such that only 16% of the V_r observations will result in an estimated mass that is greater than true mass (CNST = 870 and 620 for the West and East, respectively).

Table 6.3a: (West) The smoke guide’s (“Wildfire Smoke, A Guide for Public Health Officials”, 2008) mass concentration breakpoints listed along with the percent uncertainty associated with estimating the mass breakpoints from a visual range observation. Also listed are the upper and lower bounds associated with each mass breakpoint estimate. Best-estimate dry and ambient visual ranges corresponding to the mass breakpoints as well as the recommended visual range levels are listed.

Guide Breakpoint ($\mu\text{g}/\text{m}^3$)	Percent Uncertainty (West)	Upper Bound ($\mu\text{g}/\text{m}^3$) (West)	Lower Bound ($\mu\text{g}/\text{m}^3$) (West)	Guide V_r (Km)	Best-Estimate V_r (Km) (Dry)	Best-Estimate V_r (Km) (Wet-West)	Recommendation V_r (Km)
38	112	81	18	17.7	22.9	19.4	41.2
88	99	175	44	9.7	9.9	8.4	17.8
138	96	270	70	4.8	6.3	5.4	11.3
351	92	674	183	2.4	2.5	2.1	4.5
526	91	1005	275	1.6	1.7	1.4	3.0

Table 6.3b: (East) The smoke guide’s (“Wildfire Smoke, A Guide for Public Health Officials”, 2008) mass concentration breakpoints are listed along with the percent uncertainty associated with estimating the mass breakpoints from a visual range observation. Also listed are the upper and lower bounds associated with each mass breakpoint estimate. Best-estimate dry and ambient visual ranges corresponding to the mass breakpoints as well as the recommended visual range levels are listed.

Guide Breakpoint ($\mu\text{g}/\text{m}^3$)	Percent Uncertainty (East)	Upper Bound ($\mu\text{g}/\text{m}^3$) (East)	Lower Bound ($\mu\text{g}/\text{m}^3$) (East)	Guide V_r (Km)	Best-Estimate V_r (Km) (Dry)	Best-Estimate V_r (Km) (Wet-East)	Recommendation V_r (Km)
38	128	87	17	17.7	22.9	16.3	37.3
88	100	176	44	9.7	9.9	7.1	16.1
138	93	266	72	4.8	6.3	4.5	10.3
351	86	653	189	2.4	2.5	1.8	4.0
526	84	968	286	1.6	1.7	1.2	2.7

Figures 6.1 to 6.3 are plots of the data in Table 6.3a. Figure 6.1 is a plot of the 1–3 hr concentration breakpoints from the smoke guide as a function of V_r from the smoke guide and as a function of the corresponding best-estimate V_r for dry and for wet or ambient conditions. The dry best-estimate V_r is always greater than the smoke guide’s V_r by about 30% for the 38 and 138 $\mu\text{g}/\text{m}^3$ breakpoints and only a few percent for the remaining breakpoints. The best-estimate V_r for ambient conditions is about 10% greater for the 38 and 138 $\mu\text{g}/\text{m}^3$ breakpoints and about 10% less for the remaining breakpoints. **What this plot highlights is that there is not a consistent physical relationship between the visual ranges and concentration breakpoints listed in the smoke guide.**

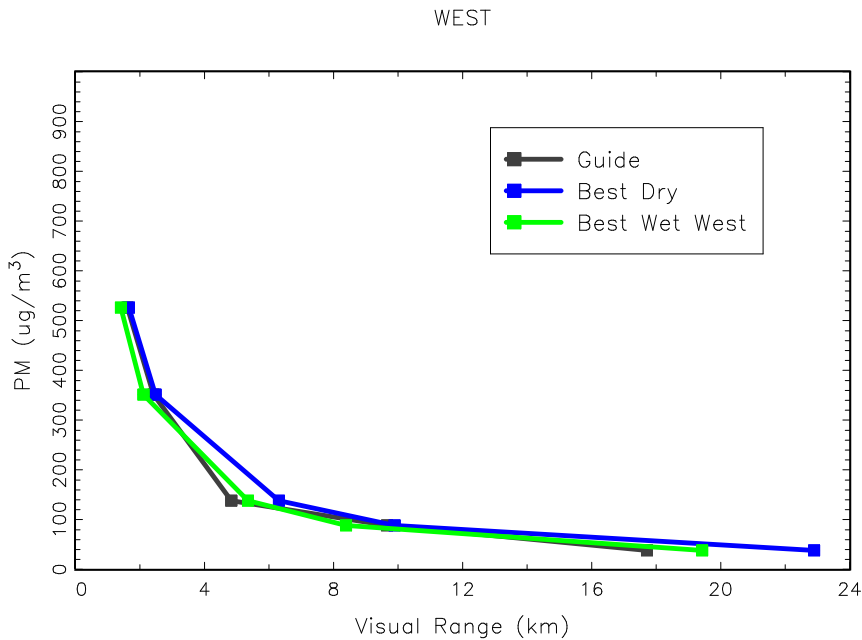


Figure 6.1: Plot of PM vs. visual range from the smoke guide's ("Wildfire Smoke, A Guide for Public Health Officials", 2008) best dry and ambient (wet) estimate PM vs. visual range relationships for the West.

Figure 6.2 is a plot of the recommended V_r corresponding to the concentration breakpoints as well as the best-estimate and smoke guide V_r , along with the uncertainty bars showing the one standard deviation uncertainty associated with each mass estimate. First of all, notice that the recommended V_r to mass breakpoint relationship corresponds to the one standard deviation uncertainty of either the smoke guide or best-estimate V_r values. **Choosing the recommended V_r to mass concentration relationship would yield mass estimates derived from V_r observations that would not be higher than true mass concentrations 16% of the time.** The second point to be made is that, within the uncertainty limits, the mass estimates from V_r observations associated with the first three breakpoints (V_r greater than approximately 5 km) are essentially indistinguishable, as are the mass estimates associated with the lowest two V_r observations (V_r less than approximately 5 km).

WEST

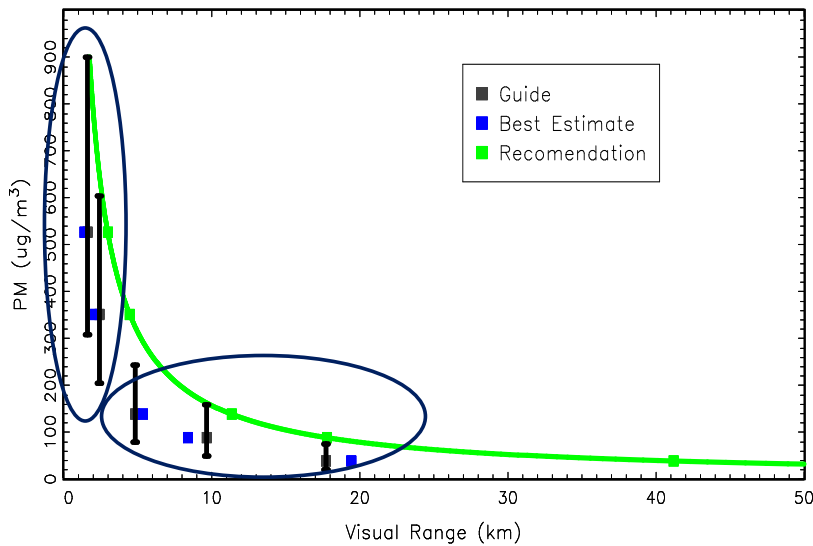


Figure 6.2: Plot of the smoke guide's ("Wildfire Smoke, A Guide for Public Health Officials", 2008) PM vs. visual range relationship as well as the uncertainty in the PM estimate derived from a visual range observation. The Best Estimate visual range values are for ambient conditions, taking into account relative humidity. Also plotted are the recommended visual ranges that are to be associated with the mass concentration breakpoint.

Figure 6.3 is a plot of the same data as in Figure 6.2 but on a log-log scale. Because a percent change in mass corresponds to some percent change in V_r , there is linear relationship between the $\log(V_r)$ and $\log(\text{Mass})$. This graph clearly shows that on a percent basis, the uncertainties under low V_r and high mass loadings are about the same as under lower mass loadings and greater V_r . This plot further highlights the inconsistent relationship between V_r and mass concentrations associated with the mass concentration breakpoints listed in the smoke guide. If there were a consistent relationship between PM and V_r , the smoke guide's PM- V_r would be a straight line.

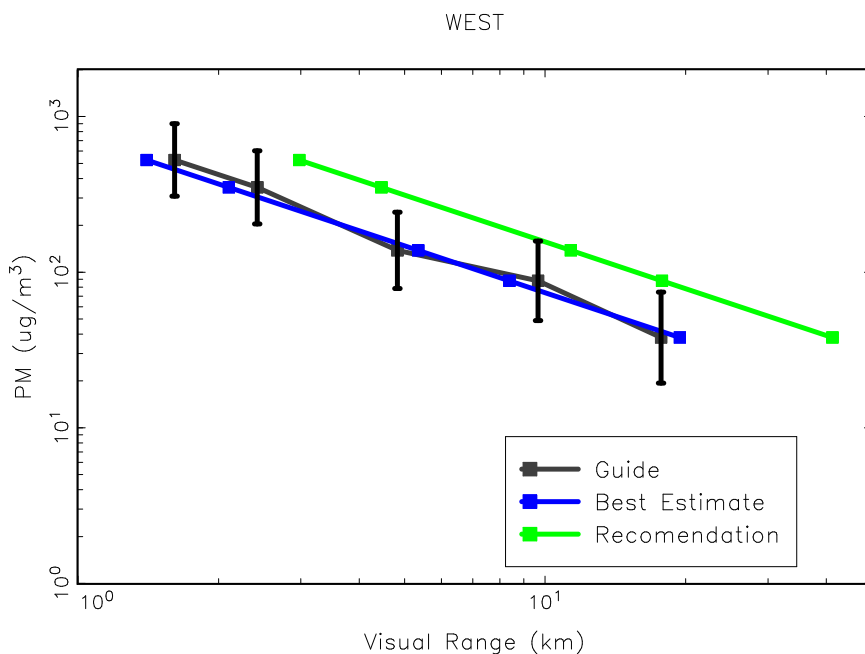


Figure 6.3: Log-log plot of the smoke guide’s (“Wildfire Smoke, A Guide for Public Health Officials”, 2008) PM vs. visual range relationship as well as the uncertainty in the PM estimate derived from a visual range observation. Also plotted are the recommended visual ranges that are to be associated with the mass concentration breakpoint.

Figure 6.4 is the same plot as Figure 6.1 but for the East. The smoke guide and best dry curves are the same as in Figure 6.1; however, because of higher humidity conditions, the best ambient or wet curve is quite different from the Intermountain West case shown in Figure 6.1. In the West, the ambient best-estimate curve was within about 10% of the smoke guide recommendations, while in the East, the smoke guide V_r associated with the mass breakpoints are about 30% greater than those recommended. Because of higher humidity, a lower V_r is required to achieve the same dry mass concentration level.

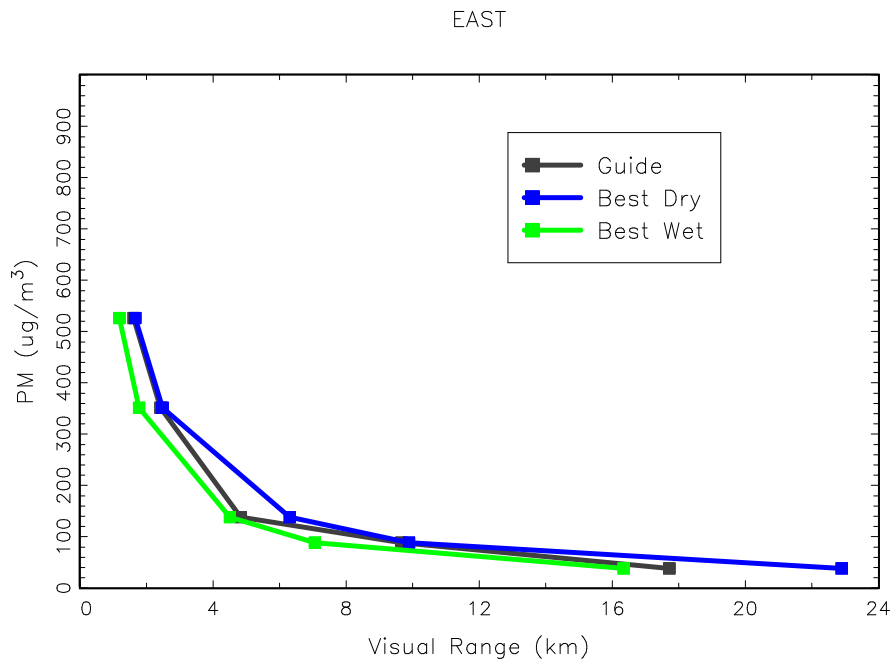


Figure 6.4: Plot of PM vs. visual range from the smoke guide’s (“Wildfire Smoke, A Guide for Public Health Officials”, 2008) best dry and ambient (wet) estimate, PM vs. visual range relationships for the East.

6.6 Pictorial Examples of Visual Impairment Associated with the Health Breakpoint Mass Concentrations

Examples of the visual impairment associated with the health breakpoint mass concentrations along with their associated uncertainty, listed in Table 6.3a, are shown in Figures 6.5 to 6.8 for a nonurban and urban scene. Figure 6.5 is a view of Desert View from Hopi Point, Grand Canyon. Distances to various landscape features are shown in the photo. Figure 6.7 shows a view of downtown Dallas, Texas, and again, distances to various features are indicated.

The center column (column 2) of pictures in Figure 6.6 shows the appearance of the Grand Canyon scene as it would appear in an atmosphere where the ambient mass concentration corresponded to the V_r listed for the first four health breakpoints presented in Table 6.3a. Columns 1 and 3 show pictures corresponding to the upper and lower uncertainty/variability V_r bounds for each of the V_r health breakpoints. Therefore, the first row shows the variability of the appearance of the scene for a true mass concentration of $38 \mu\text{g}/\text{m}^3$, the second row the variability in the appearance of the scene for a mass concentration of $88 \mu\text{g}/\text{m}^3$, and so forth. If the true mass concentration were $88 \mu\text{g}/\text{m}^3$, then the V_r could be anywhere between 4.9 and 19.2 km 68% of the time. This range of V_r as depicted in the pictures overlaps with the appearance of the scene that corresponds to the first and third ($38.0 \mu\text{g}/\text{m}^3$ and $138 \mu\text{g}/\text{m}^3$, respectively) health breakpoints. **In other words, the first three breakpoints are essentially indistinguishable from each other as are any combination of about three concurrent breakpoints.**

It is also clear from Figure 6.6 that it is necessary to have scenic elements at distances corresponding to the approximate V_r linked to the health breakpoints. Many scenes in more remote landscapes have distinct landscape features, but they tend to be at distances greater than a few kilometers, and in many cases they are tens of kilometers distant. In the Grand Canyon scene, mass concentrations above the second health breakpoint (moderate) are indistinguishable. Figure 6.8 shows the same series of photos for the urban scene of Dallas, Texas.

For more photos approximating an average appearance of a number of United States Forest Service and National Park Service vistas, the reader is directed to <http://www.frames.gov/partner-sites/emissions-and-smoke/perceptions/smoke-examples/> where the University of Idaho College of Natural Resources has developed the “Smoke Photographic Guides for Communicating Smoke Impacts.” The primary purpose of the guides is to serve as a tool for communicating potential particulate matter ($PM_{2.5}$) levels using visual representation. There are eight guides representing United States Forest Service regions 1–6, 8, and 9.

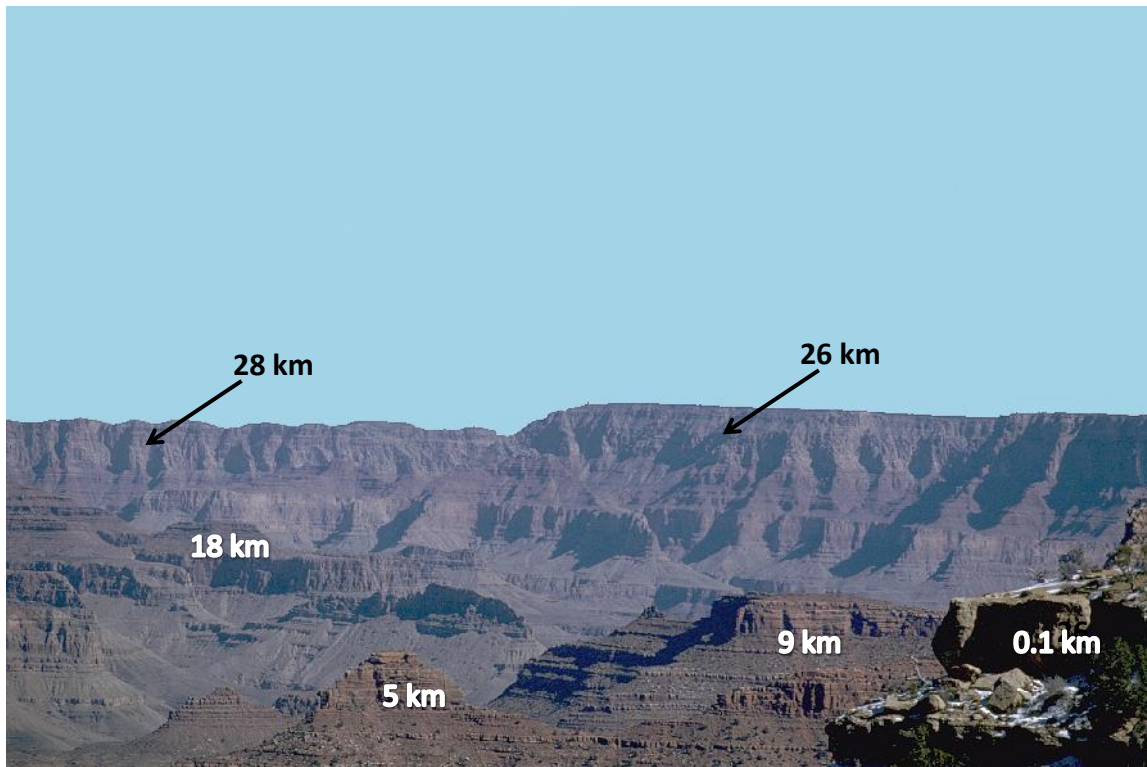


Figure 6.5: Desert View as seen from Hopi Point, Grand Canyon, Arizona. Distances to a number of landscape features are indicated.



Figure 6.6: The center column (column 2) shows the appearance of the Grand Canyon scene as it would appear in an atmosphere where the ambient mass concentration corresponded to the visual ranges listed for the first four health breakpoints. The first row shows one standard deviation variability of the appearance of the scene for a true mass concentration of $38 \mu\text{g}/\text{m}^3$, the second row the variability in the appearance of the scene for a mass concentration of $88 \mu\text{g}/\text{m}^3$, and so forth.

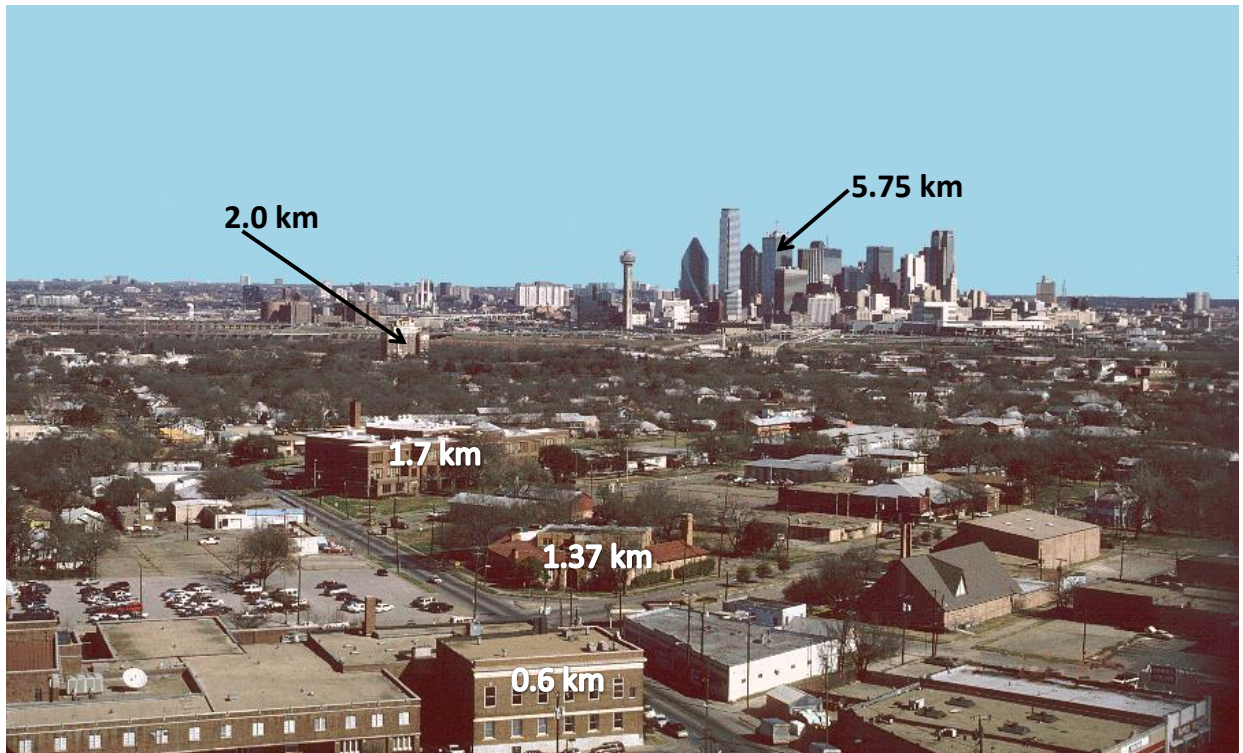


Figure 6.7: View of Dallas, Texas. Distances to a number of structures are indicated.

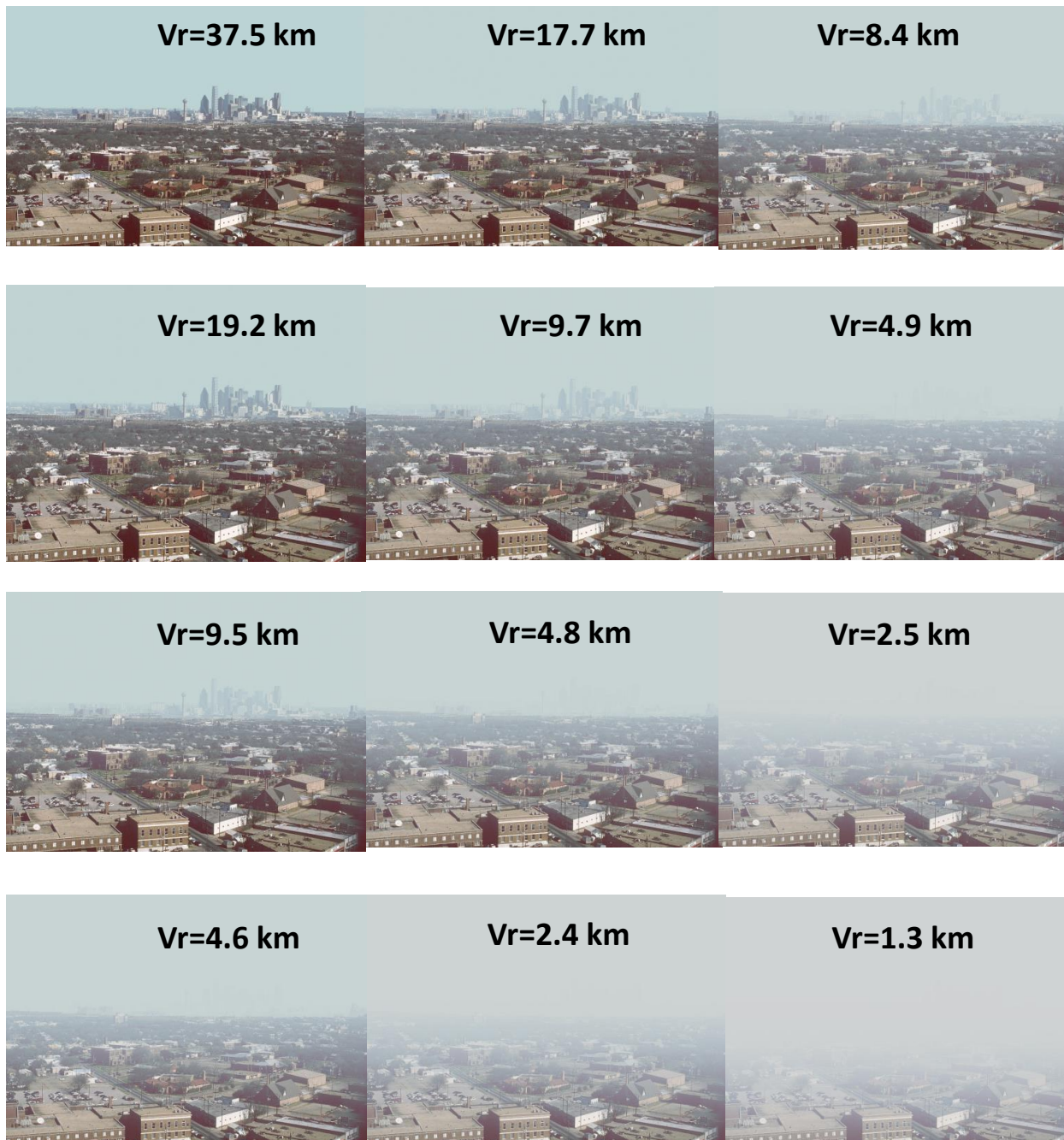


Figure 6.8: The center column (column 2) shows the appearance of the Dallas, Texas scene as it would appear in an atmosphere where the ambient mass concentration corresponded to the visual ranges listed for the first four health breakpoints. The first row shows one standard deviation variability of the appearance of the scene for a true mass concentration of $38 \mu\text{g}/\text{m}^3$, the second row the variability in the appearance of the scene for a mass concentration of $88 \mu\text{g}/\text{m}^3$, and so forth.

A second method of choosing a CNST that assures some confidence that the mass estimation is not underestimated is to choose a lower bound for the average mass extinction ratio and further

adjust the CNST value for an uncertainty in making a V_r estimation. A lower bound for α would be about $3.0 \text{ m}^2/\text{gm}$, corresponding to $\text{CNST} = 1304$. The uncertainty in making a V_r observation (Table 6.1 above) is about 0.58, corresponding to a $\text{dm} \approx 0.58 * 738 = 428$ and $0.58 * 621 = 360$ in the Intermountain West and the East, respectively. Therefore a second method at arriving at an average CNST value is to choose a conservative $\text{CNST} = 1304$ and add it to the associated error in CNST due to making a V_r observation: $\text{CNST} = 1304 + 428 = 1732$ for the Intermountain West and $\text{CNST} = 1304 + 360 = 1664$ for the East.

7. RECOMMENDATIONS

Quantification of Uncertainty – About a Factor of 2: Propagating the total one standard deviation variability or uncertainty in mass extinction efficiency and a V_r observation yields an overall one standard deviation uncertainty in making an atmospheric mass concentration estimate from a V_r observation. In the West, the uncertainty at $38 \text{ } \mu\text{g}/\text{m}^3$ is about a factor of 2.1, while in the East it is about a factor of 2.3. Under higher mass loadings where it is the characteristics of the smoke aerosol that dominate, the uncertainty in both the East and West is about a factor of 1.8 to 1.9. Therefore 16% of the time, the true mass concentration will be a factor of 2 greater than estimated mass. Or stated in another way, 84% of the time, true mass will be less than estimated mass.

Recommendation #1 – Use a conservative estimate of the $V_r * \text{PM} = \text{CNST}$ relationship to take into account the factor of 2 uncertainty, and customize it by location: Chose a $V_r * \text{PM} = \text{CNST}$ that reflects one standard deviation uncertainty in mass estimate from a V_r observation. This $V_r * \text{PM}$ relationship is referred to as the recommended relationship.

Tables 7.1 and 7.2 summarize for the West and East, respectively, the smoke guide’s 1–3 hr mass concentrations for the five health breakpoints, their upper and lower one standard deviation uncertainty bounds, the smoke guide’s recommended V_r associated with each health breakpoint, the best-estimate V_r for each breakpoint under dry conditions ($\text{RH} < 30\%$), the best-estimate V_r for average RH conditions, and the recommended V_r such that only 16% of the V_r observations will result in an estimated mass that is greater than true mass.

Table 7.1: (West) Smoke guide (“Wildfire Smoke, A Guide for Public Health Officials”, 2008) mass concentration breakpoints along with the percent uncertainty associated with estimating mass breakpoints from a visual range observation. Also listed are the upper and lower bounds associated with each mass breakpoint estimate. Best-estimate dry and ambient visual ranges corresponding to the mass breakpoints as well as the recommended visual range levels are listed.

Guide Breakpoints ($\mu\text{g}/\text{m}^3$)	Upper Bound ($\mu\text{g}/\text{m}^3$) (West)	Lower Bound ($\mu\text{g}/\text{m}^3$) (West)	Guide V_r (Km)	Best-Estimate V_r (Km) (Dry)	Best-Estimate V_r (Km) (Wet-West)	Recommendation V_r (Km)
38	81	18	17.7	22.9	19.4	41.2
88	175	44	9.7	9.9	8.4	17.8
138	270	70	4.8	6.3	5.4	11.3
351	674	183	2.4	2.5	2.1	4.5
526	1005	275	1.6	1.7	1.4	3.0

Table 7.2: (East) Smoke guide (“Wildfire Smoke, A Guide for Public Health Officials”, 2008) mass concentration breakpoints along with the percent uncertainty associated with estimating the mass breakpoints from a visual range observation. Also listed are the upper and lower bounds associated with each mass breakpoint estimate. Best-estimate dry and ambient visual ranges corresponding to the mass breakpoints as well as the recommended visual range levels are listed.

Guide Breakpoints ($\mu\text{g}/\text{m}^3$)	Upper Bound ($\mu\text{g}/\text{m}^3$) (East)	Lower Bound ($\mu\text{g}/\text{m}^3$) (East)	Guide V_r (Km)	Best-Estimate V_r (Km) (Dry)	Best-Estimate V_r (Km) (Wet-East)	Recommendation V_r (Km)
38	87	17	17.7	22.9	16.3	37.3
88	176	44	9.7	9.9	7.1	16.1
138	266	72	4.8	6.3	4.5	10.3
351	653	189	2.4	2.5	1.8	4.0
526	968	286	1.6	1.7	1.2	2.7

Figure 7.1 is a plot of the recommended V_r corresponding to the concentration breakpoints in green as well as the best-estimate and smoke guide V_r , along with the uncertainty bars showing the one standard deviation uncertainty associated with each mass estimate. First of all, notice that the recommended V_r to mass breakpoint relationship corresponds to the one standard deviation uncertainty of either the smoke guide or best-estimate V_r values. Choosing the recommended V_r to mass concentration relationship would yield mass estimates derived from V_r observations that would not be higher than true mass concentrations 16% of the time.

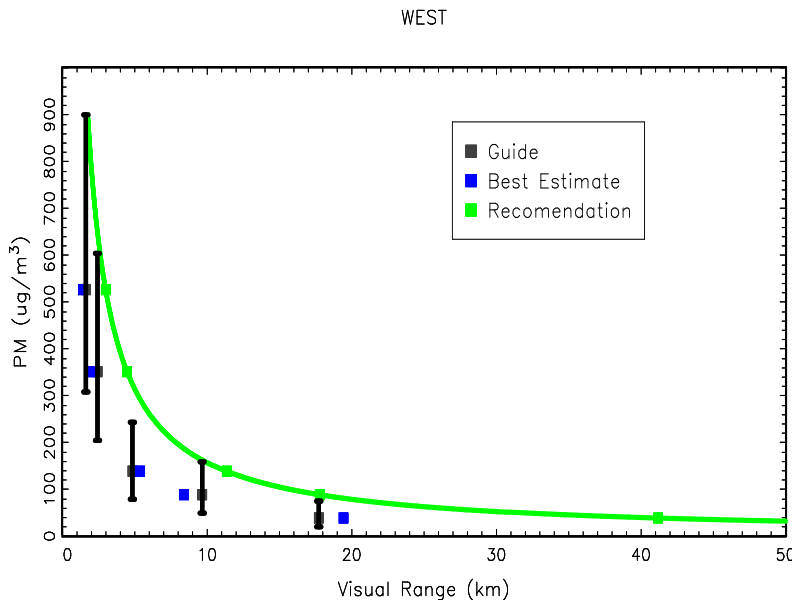


Figure 7.1: (West) Plot of the smoke guide’s (“Wildfire Smoke, A Guide for Public Health Officials”, 2008) PM vs. V_r relationship, as well as the uncertainty in the PM estimate derived from a visual range observation. Also plotted are the recommended visual ranges that are to be associated with the mass concentration breakpoint.

Figure 7.2 shows the same calculations but for the eastern United States.

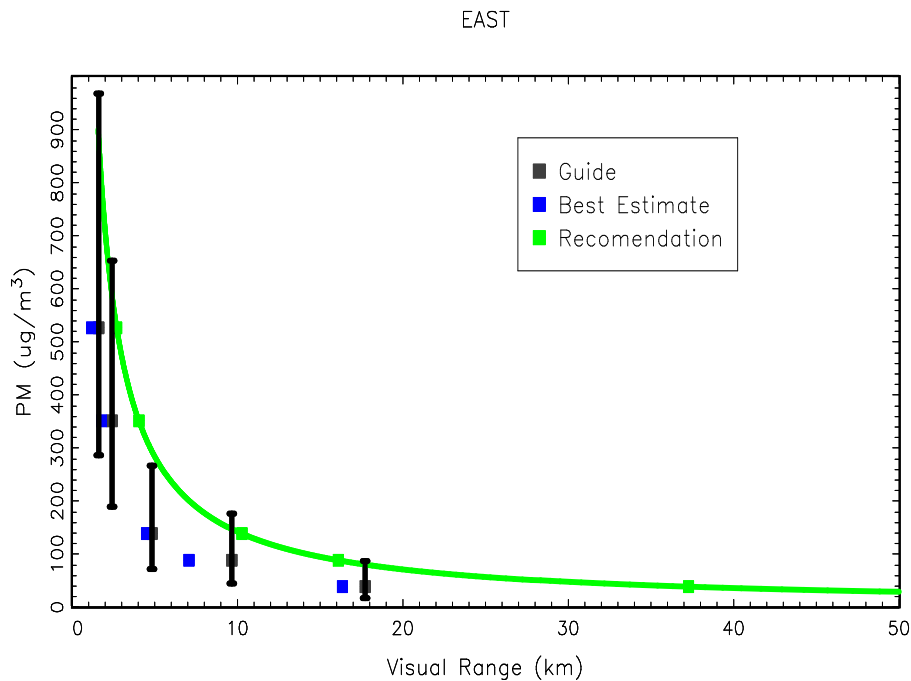


Figure 7.2: (East) Plot of the smoke guide's ("Wildfire Smoke, A Guide for Public Health Officials", 2008) PM vs. V_r relationship, as well as the uncertainty in the PM estimate derived from a visual range observation. Also plotted are the recommended visual ranges that are to be associated with the mass concentration breakpoint.

Other related recommendations:

- At a minimum, refine the estimate of CNST to reflect unique climatological regions of the United States using the full suite of IMPROVE information. The above recommendations are based on an in-depth analysis of only two IMPROVE sites, Grand Canyon and Great Smoky Mountains national parks, and these results have been generalized to the Intermountain West and eastern United States. The Northwest, Southwest, Sierra Nevada, etc., warrant specific attention.
- The particulate matter estimate could be improved by developing a simple algorithm (implemented either on a personnel PC or smart phone) to incorporate a measure of RH to adjust a mass determination to reflect the amount of water contained in ambient and smoke aerosols. That is, adjust the mass determination down to reflect the hygroscopicity of the ambient as well as smoke aerosol to arrive at a better estimate of true dry mass concentration.
- More appropriately, develop a CNST value for every part of the United States at seasonal or monthly temporal resolutions. Access this information through a smart phone or PC app that recognizes the fire's location and presents the appropriate CNST value. The CNST value would be dependent on local aerosol background conditions, RH, and fuel

types. If considering smoke impact from a specific prescribed fire, the fuel type could be used to determine an appropriate CNST value.

Recommendation #2 – Two-level air quality warning system: A 1–3 hr average, PM-concentration-based air quality warning scale based on an observed V_r should consist of no more than two levels of warning instead of the five now used (see Figure 7.1, the error bars and blue boxes). Within the uncertainty limits, the mass estimates from V_r observations associated with the first three breakpoints are essentially indistinguishable, as are the mass estimates associated with the lowest two V_r categories.

Recommendation #3 – An actual visual range determination should not be attempted: A more defensible procedure would be to identify landscape features that have not disappeared or can be seen or identified. Then it is possible to state that the mass concentration is some value (corresponding to the distance to the landscape feature) or less. The ability to determine a threshold contrast of 0.02 is very difficult and only can be done by highly trained observers. Even then, a significant fraction of observers, depending on the threshold criteria, will say they see the feature when it cannot be seen. More likely, the contrast that is interpreted as 0.02 is significantly greater, and the associated uncertainty in estimated mass is significantly greater, than assumed in the above analysis. Moreover, it is highly unlikely that a landscape feature can be found that is exactly at the V_r . More typically, the landscape feature will be at a distance that is greater or less than the V_r .

Other related recommendations:

- Develop a smart phone application to directly measure landscape feature contrast that allows V_r to be calculated and therefore allows for a more accurate assessment of mass concentration.
- Develop simple “contrast cards” that can be compared to landscape feature contrast, thus allowing for a contrast estimation of that landscape feature and, in turn, a V_r estimation.

8. REFERENCES

Abel, S. J., J. M. Haywood, E. J. Highwood, J. Li and P. R. Buseck, Evolution of biomass burning aerosol properties from an agricultural fire in southern Africa, *Geophysical Research Letters*, 30(15) 2003.

Alaska Smoke Visibility and Air Quality Index
<http://co.fairbanks.ak.us/AirQuality/Docs/ParticulateLevels.pdf>, retrieved on 4/8/2013.

Artaxo, P., F. Gerab, M. A. Yamasoe and J. V. Martins, Fine mode aerosol composition at 3 long-term atmospheric monitoring sites in the Amazon basin, *Journal of Geophysical Research-Atmospheres*, 99(D11), 22857-22868, 1994.

Artaxo, P., E. T. Fernandes, J. V. Martins, M. A. Yamasoe, P. V. Hobbs, W. Maenhaut, K. M. Longo and A. Castanho, Large-scale aerosol source apportionment in Amazonia, *Journal of Geophysical Research*, 103(D24), 31,837-31,847, 1998.

Bond, T. C., T. L. Anderson and D. Campbell, Calibration & Intercomparison of Filter-Based Measurements Of Visible Light Absorption by Aerosols, *Aerosol Science & Tech*, 30, 582-600, 1999.

Campbell, D., S. Copeland, and T.A. Cahill, Response to “Comment on Measurement of aerosol absorption coefficient from Teflon filters using the integrating plate and integrating sphere techniques”, *Aerosol Science & Tech*, 24, 225-229, 1996.

Chand, D., O. Schmid, P. Gwaze, R. S. Parmar, G. Helas, K. Zeromskiene, A. Wiedensohler, A. Massling and M. O. Andreae, Laboratory measurements of smoke optical properties from the burning of Indonesian peat and other types of biomass, *Geophysical Research Letters*, 32(12) 2005.

Chen, L. W. A., H. Moosmuller, W. P. Arnott, J. C. Chow and J. G. Watson, Particle emissions from laboratory combustion of wildland fuels: In situ optical and mass measurements, *Geophysical Research Letters*, 33(4) 2006.

Chen, L. W. A., H. Moosmuller, W. P. Arnott, J. C. Chow, J. G. Watson, R. A. Susott, R. E. Babbitt, C. E. Wold, E. N. Lincoln and W. M. Hao, Emissions from laboratory combustion of wildland fuels: Emission factors and source profiles, *Environmental Science & Technology*, 41(12), 4317-4325, 2007.

Claeys, M., R. Vermeylen, F. Yasmeen, Y. G´omez-Gonz´alez, Y., X. Chi, W. Maenhaut, T. M´esz´aros, T., and I. Salma, Chemical characterization of humic-like substances from urban, rural and tropical biomass burning environments using liquid chromatography with UV/vis photodiode array detection and electrospray ionisation mass spectrometry, *Environmental Chemistry*, 9, 273–284, doi:10.1071/EN11163, 2012.

Colorado Wildfire Information <http://www.colorado.gov/airquality/wildfire.aspx>, retrieved on 4/8/2013.

Day, D. E., J. L. Hand, C. M. Carrico, G. Engling and W. C. Malm, Humidification factors from laboratory studies of fresh smoke from biomass fuels, *Journal of Geophysical Research-Atmospheres*, 111(D22), Art. No. D22202, 2006.

Duntley, S. Q. Reduction of apparent contrast by the atmosphere, *Journal of the Optical Society of America*, 38, 179, 1948.

Echalar, F., P. Artaxo, J. V. Martins, M. Yamasoe and F. Gerab, Long-term monitoring of atmospheric aerosols in the Amazon Basin: Source identification and apportionment, *Journal of Geophysical Research*, 103(D24), 31,849-31,864, 1998.

Formenti, P., O. Boucher, T. Reiner, D. Sprung, M. O. Andreae, M. Wendisch, H. Wex, D. Kindred, M. Tzortziou, A. Vasaras and C. Zerefos, STAAARTE-MED 1998 summer airborne measurements over the Aegean Sea - 2. Aerosol scattering and absorption, and radiative calculations, *Journal of Geophysical Research-Atmospheres*, 107(D21), 2002.

Formenti, P., W. Elbert, W. Maenhaut, J. Haywood, S. Osborne and M. O. Andreae, Inorganic and carbonaceous aerosols during the Southern African Regional Science Initiative (SAFARI 2000) experiment: Chemical characteristics, physical properties, and emission data for smoke from African biomass burning, *Journal of Geophysical Research-Atmospheres*, 108(D13), 2003.

Gras, J. L., J. B. Jensen, K. Okada, M. Ikegami, Y. Zaizen, and Y. Makino, Some optical properties of smoke aerosol in Indonesia and tropical Australia, *Geophys. Res. Lett.*, 26, 1393-1396, 1999.

Guyon, P., B. Graham, J. Beck, O. Boucher, E. Gerasopoulos, O. L. Mayol-Bracero, G. C. Roberts, P. Artaxo, and M. O. Andreae, Physical properties and concentrations of aerosol particles over the Amazon tropic forest during background and biomass burning conditions, *Atmos. Chem. Phys.*, 3, 951-967, 2003.

Hand, J. L. and W. C. Malm, Review of aerosol mass scattering efficiencies from ground-based measurements since 1990, *Journal of Geophysical Research*, 112(D16203), doi:10.1029/2007JD008484, 2007.

Hand, J. L., D. E. Day, G. R. McMeeking, E. J. T. Levin, C. M. Carrico, S. M. Kreidenweis, W. C. Malm, A. Laskin and Y. Desyaterik, Measured and modeled humidification factors of fresh smoke particles from biomass burning: Role of inorganic constituents, *Atmospheric Chemistry and Physics*, 10, 6179-6194, 2010.

Haywood, J. M., S. R. Osborne, P. N. Francis, A. Keil, P. Formenti, M. O. Andreae and P. H. Kaye, The mean physical and optical properties of regional haze dominated by biomass burning aerosol measured from the C-130 aircraft during SAFARI 2000, *Journal of Geophysical Research-Atmospheres*, 108(D13), 2003.

Heintzenberg, J., R. J. Charlson, A. D. Clarke, C. Liousse, V. Ramaswamy, K. P. Shine, and M. Wendisch, Measurements and modeling of aerosol single-scattering albedo: Progress, problems, and prospects, *Beitr. Phys. Atmos.*, 70, 249-263, 1997.

Hobbs, P. V., J.S. Reid, J.A. Herring, J. D. Nance, R. E. Weiss, J. L. Ross, D. A. Hegg, R. D. Ottmar, and C. Liou, Particle and trace-gas measurements in smoke from prescribed burns of forest products in the Pacific Northwest, in: *Biomass Burning and Global Change*, Vol. 1, edited by: Levine, J. S., MIT Press, New York 697-715, 1996.

Hobbs, P.V., J. S. Reid, R. A. Kotchenruther, R. J. Ferek, and R. Weiss, Direct radiative forcing by smoke from biomass burning, *Science*, 275, 1776-1778, 1997.

Hoffer, A., A. Gelencser, P. Guyon, G. Kiss, O. Schmid, G. P. Frank, P. Artaxo, and M. O. Andreae, Optical properties of humic-like substances (HULIS) in biomass-burning aerosols, *Atmos. Chem. Phys.*, 6, 3563-3570, 2006.

Intergovernmental Panel on Climate Change (IPCC): *Climate Change 2001: Radiative Forcing of Climate change*, edited by: Houghton, J. T., Ding, Y., Griggs, D. J., Noguer, M., van der Linden P. J. and Xiaosu, D., Cambridge Univ. Press, Cambridge, 2001.

Iziomon, M. G. and U. Lohman, Optical and meteorological properties of smoke-dominated haze at the ARM Southern Great Plains Central Facility, *Geophys. Res. Lett.*, 30(3), 1123, 2003.

Kim, J., S. C. Yoon, A. Jefferson and S. W. Kim, Aerosol hygroscopic properties during Asian dust, pollution, and biomass burning episodes at Gosan, Korea in April 2001, *Atmospheric Environment*, 40(8), 1550-1560, 2006.

Kirchstetter, T. W., T. Novakov and P. V. Hobbs, Evidence that the spectral dependence of light absorption by aerosols is affected by organic carbon, *Journal of Geophysical Research-Atmospheres*, 109(D21) 2004.

Kitanovski, Z., I. Grgif'a, R. Vermeylen, M. Claeys, and W. Maenhaut, Liquid chromatography tandem mass spectrometry method for characterization of monoaromatic nitro-compounds in atmospheric particulate matter, *J. Chromatography A*, 1268, 35-43, doi:10.1016/j.chroma.2012.10.021, 2012.

Kotchenruther, R. A. and P. V. Hobbs, Humidification factors of aerosols from biomass burning in Brazil, *Journal of Geophysical Research*, 103(D24), 32,081-32,089, 1998.

Lack, D. A., R. Bahreni, J. M. Langridge, J. B. Gilman, and A. M. Middlebrook, Brown carbon absorption linked to organic mass tracers in biomass burning particles, *Atmos. Chem. Phys.*, 13, 2415-2422, 2013

Levin, E. J. T., G. R. McMeeking, C. M. Carrico, L. E. Mack, S. M. Kreidenweis, C. E. Wold, H. Moosmüller, W. P. Arnott, W. M. Hao, J. L. Collett, Jr. and W. C. Malm, Biomass burning smoke aerosol properties measured during Fire Laboratory at Missoula Experiments (FLAME), *Journal of Geophysical Research*, 115(D18210)doi:10.1029/2009JD013601, 2010.

Mack, L. A., E. J. T. Levin, S. M. Kreidenweis, D. Obrist, H. Moosmuller, K.A. Lewis, W. P. Arnott, G. R. Mc Meeking, A. P. Sullivan, C. E. Wold, W. M. Hao, J. L. Collett Jr. W.C. Malm,

Optical closure experiments for biomass smoke aerosols, *Atmos. Chem. Phys.*, 10, 9017-9026, 2010.

Magi, B.I. and Hobbs, P.V., Effects of humidity on aerosols in southern Africa during the biomass burning season. *J. Geophys. Res.*, 108(D13), 8495 doi: 10.1029/2002JD002144, 2003.

Magi, B. I., P. V. Hobbs, B. Schmind, and J. Redmann, Vertical profile of light scattering, 46 light absorption, and single- scattering albedo during the dry, biomass burning season in southern Africa and comparisons of in situ and remote sensing measurements of aerosol optical depth, *J. Geophys. Res.*, 108(D18), 8504, 2003.

Malm, W., Considerations in the measurement of visibility, *Journal of the Air Pollution Control Association*, 29(10), 1042-1052, 1979.

Malm, W. C. and J. L. Hand, An examination of the physical and optical properties of aerosols collected in the IMPROVE program, *Atmos. Environ.*, doi:10.1016/j.atmosenv.2006.12.012, 2007.

Malm W. C., J. F. Sisler, D. Huffman, R. A. Eldred, and T. A. Cahill, Spatial and seasonal trends in particle concentration and optical extinction in the United States. *Journal of Geophysical Research* 99(D1), 1347-1370, 1994.

Malm, W. C. and S. M. Kreidenweis, The effects of models of aerosol hygroscopicity on estimated scattering efficiencies, Pres at the 89th Annual Mtg & Exhibition of the AWMA, paper #96-MP1A.01, Nashville, TN, 1996.

Malm, W. C., Introduction to Visibility, CIRA, NPS Visibility Program, Colorado State University, Fort Collins, CO, 2000.

Malm, W. C., D. E. Day, S. Kreidenweis, J. L. Collett Jr., C. M. Carrico, G. R. McMeeking, T. Lee, J. Carrillo and B. A. Schichtel, Hygroscopic properties of an organic-laden aerosol, *Atmospheric Environment*, 39, 4969-4982, 2005a.

Malm, W. C., D. Day, C. M. Carrico, S. M. Kreidenweis, J. Collett, G. McMeeking, T. Lee and J. Carrillo, Intercomparison and closure calculations using measurements of aerosol species and optical properties during the Yosemite Aerosol Characterization Study., *Journal of Geophysical Research*, 110(D14302), doi:10.1029/2004JD005494- 2005b.

Martins, J. V., P. Artaxo, P. V. Hobbs, C. Liousse, H. Cachier, Y. Kaufman and A. Plana-Fattori, Particle Size Distributions, Elemental Compositions, Carbon Measurements, and Optical Properties of Smoke from Biomass Burning in the Pacific Northwest of the United States, In *Biomass Burning and Global Change*, edited by J. S. Levine, 2(67), 716-732, 1996.

Martins, J. V., P. Artaxo, C. Liousse, J. S. Reid, P. V. Hobbs, and Y.J. Kaufman, Effects of black carbon content, particle size, and mixing on light absorption by aerosols from biomass burning in Brazil, *J. Geophys. Res.*, 103, 32 041-32 050, 1998a.

- Martins, J. V., P. V. Hobbs, R. E. Weiss, and P. Artaxo, Sphericity and morphology of smoke particles from biomass burning in Brazil, *J. Geophys. Res.*, 103, 32 051-32 058, 1998b.
- McMeeking, G. R., S. M. Kreidenweis, S. Baker, C. M. Carrico, J. C. Chow, J. L. Collett, W. M. Hao, A. S. Holden, T. W. Kirchstetter, W. C. Malm, H. Moosmuller, A. P. Sullivan and C. E. Wold, Emissions of trace gases and aerosols during the open combustion of biomass in the laboratory, *Journal of Geophysical Research-Atmospheres*, 114(D19210)doi:10.1029/2009JD0011836, 2009.
- Middleton, W.E.K., *Vision through the atmosphere*, Univ. Toronto Press, Toronto, Ontario, Canada, 1952.
- Miller, J. R. and N. T. O'Neill, Multi-altitude airborne observations of isolation effects of forest fire smoke aerosols at BOREAS: Estimates of aerosol optical parameters, *J. Geophys. Res.*, 102, 29 729-29 736, 1997.
- Montana Wildfire Smoke Updates <http://www.deq.mt.gov/FireUpdates/cutpointsRevised.mcp>, retrieved on 4/8/2013.
- Nance, J. D., P. V. Hobbs and L. F. Radke, Airborne Measurements of Gases and Particles from An Alaskan Wildfire, *Journal of Geophysical Research-Atmospheres*, 98(D8), 14873-14882, 1993.
- O'Neill, S. M., P.W. Lahm, M.J. Fitch, Summary and analysis of approaches linking visual range PM2.5 concentrations and air quality health impact indices for wildfires, 2013.
- Pitchford, M. L., W. C. Malm, B. A. Schichtel, N. Kumar, D. Lowenthal and J. L. Hand, Revised algorithm for estimating light extinction from IMPROVE particle speciation data, *Journal of the Air & Waste Management Association*, 57, 1326-1336, 2007.
- Pilewskie, P., J. Pommier, R. Bergstrom, W. Gore, S. Howard, M. Rabbette, B. Schmid, P. V. Hobbs and S. C. Tsay, Solar spectral radiative forcing during the Southern African Regional Science Initiative, *Journal of Geophysical Research-Atmospheres*, 108(D13) 2003.
- Radke, L. F., D. A. Hegg, J. H. Lyons, C. A. Brock, P. V. Hobbs, R. Weiss, and R. Rasmussen, Airborne measurements on smokes from biomass burning, *Aerosols and Climate*, edited by Hobbs, P. V. and McCormick, M/ P., Deepak Publishing, Hampton, VA, 411-422, 1988.
- Radke, L. F., D. A. Hegg, P. V. Hobbs, J. D. Nance, J. H. Lyons, K. K. Larsen, R. E. Weiss, P. J. Regan, and D. E. Ward, Particulate and trace emissions from larger biomass fires in North American, *Global Biomass Burning: Atmospheric, Climatic, and Biospheric Implications*, edited by Levine, J.S., MIT Press Cambridge, MA, 209-224, 1991.
- Reid, J. S. and P. V. Hobbs, Physical and optical properties of smoke from individual biomass fires in Brazil, *J. Geophys. Res.*, 103, 32 013–32 031, 1998.

- Reid, J. S., P. V. Hobbs, C. Liou, J. V. Martins, R. E. Weiss, and T. F. Eck, Comparisons of techniques for measuring shortwave absorption and black carbon content of aerosols from biomass burning in Brazil, *J. Geophys. Res.*, 103, 32 031–32 040, 1998a.
- Reid, J. S., P. V. Hobbs, R. J. Ferek, D. R. Blake, J. V. Martins, M. R. Dunlap, and C. Liou, Physical, chemical and optical properties of regional hazes dominated by smoke in Brazil, *J. Geophys. Res.*, 103, 32 059–32 080, 1998b.
- Reid, J. S., R. Koppmann, T. F. Eck and D. P. Eleuterio, A review of biomass burning emissions part II: intensive physical properties of biomass burning particles, *Atmospheric Chemistry and Physics*, 5, 799-825, 2005a.
- Reid, J. S., T. F. Eck, S. A. Christopher, R. Koppmann, O. Dubovik, D. P. Eleuterio, B. N. Holben, E. A. Reid and J. Zhang, A review of biomass burning emissions part III: intensive optical properties of biomass burning particles, *Atmospheric Chemistry and Physics*, 5, 827-849, 2005b.
- Ross, H.E. and Murray, D. J.(Ed. and Transl.), E.H.Weber on the Tactile Senses, 2nd ed., Hove: Erlbaum (UK) Taylor & Francis, 1996.
- Russell, P. B., J. Redemann, B. Schmid, R. W. Bergstrom, J. M. Livingston, D. M. McIntosh, S. Hartley, P. V. Hobbs, P. K. Quinn, C. M. Carrico, M. J. Rood, E. Öström, K. J. Noone, W. von Hoyningen-Huene and L. Remer, Comparison of aerosol single scattering albedos derived by diverse techniques in two North Atlantic experiments, *J.Atmos.Sci.Global Aerosol Climatology Special Issue*, 59(3), 609-619, 2002.
- Schwarz J.P., R. S. Gao, J. R. Spackman, L. A. Watts, D. S. Thomson, D. W. Fahey, T. B. Ryerson, J. Peischl, J. S. Holloway, M. Trainer, G. J. Frost, T. Baynard, D. A. Lack, J. A. de Gouw, C. Warneke, and L. A. Del Negro, Measurement of the mixing state, mass, and optical size of individual black carbon particles in urban and biomass burning emissions, *Geophysical Research Letters*, 35, L13810, doi:10.1029/2008GL033968, 2008.
- Sloane, C. S., Optical properties of aerosols-comparison of measurements, *Atmos.Environ.*, 17, 409-416, 1983.
- Sloane, C. S., Optical properties of aerosols of mixed composition, *Atmos.Environ.*, 18(4), 871-878, 1984.
- Sloane, C. S. and G. T. Wolff, Prediction of ambient light scattering using a physical model responsive to relative humidity: valid, *Atmos.Environ.*, 19(4), 669-680, 1985.
- Sloane, C. S., Effect of composition on aerosol light scattering efficiencies, *Atmos.Environ.*, 20(5), 1025-1037, 1986.
- Tangren, C. D., Scattering Coefficient and Particulate Matter Concentration in Forest Fire Smoke, *Journal of the Air Pollution Control Association*, 32(7), 729-732, 1982.

Tang, I. N., W. T. Wong and H. R. Munkelwitz, The relative importance of atmospheric sulfates and nitrates in visibility reduction, *Atmos. Environ.*, 15(12), 2463-2471, 1981.

Van de Hulst, H.C., *Light Scattering by Small Particles*. Dover Publications, New York, New York, 1981.

White, W. H., On the theoretical and empirical basis for apportioning extinction by aerosols: a critical review, *Atmos. Environ.*, 20(9), 1659-1672, 1986.

Wildfire Smoke, A Guide for Public Health Officials
http://www.ehib.org/papers/wildfire_smoke_july_2008.pdf, 2008.

Yamasoe, M. A., P. Artaxo, A. H. Miguel and A. G. Allen, Chemical composition of aerosol particles from direct emissions of vegetation fires in the Amazon Basin: water-soluble species and trace elements, *Atmospheric Environment*, 34(10), 1641-1653, 2000.

Yang, M., S. G. Howell, J. Zhuang, and B. J. Huebert, Attribution of aerosol light absorption to black carbon, brown carbon, and dust in China – interpretations of atmospheric measurements during EAST-AIRE, *Atmos. Chem. Phys.*, 9, 2035–2050, doi:10.5194/acp-9-2035-2009, 2009.